Chapter 14

Noise, Vibration, and Health and Usage Monitoring Systems (HUMS) of Aircraft Dynamic Components

Chapter details

Chapter DOI:

https://doi.org/10.4322/978-65-86503-83-8.c14

Chapter suggested citation / reference style:

Cruz, Alejandro R., et al. (2022). "Noise, Vibration, and Health and Usage Monitoring Systems (HUMS) of Aircraft Dynamic Components". *In* Jorge, Ariosto B., et al. (Eds.) *Fundamental Concepts and Models for the Direct Problem*, Vol. II, UnB, Brasilia, DF, Brazil, pp. 386–450. Book series in Discrete Models, Inverse Methods, & Uncertainty Modeling in Structural Integrity.

P.S.: DOI may be included at the end of citation, for completeness.

Book details

Book: Fundamental Concepts and Models for the Direct Problem

Edited by: Jorge, Ariosto B., Anflor, Carla T. M., Gomes, Guilherme F., & Carneiro, Sergio H. S.

Volume II of Book Series in:

Discrete Models, Inverse Methods, & Uncertainty Modeling in Structural Integrity

Published by: UnB City: Brasilia, DF, Brazil Year: 2022

DOI: https://doi.org/10.4322/978-65-86503-83-8

Noise, Vibration, and Health and Usage Monitoring Systems (HUMS) of Aircraft Dynamic Components

Alejandro Rios Cruz[1] Ariosto B. Jorge[2] Bento S. de Mattos[1*]
Ronaldo V. Cruz[1]

[1]Instituto Tecnológico de Aeronáutica. E-mail: alejandro.cruz@ga.ita.br, bmattos@ita.br; ronaldoc@ita.br
[2]Post-Graduate Program - Integrity of Engineering Materials, University of Brasilia, Brazil. E-mail: ariosto.b.jorge@gmail.com

*Corresponding author

Abstract

This work is concerned with vibrations and noise in helicopters and turbofan engines. An overview of current and under research techniques to improve the detection of faulty components and Health and Usage Monitoring Systems (HUMS) tools are addressed in this book chapter. An overview of noise theory and existing sources in aircraft is carried out. Some applications with hybrid methods to measure the impact and extension of noise generated, by the landing gear, ice probes, and slatted-airfoil configurations are shown and discussed. Traditionally, system prognostics and health management (PHM) depend on sufficient previous knowledge of critical components degradation process to predict the remaining useful life (RUL). However, accurate physical or expert models are not applicable in most cases. The present work shows an example of how to predict engines' remaining useful life (RUL) by utilizing deep convolutional neural networks (CNNs). CNN is more often utilized for classification and computer vision tasks. The advantage of a deep learning approach is that the user does not need manual extraction or selection of features for models to predict RUL. Moreover, there is a need for pre-existing knowledge of machine health prognostics or signal processing to develop a deep learning-based RUL prediction model. The example uses NASA's Turbofan Engine Degradation Simulation Data Set (C-MAPSS). The data set contains run-to-failure time series for four diverse sets, which were simulated with combinations of operational conditions and fault modes. This example uses only one data set, which is further divided into training and test subsets. In addition, relevant noise sources in transport aircraft and rotorcraft are discussed. A turbofan engine code and another to predict the airframe noise of transport airplanes are employed in a multi-disciplinary design and optimization framework (MDO) to design a 78-seat airliner.

Keywords: noise, vibration in aircraft, health, and usage monitoring system, turbofan engine, convolutional neural network

1. Causes and effects of vibration in dynamic components

1.1 Rotorcraft

The study of the causes and effects of vibrations in dynamic components has become a continuous task for manufacturers of helicopters, engines, and transmission gears. Excitations come from all the possible sources of tan helicopters like main/tail rotors, engines, and transmissions. Vibrations may affect equipment performances and even cause some failures in the short term.

The FAR regulations concerning vibration safety on the helicopter can be summarized in the following way (1):

- §29.251 Vibrations:

  "Each part of the rotorcraft must be free from excessive vibration under each appropriate speed and power conditions"
- §29.1301d Function and installation:

  "Each item of installed equipment must function properly when installed"
- §29.1309a Equipment, systems, and installations:

  "The equipment, systems, and installations whose functioning is required by this subchapter must be designed and installed to ensure that they perform their intended functions under any foreseeable operating condition"
- §29.571 Structural fatigue: this paragraph is not under Dynamics and Vibration responsibility but Structure. Some objectives of equipment assessment:
  - Ensure that vibration does not affect the equipment's performance
  - Prevent vibration-related failures (dynamic fatigue phenomena)
  - Show compliance with FAR 29.251

There is a quest to implement techniques for minimizing the effects of these vibrations and early detection of their impact on the useful life of aircraft components. The usual measures to mitigate or reduction of vibration causes are suppression, absorption, reduction, isolation, or active/passive control of vibrations, or a combination of these techniques. As a result of all these efforts, several maintenance techniques have been developed, to be employed by the aircraft operator, which can be divided into two groups: reduction of the vibration levels and analysis of vibrations.

Vibration reduction techniques available for the helicopter operators focus on the adjustment of the blade track of the main and tail rotors, and/or in the correction of any imbalance present in these rotors, as well as any imbalance present in some specific dynamic components of the aircraft, such as gearboxes, main and tail rotor drive shafts, oil cooler fans, etc.

In a subsequent step, the user should concentrate his efforts on the vibration analysis, which consists in obtaining the aircraft vibration signature, i.e., the survey of the values of vibration amplitude versus frequency, carried out in pre-established locations and flight conditions, utilizing accelerometers and analyzers that directly provide a fault spectrum in the frequency domain.

The records of vibration signatures, duly filed, will form a vibration database of each aircraft type, which will be used as a starting point for the assessment of the vibration levels of a particular aircraft at a certain time of its useful life, allowing the detection, location, and identification of problems or defects, even when they are still incipient. Thus, vibration analysis would become an important predictive maintenance tool to monitor the wear and fatigue of components and reduce maintenance costs.

The reduction of vibrations found in helicopters has, among others, the objectives of (2):

a) Reduce the probability of failures in structural components before they reach their life limit. Such components have an estimated life, considering a certain magnitude of cyclic loads, acting on them. In this way, considering that there is a direct relationship between the vibration level of the structure and the cyclic loads acting, a high level of vibration shows that the structural components of the helicopter are being subjected to efforts beyond those estimated in its design and, consequently, present a high probability of in-service fatigue failures.

b) Minimize the effects of tiredness and fatigue on the crew. Prolonged and repeated exposure to vibrations of different frequencies, amplitudes, and directions can cause various types of aggressions that essentially consist of headaches, tinnitus, general malaise, feeling of drowsiness, general weakness, irritability, a reduction in the will and the ability to concentrate, a reduction in reflexes, a psychic depression as well as fatigue of the eyes and ears. Depending on their intensity and persistence, these disturbances can decisively contribute to pilot fatigue and helicopter accidents.

Each system of a helicopter generates vibration at a specific frequency and amplitude. Despite the main rotor rotating at a constant angular speed, it induces vibrations in many helicopter systems and subsystems. The analysis of vibrations parameters enables the mapping of the nodes and anti-node locations (Figure 2). At each rotor cycle about its axis, the loads caused by the rotor provoke cycled stresses on other systems. If a weight m is added to a determined system, it radically alters the vibration characteristics of that system. Put differently, the balanced mass shall alter the system's natural frequency to the same frequency of excitement. This way, the resonator cancels out the system's vibration.

To better explain the characteristics of the combination of masses and springs a system of two degrees of freedom is taken as an example. A system is defined as having two degrees of freedom when two coordinates are required to describe the motion. This type of system will also have two eigenfrequencies and two normal modes of vibration which, in turn, refer to the relationship between the amplitudes of the two coordinates for each corresponding eigenfrequency.

Free vibration, when subjected to an initial condition, will generally be the superposition of the two normal modes of vibration. However, if a forced harmonic vibration occurs with a given excitation frequency, the amplitude of each of the two coordinates will tend to a maximum at the two proper frequencies.

These characteristics are understood through the example presented in Figure 1. In this spring-mass system, which is used as a vibration absorber in helicopters, k_2 and m_2 are adjusted about the frequency of the exciting force, in such a way that the movement of the main mass m_1 (point B) is reduced to zero (3).

In fact, in Figure 1(b), it can be seen that:

1. for the interval $0 < \Omega < \Omega_A$, the two bodies are moving in phase with the excitation, as the two maximum amplitudes are positive. For frequencies close to 0, the displacements of the two masses are slightly different, depending on the stiffness and mass parameters. However, for $\Omega \cong \Omega_A$, the maximum amplitudes of the two masses tend to infinity. Therefore, Ω_A corresponds to the natural frequency of the 1st normal mode of vibration, which is related to the in-phase motion of the masses;
2. for the interval $\Omega_A < \Omega < \Omega_C$, the two bodies initially move in phase (but in opposition to phase with the excitation), since the two maximum amplitudes are negative, inverting the phase (a maximum amplitude positive and one negative) from $\Omega \cong \Omega_B$;
3. for the interval $\Omega_C < \Omega < \infty$, the two bodies move out of phase symmetrically, so that m_2 and m_1 are, respectively, in-phase and in phase opposition with the excitation. For $\Omega \cong \Omega_C$, the maximum amplitudes of the two masses tend to infinity, and then Ω_C corresponds to the natural frequency of the 2nd normal mode of vibration (masses in phase opposition).

It can also be verified that the amplitude X_1 will be null, when $\Omega = \Omega_B$, but, under these conditions, the absorber mass will be submitted to an amplitude $X_2 = -{}^{F_0}/_{k_2}$, since the mass-spring system k_2 and m_2 oppose each other to the disturbing force.

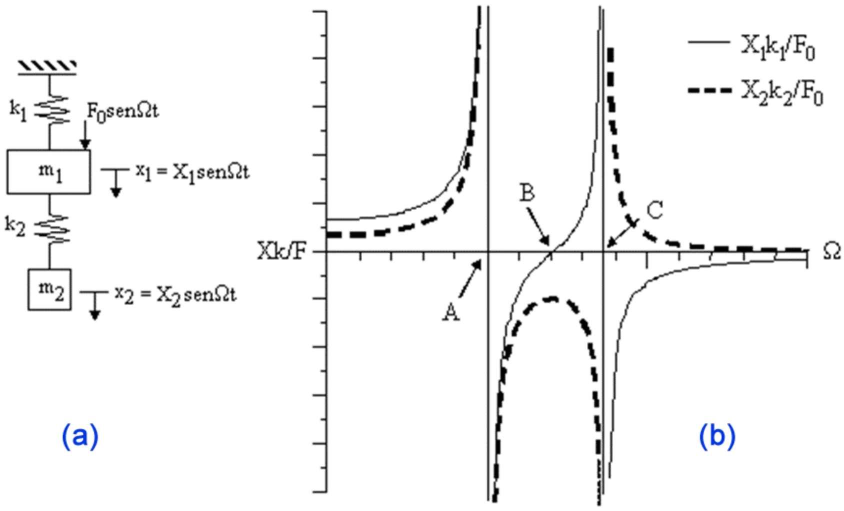

Figure 1: System with two degrees of freedom (3)

The spring-mass combination enables the development of resonators to mitigate vibration. The number of resonators and their location shall be determined to reduce the vibration amplitude to an acceptable minimum. Regarding the reduction of vibration levels suffered by the helicopter crew, some resonators are placed under the pilot and co-pilot seats (Figure 3) to mitigate vertical vibrations from the main rotor. In this case, the resonators are adjusted to mitigate the $nb\Omega$, where n is an integer number representing a multiple of the fundamental frequency of the rotor assembly, b is the number of the blades, and Ω is the rotation frequency of the main rotor. All harmonics will be transmitted to the fuselage but the first one will cause vibration with higher amplitudes.

The multiples of the fundamental frequency (2*Ω, 3Ω, 4Ω,* etc.) will cause noise and the amplitudes of their vibrations will be considerably lower (3).

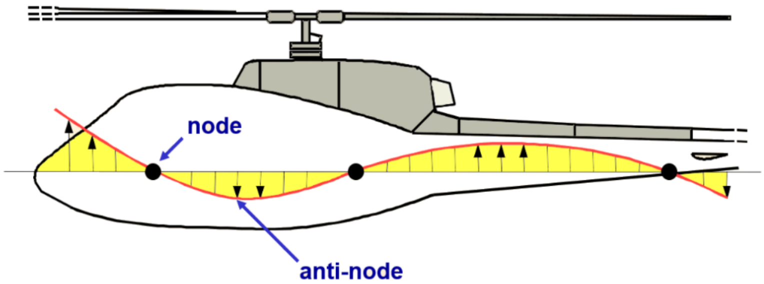

Figure 2: Vertical vibration amplitudes with no cabin resonators (adapted from (4))

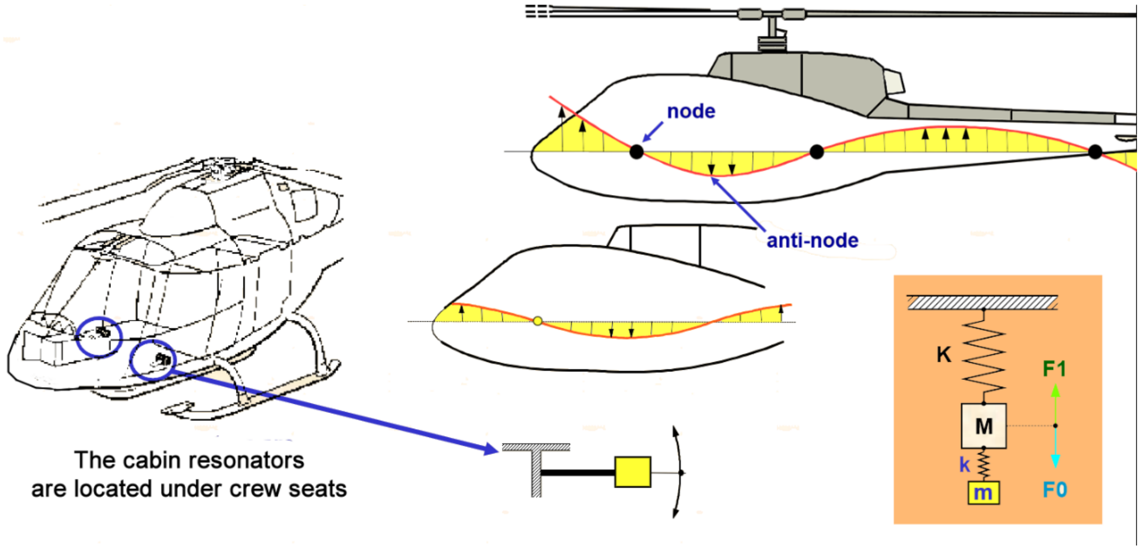

Figure 3: The addition of resonators reduces the vibration amplitude [Adapted from (4)]

The rule of thumb for blade weight and aerodynamic adjustment is that all the blades must be strictly identical in the spanwise sense (same weight and same weight distribution) and aerodynamically (same airfoil geometry). If so, there would be no problems and the rotor would then find flawless functioning. On the contrary, the rotor is unbalanced when the loads are not equal on all the blades. The rotation then induces periodical load variations generating vibrations, whose amplitude depends on the blade load differences.

Rotor blades must be statically and dynamically balanced. Regarding static balance, the blades should have the same static moment, defined as the product of the blade weight (W) and the lever arm, the distance of CG from the rotor axis. Balance weights are properly installed at the blade tips to obtain equal static moments. The weights modify both the blade weight and the blade CG location, i.e. its static moment.

The distance (d) between the CG. and the center of the lift induces a twisting moment, which deforms the blade and therefore the lift that is generated. As consequence, stresses are generated. One requirement for dynamic balance is that the distance (d) be the same for all blades to produce the same twisting moment. This condition is satisfied by adding blade tip balance weights at the front and rear of the airfoil (Figure 4). These weights move the chordwise CG. to adjust the distance (d).

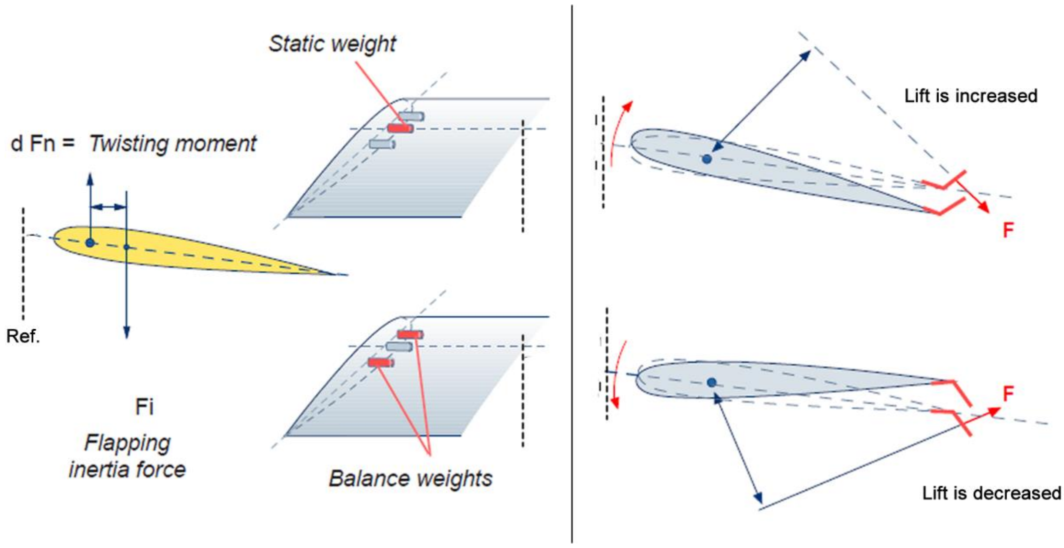

Figure 4: Dynamic balancing (5)

1.2 Turbofan and turboshaft engines

Turbofan engines find widespread use in commercial transport due to their advantage of higher performance and lower noise. The noise reduction for this kind of engine comes from combinations of changes to the engine cycle parameters and low noise design features.

During normal operation, airliners are steadily sending small packages known as ACARS (Aircraft Communication Addressing and Reporting System) to ground stations. Information is transmitted to orbiting satellites that relay the data to ground stations. Each package of messages is limited in size, but it is possible to send considerable measurements taken from the aircraft data computer and engine controllers.

The full authority digital engine (or electronics) control (FADEC) is a system consisting of a digital computer, called an electronic engine controller (EEC) or engine control unit (ECU), and its related accessories that control all aspects of aircraft engine operation. However, FADEC's main objective is to guarantee that the engine works within a prescribed operation envelope, lengthening this way its useful life. The fan speed is the parameter used to define the engine thrust. The FADEC controls the fan speed for the required thrust based on pressure altitude, temperature, and Mach number.

During take-off and cruise phases, information packages are always transmitted. Health Monitoring embedded systems acquire a lot of data (Big data), among them, meaningful indicators, and context information. Typically, information such as N2 (High-Pressure engine speed), EGT (Exhaust Gas Temperature), and FF (Fuel Flow) but also PS3 (static pressure after compressor) and T3 (temperature after compressor) and all associated context data are transmitted (6). Those last measurements give information about the compressor's behavior and help to differentiate compressor degradation from that of the turbine (6).

Helicopter jet engines consist of two stages. The first stage includes a compressor, combustion chamber, and turbine, and resembles the design of a traditional fixed-wing engine. This assembly is followed by the second stage, which is a free turbine, which must rotate at a constant angular speed. The second stage is coupled to the transmission system.

Engine turbines and compressors rotate at very high speeds and must be perfectly balanced for a flawless operation. Problems like disk cracks, blade cracks, and broken blades typically produce unbalanced rotation and are uncovered by monitoring vibration energy at the frequencies corresponding to the compressor and turbine rotating speeds.

Engine performance is gradually degraded throughout its lifetime. Performance must not be allowed to drop below a safe threshold. The engine condition is determined by measuring which engine temperature is required to deliver a given torque or thrust.

2. Health Usage Monitoring System for helicopters (HUMS)

HUMS stands for Health and Usage Monitoring System. Such a system is a common component on board modern helicopters. A helicopter counting with a HUMS experiences improvement in safety, comfort, and easier maintenance. Safety is improved due to the detection of abnormal and dangerous vibration levels. This allows the anticipate detection of cracks, misalignment, unbalance, and corrosion of shaft, bearings, and gears before they fail. Another HUMS benefit is the decrease of maintenance workload because a faulty component can be easily pinpointed. Maintenance becomes less expensive because on-condition maintenance can be then established for many components. From collected HUMS data it is possible to proceed with rotor balance, avoiding a specific technical flight to perform that task. More comfort is possible thanks to better tuning of the aircraft thanks to HUMS data.

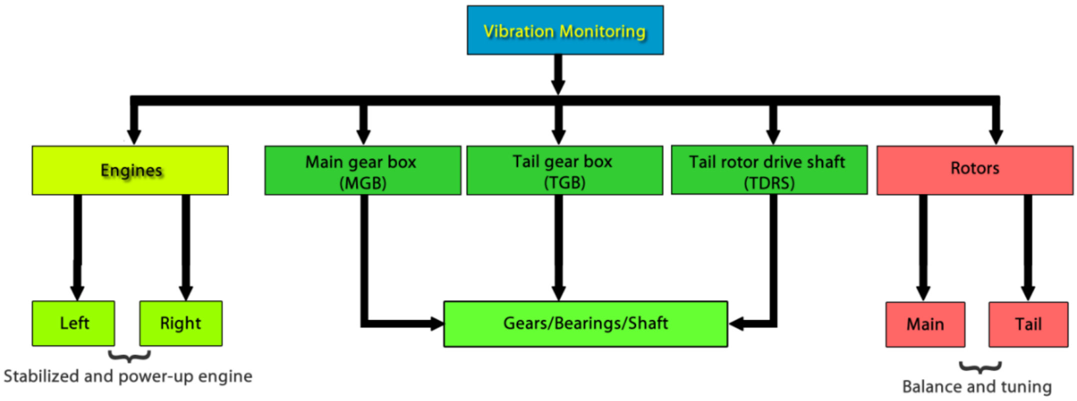

Figure 5: Typical helicopter components being monitored by health and usage monitoring systems (7)

The physical parameters that are measured by accelerometers are

- Displacement: x(t)
- Speed: $v(t) = \frac{dx}{dt}$
- Acceleration: $\gamma(t) = \frac{d^2x}{dt^2}$

Accelerometers utilize the piezoelectric properties to generate a time-domain signal. The health of mechanical components is estimated by the computation of trends and trend analysis by statistical analysis and deep learning tools. To detect anomalies in the functioning of components some analysis requires the Fast Fourier Transform (FFT) to be applied to time-domain a signal. FFT is the graph representation of harmonics in the frequency domain. Figure 6 shows a sound record in a helicopter cabin in its transformation in the frequency domain.

Accelerometers have not changed very much over time. The velometer is an accelerometer with an amplification & integration circuit built into each sensor's base (8). These additional parts ensure the signal is amplified and integrates the basic electrical output from the accelerometer (8). It then converts the direct measurement into a corresponding velocity signal or displacement reading, usually inches per second. In general terms, a velometer produces a more linear response over a far vaster frequency window than that of a basic accelerometer. It tends to be notably efficient at the medium frequency band.

The parameters which may be monitored by health and usage monitoring systems are extensive and may depend to some degree upon the precise engine/gearbox/rotor configuration. Table 1 contains a summary of some helicopter mechanical systems defects and their related indicators in the frequency domain.

Listed below some acquisition parameters together with the rationale for their use.

- Speed probes and tachometer generators: the measurement of speed is of great importance to ensure that a rotating component does not exceed limits with the risk of being overstressed.
- Temperature measurement**:** exceeding temperature limits or a rate of increasing temperatures is often a warning of a major component or system failure.
- Pressure measurement: a tendency to over-pressure or low pressure may be an indication of obstruction or a loss of vital system fluids.
- Acceleration: higher acceleration readings than normally recorded may indicate component overstress or an abnormal wear occurrence. The use of low-cycle fatigue algorithms may indicate blade fatigue which could result in blade failure.
- Particle detection: metal particle detection may indicate higher than normal metal composition in an engine or gearbox oil system resulting from abnormal or excessive wear of a bearing which certainly will fail.
- Signal oscillation: cause may be a defective sensor or a mechanical issue with gears. By building a space state plot of a correlation $\dot{R}(x,y) * R(x,y)$ the origin of oscillation can be determined.

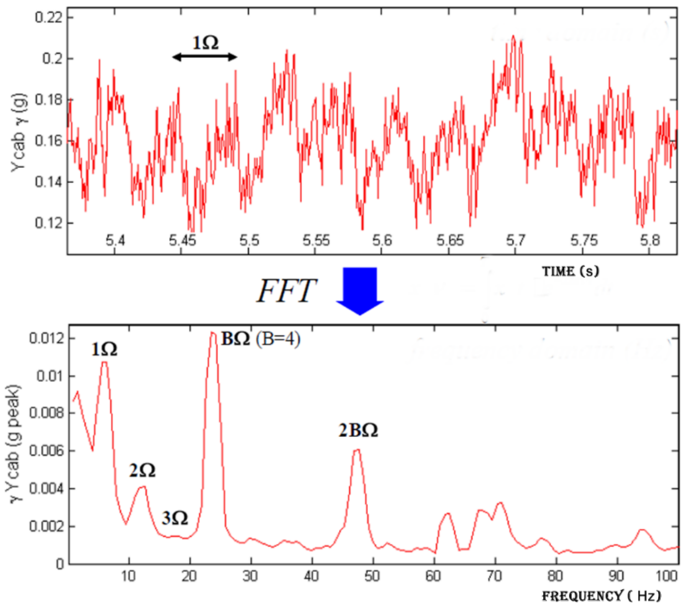

Figure 6: Direct FFT from the raw signal (*B* means the number of rotor blades, Ω is the rotor rotation) (7)

Table 1: Indicators in the frequency domain (7)

Frequency	Defects	Illustration
1Ω is the rotation frequency of the monitored rotor (or shaft)	imbalance, the result of torque loss, part damaging as crack	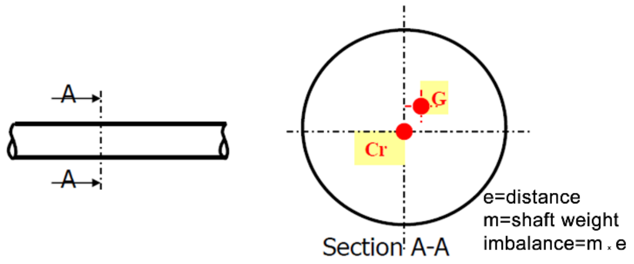
2Ω is twice the rotation frequency of the monitored shaft or rotor	shaft misalignment, shaft cracks, rotor track (RTB)	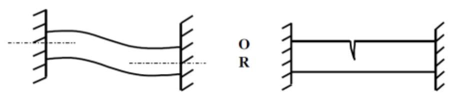
xΩ is the mesh frequency for gears	Gear tooth damage and weariness	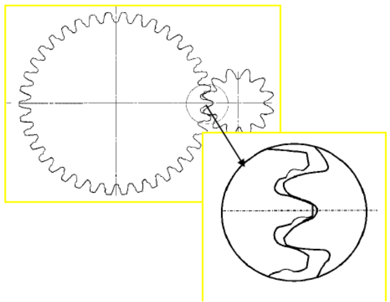
Modx is the amplitude of meshing frequency sideband gears	Gear cracks or hub cracks	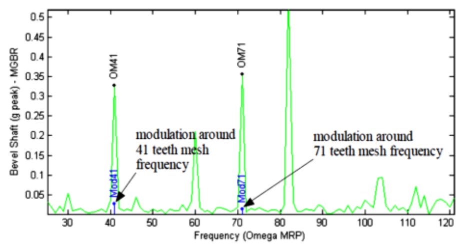
F_i, F_e, F_b, and F_c (bearing indicators)	Bearing damages detection and location	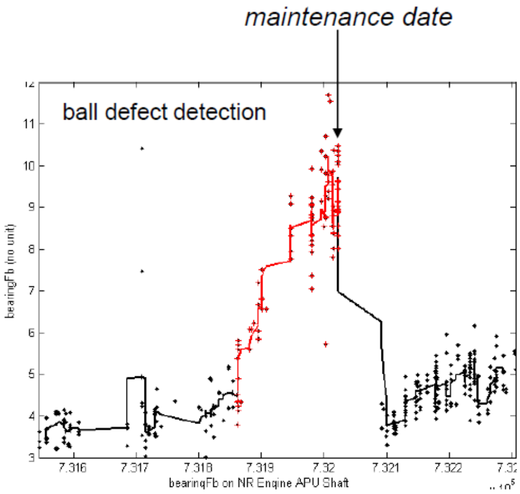

3. Noise

3.1 General considerations and physics

Noise pollution represents one of the main challenges to the aeronautical community due to the absolute necessity to reduce the noise exposure of the areas adjacent to airports or heliports. It is known that the noise exposure to the crew and especially the passengers and the people around landing and take-off areas represents a great issue.

Aircraft noise can cause community annoyance and has a large impact on people's health. There are records of restlessness in sleep, poor school performance, and increased risk of cardiovascular disease in people living in the vicinity of airports (9).

In some airports, noise restrains air traffic operations. The Frankfurt-am-Main Airport has introduced innovative noise abatement procedures. Respite periods are one of the measures brought about by the successful Dedicated Runway Operations (DROps) project. DROps operations gave affected communities scheduled breaks from aircraft noise at night or during the early morning hours (10). After this, the Alliance for Noise respite periods initiative to develop noise respite periods came into force. Many companies are part of the project and trial operations for noise respite periods started on 23 April 2015. This measure aimed to provide noise stoppage in combination with the six-hour nighttime curfew from 23:00 to 05:00 at the Frankfurt Airport. This affected some communities lying under approaches and departure routes (10).

The sound is a hearing sensation generated by a short time fluctuation of pressure. The sound mechanisms are emission (Figure 7), propagation, and reception.

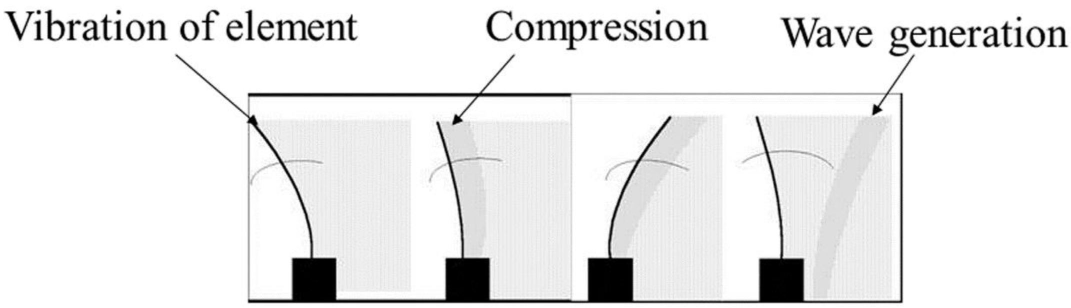

Figure 7: Emission of sound: no vibration, no sound (7)

The human ear does not have the same sensitivity to all frequencies. It is most sensitive at frequencies between 2 kHz and 5 kHz, and least sensitive at high and low frequencies, as illustrated in Figure 8. The long exposure to main rotor frequencies impacts instrument reading capability and causes fatigue and loss of control capacity.

Noise generated by aircraft is a particular case, as it has a wide variable spectrum and a transient intensity-time relationship. For this reason, special rating scales have been developed, which are based on sound annoyance rather than sound intensity, and which contain factors that consider special spectral characteristics and sound persistence. The intensity considered in this case is not the physical one, but the one that our ears perceive. Many other units, such as the dBA, were developed to assess the more general impact of present day-to-day noise and are associated with intensity. The Perceived Noise Level (PNL, which has the PNdB unit) and effective perceived noise (Effective Perceived Noise Leve - EPNL, which has the EPNdB unit) scales are related to the annoyance caused by aircraft. However, the effective perceived noise level is a complex unit, so the use of dBA is more common to measure aircraft noise in some uses, including airport restrictions, where it is important that monitoring is as simple as possible. possible, and that is comparable with other sounds.

The human ear is sensitive to the timeframe it is exposed to incoming sound waves. The following pressure level is used to measure the exposure to sound

$$L_{eq} = 10\, log\left(\frac{1}{T_0}\sum_i 10^{L_{Ai}/10}\Delta t_i\right) \tag{1}$$

where T_0 is a reference timespan (day, month, year) and L_{Ai} is dB(A) level during the period Δt_i

The following criterium is used to measure the effects of sound exposure on health (11):

$L_{eq} < 38\ dB(A)$	*Sleep: keep quality*
$L_{eq} = 65\ dB(A)$	*Office: strong discomfort, tired feeling*
$L_{eq} > 85\ dB(A)$	*Workshop: risk of deafness increases with years of exposure*

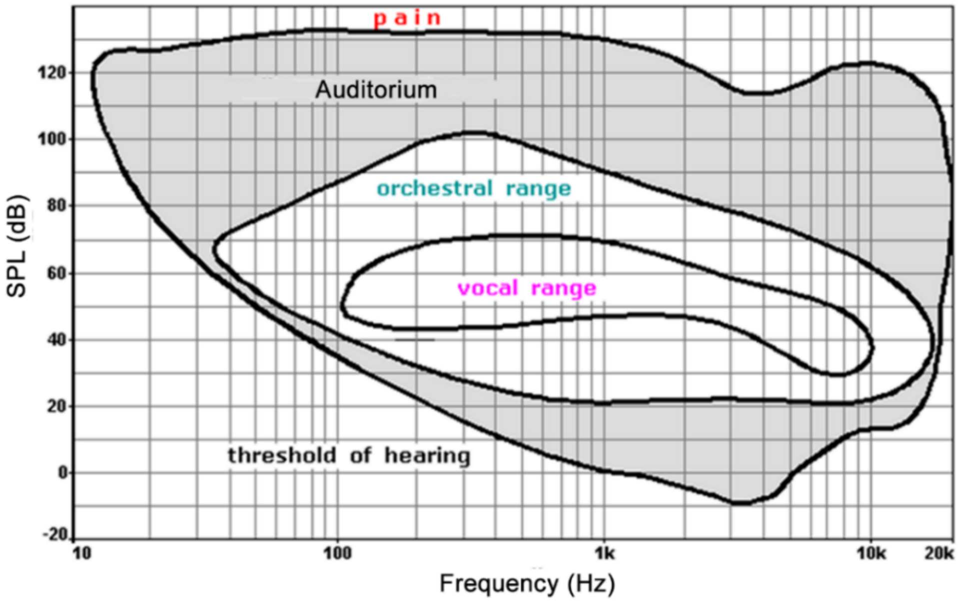

Figure 8: Human sound perception is highly dependent on frequency (11)

The main noise sources found in transport airplanes are shown in Figure 9 and Figure 10. Aircraft systems also generate noise: flight control actuators, auxiliary power units, air cycle machines, and others. Windows, gaps, rain gutters, handgrips, antennas, and skin ripples contribute to the thickening of the boundary layer and therefore increase airframe noise.

Thanks to the advances in technology and the utilization of high-bypass turbofan engines the engine-generated noise has been reduced considerably. Thus, the noise generated by high-lift devices and landing gear has recorded a percentual increase at the landing and approach flight phases.

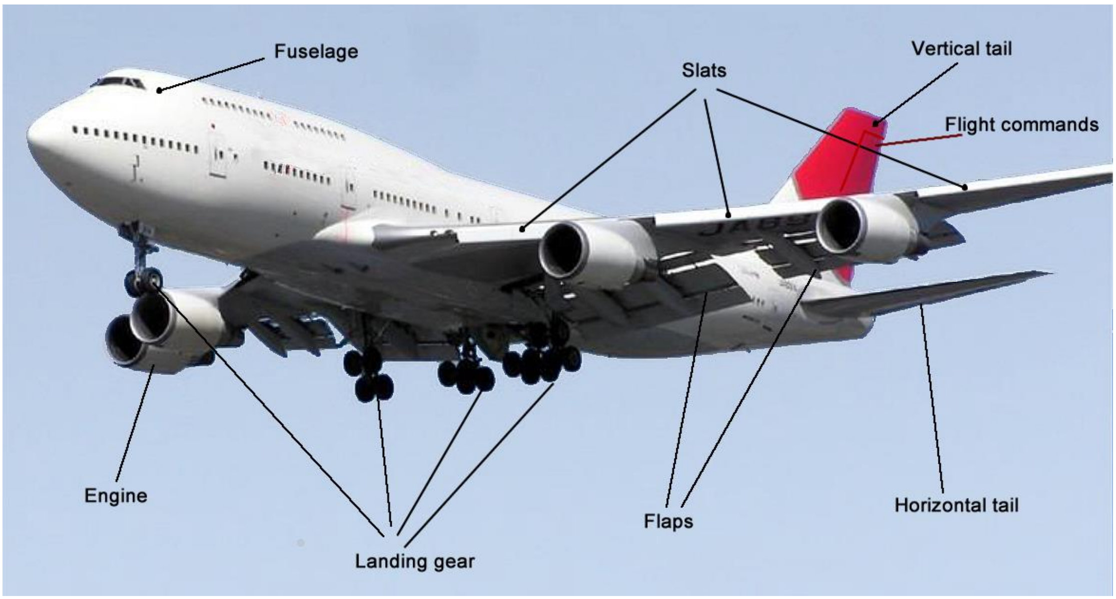

Figure 9: Airplane noise sources (12) [Edition of a public domain photo]

Airplane noise sources are normally divided into two basic groups: engine noise and airframe-generated noise. Each of these two groups is further divided into its components as shown in Figure 10 The noise of each of these components can be analyzed according to its origins as follows. Fan and compressor noise originates essentially from pressure fluctuations and interactions due to the airflow over rotating components. They are composed of **(12)**:

- Noise emitted from the fan or compressor inlet duct:
    - Broadband noise.
    - Discrete-tone noise.
    - Combination of tone noise.
- Noise emitted from the fan discharge duct:
    - Broadband noise.
    - Discrete-tone noise.
- Engine core noise originates from:
    - The process of combustion.
    - Flow around internal obstructions.
    - Scrubbing of the duct walls.
    - Local temperature fluctuations.
    - Flow throughout the turbine.
    - Turbine-blade and blade-stator interactions.

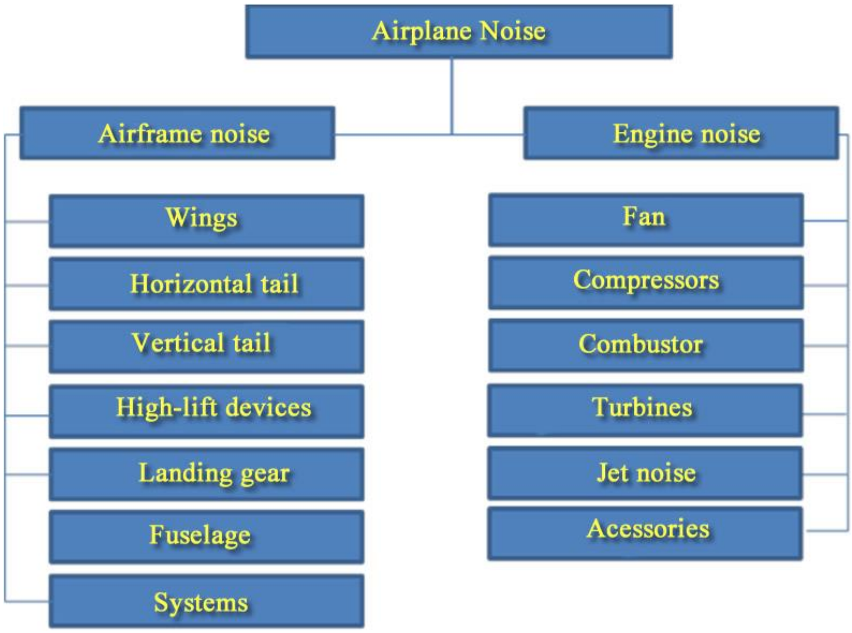

Figure 10: Airplane noise breakdown (12)

Figure 11 illustrates the procedure to calculate the effective perceived noise generated by a flying aircraft from widespread and known parameters.

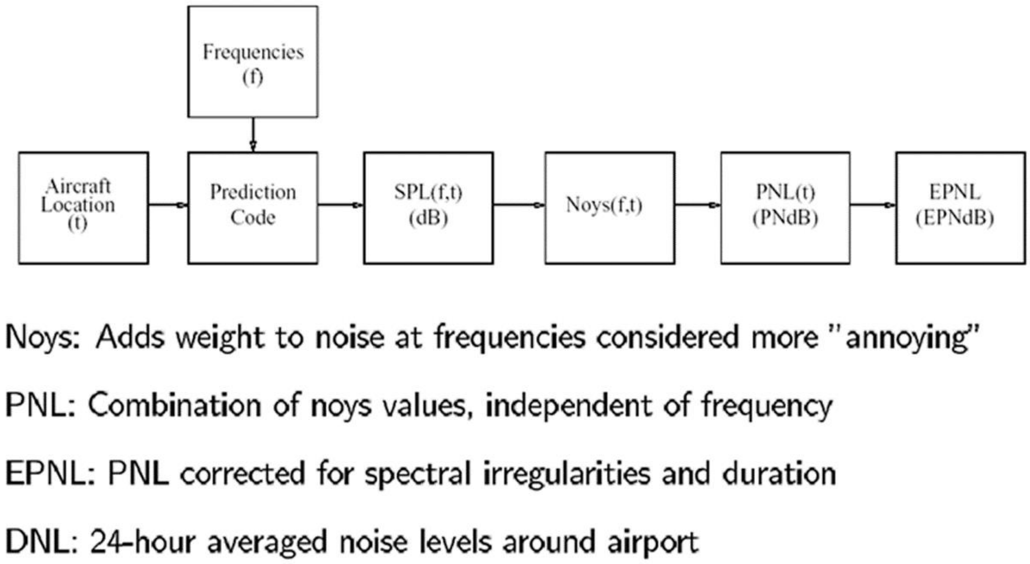

Figure 11: Calculating the effective perceived noise

It is important to differentiate sound pressure level (SPL) from sound power level (SWL). "Sound power or acoustic power is the rate at which sound energy is emitted, reflected, transmitted, or received, per unit time" (13). SPL depends on the distance and position/location of the source and the environment itself. Ambient, reflections on surrounding surfaces, and absorbing materials will influence the reverberation, sound propagation, as well as damping of the sound. Its unit of measurement is dB. SPW is not dependent on distance, position, or environment. This reveals a very important difference between both parameters. Indeed, SWL is a theoretical concept, and it is not directly measurable. Thus, a determined noise source presents the same sound power independent of its location and it provides a direct comparison between two sound sources.

At low frequencies, the absence of effective acoustic absorption materials requires the search for satisfactory alternative solutions for noise control, such as the application of reactive devices. The acoustic characteristics of reactive silencers are determined only by their geometric shape (without the use of acoustic absorption materials). These devices are designed in such a way as to let a fluid pass by greatly reducing its sound energy. As an example, one can mention compressor silencers, automotive engine exhausts, etc.

The principle of these silencers is based on the reflection of the waves to the source, that is, the waves, when passing through the silencer, find a change in the acoustic impedance of the medium, for a very large or very small value. Then, a small portion of the energy propagates through the silencer and most of the energy is reflected in the source. These silencers are economical and have a low-pressure loss of the loaded fluid.

3.2 Computational aeroacoustics

Only the hybrid or acoustic analogy methods method for the analysis of noise generation is addressed in this section. Here, the flow solution is decoupled from sound propagation. In this approach, the computational domain is split into different regions, such that the governing acoustic or flow field can be solved with different numerical techniques. There is a need for two numerical solvers: a dedicated Computational fluid dynamics (CFD) tool; and an acoustic solver. The flow field is then used to calculate the acoustical sources. Both steady-state and transient fluid field solutions can be used.

There are methods based on a known solution of the acoustic wave equation to compute the acoustic far-field of a sound source. Because a general solution for wave propagation in the free space can be written as an integral over all sources, these solutions are categorized as integral methods. The acoustic sources must be known from some different computations such as a finite element simulation of a moving mechanical system or a CFD simulation of the sources in a moving medium. The integral is taken over all sources at the retarded time (source time), which is the time at that the source is sent out the signal, which arrives now at a given observer position.

All integral methods cannot account for changes in the speed of sound or the average flow speed between source and observer position as they use a theoretical solution of the wave equation. When applying Lighthill's theory **(14)** to the Navier Stokes equations, volumetric sources can be obtained, whereas the other two analogies provide far-field information based on a surface integral. Acoustic analogies are cost-effective in terms of computational efforts, as the known solution of the wave equation is used. One observer distant from the source takes as long as one very close observer. Common for the application of all analogies is the integration over many contributions, which may lead to additional numerical problems because there is addition/subtraction of many large numbers with a result close to zero. In addition, when applying an integral method, usually, the source domain is limited somehow.

Lighthill acoustic analogy

The equation of Lighthill can be derived from the mass and momentum conservation principles (14). The intent is to evolve towards a wave equation in which the acoustic source terms are explicitly present. In this derivation, the absence of mass sources in the domain is assumed. The mass and momentum equations are then given by

$$\frac{\partial p}{\partial t} + \frac{\partial u_i}{\partial x_i} = 0 \tag{2}$$

$$\frac{\partial \rho u_i}{\partial t} + \frac{\partial u_i u_j}{\partial x_i} = \frac{\partial \sigma_{ij}}{\partial x_j} + f_i \tag{3}$$

where σ_{ij} is the stress tensor comprising the viscous stresses τ_{ij} and the static pressure is represented by p. The body force in the i-direction is given by f_i.

For a Newtonian fluid, the viscous stress tensor can be written in terms of viscosity and the gradient of the velocity field as stated in Eq. 4

$$\sigma_{ij} = \tau_{ij} - \delta_{ij} p \tag{4}$$

$$\tau_{ij} = \mu \left[\frac{\partial u_i}{\partial x_j} + \frac{\partial u_j}{\partial x_i} - \frac{2}{3} \frac{\partial u_i}{\partial x_i} \delta_{ij} \right] \tag{5}$$

If the time derivative of the mass equation and the divergence of the momentum equation are taken, these equations can be combined to obtain Equation (6). By linearizing the pressure and the density and subtracting the term $c_0^2 \frac{\partial^2 \rho'}{\partial x_i x_i}$ from both sides, (6) can be rewritten as (7). The linearization is carried out around the uniform free-field pressure and density. This is only valid for very small perturbations on the free field conditions, which is the case in general acoustics.

$$\frac{\partial^2 \rho}{\partial t^2} = \frac{\partial^2 (\sigma_{ij} + \rho u_i u_j)}{\partial x_i \partial x_j} - \frac{\partial f_i}{\partial x_i} \tag{6}$$

$$\frac{\partial^2 \rho'}{\partial t^2} + c_0^2 \frac{\partial^2 \rho'}{\partial x_i \partial x_i} = \frac{\partial^2 T_{ij}}{\partial x_i \partial x_j} - \frac{\partial f_i}{\partial x_i} \tag{7}$$

On the left-hand side, the wave equation is obtained for the perturbation of the density, with $\rho' = \rho - \rho_0$, where ρ_0 is a reference value in a medium at rest for density. In this equation, the right-hand side contains the acoustic source terms. The last term is the contribution of body forces. The T_{ij} is referred to as Lighthill's stress tensor and is given by

$$T_{ij} = \rho u_i u_j - \tau_{ij} + (p' - c_0^2 \rho') \delta_{ij} \tag{8}$$

The three terms of Lighthill's stress tensor that are responsible for the production of sound are:

- $\rho u_i u_j$ related to non-linear convective forces
- τ_{ij} viscous forces
- $(p' - c_0^2 \rho') \delta_{ij}$ is related to the deviation from isotropic conditions

The term $P_{ij} = p' \delta_{ij} - \tau_{ij}$ is the stress tensor that includes viscous stresses and $p' = p - p_0$ is the acoustic pressure, with p_0 taken as a reference value.

For turbulent flows, the viscous term in the Lighthill's stress tensor will be small and T_{ij} can be approximated by $T_{ij} \approx \rho u_i u_j$. Furthermore, if the Mach number is sufficiently small the density ρ can be replaced by the ambient value ρ_∞, resulting in the following equation for the acoustic density fluctuations

$$\frac{\partial^2 \rho'}{\partial t^2} + c_0^2 \frac{\partial^2 \rho'}{\partial x_i \partial x_i} = \rho_\infty \frac{\delta^2 u_i u_j}{\partial x_i \partial x_j} \tag{9}$$

Method of Ffowcs Willians and Hawkings

The Ffowcs Williams-Hawkings (FWH) equation represents an extension of the original work of Lighthill on the aerodynamically generated sound and governs the noise generated by a moving body immersed in a fluid. It is derived from the fundamental conservation laws of mass and momentum, expressed in terms of generalized functions, by representing the presence of the body as a *discontinuity* in the computational domain. These equations will reduce the computational expense in comparison to the solution of Curle's analytical solution (15).

The Ffowcs Williams and Hawkings wave equation can be derived from the Navier-Stokes equations. The idea of this derivation is to force every variable to be zero inside a predefined volume. To achieve this, the wave equation should be modified in such a way that it is valid in the whole flow domain. This way the free field Green's functions can be applied to the inhomogeneous wave equation in the entire domain. This manipulation is done by multiplying the Navier-Stokes equations by the Heaviside step function. This function has the following properties.

$$\begin{aligned} H(f) &= 0 \; for \; f < 0 \\ H(f) &= 1 \; for \; f > 0 \end{aligned} \tag{10}$$

This implies that f < 0 inside the body and f > 0 outside the body therefore in the fluid domain. The function f is a function of the *x*-coordinate. Now let control volume be denoted by *V*, enclose the solid body, and denote the surface of the volume by *S*. Then function f must be chosen such that

$$\begin{aligned} f(x) &< 0 \; if \; x \in V \\ f(x) &= 0 \; if \; x \in S \\ f(x) &< 0 \; if \; x \notin V \end{aligned} \tag{11}$$

Now the Navier-Stokes equations are multiplied by the Heaviside function. This way the equations apply to the fluid domain and the variables inside the control volume are zero.

$$H(f)\left[\frac{\partial p}{\partial t} + \frac{\partial u_i}{\partial x_i}\right] = 0 \tag{12}$$

$$H(f)\left[\frac{\partial \rho u_i}{\partial t} + \frac{\partial}{\partial x_j}\{\rho u_i u_j - \sigma_{ij}\}\right] = 0 \tag{13}$$

Combining these two equations and using the isotropic relation $dp = c_0^2 d\rho$, we obtain the Ffowcs Williams and Hawkings equations given by

$$\begin{aligned} \frac{1}{c_0^2}\frac{\partial^2 p'}{\partial t^2} - \frac{\partial^2 p'}{\partial x_i \partial x_j} = \frac{\partial^2}{\partial x_i \partial x_j}\{T_{ij} H(f)\} - \frac{\partial}{\partial x_i}\{[\sigma_{ij} n_j + \rho u_i (u_n - v_n)]\delta(f)\} \\ + \frac{\partial}{\partial t}\{[\rho v_n + \rho(u_n - v_n)]\delta(f)\} \end{aligned} \tag{14}$$

Here u is the velocity of the fluid and v is the velocity of the surface. For both velocities the subscript i indicates the direction of the velocity and subscript n indicates the normal component. The $\delta(f)$ is the Dirac delta function, which appears from the gradient of the Heaviside function. In Eq. 14 again the sources of sound can be identified. The first term is the contribution by the quadrupoles in the volume as represented by the Lighthill stress tensor. The other two terms are due to the distribution on the control surface because the $\delta(f)$ is zero except at the surface, $f = 0$.

In the Fluent code (16), the contribution of the volume integral is neglected. This means that the quadrupole contribution of the Lighthill stress tensor is automatically excluded from the calculation. We end up with Eq. 15.

$$\frac{1}{c_0^2}\frac{\partial^2 p'}{\partial t^2} - \frac{\partial^2 p'}{\partial x_i \partial x_j} = -\frac{\partial}{\partial x_i}\{[\sigma_{ij}n_j + \rho u_i(u_n - v_n)]\delta(f)\} + \frac{\partial}{\partial t}\{[\rho v_n + \rho(u_n - v_n)]\delta(f)\} \tag{15}$$

The result is quite simple. The first source term is often called the loading term because it represents the sound generated by the forces on the body. The second term is referred to as the thickness noise, which is related to the time-dependent fluctuation of the surface.

In the result presented in Eq. 15, the integration surface is of big importance. The surface should be chosen in such a way that it is valid to neglect the contribution of the Lighthill stress tensor. For flows with dominant acoustic regions, like the slat cove, this integration surface must enclose the region, so the contributions are considered. For low Mach number flows it is valid to exclude the Lighthill stress tensor, see Pan (17).

If the surface is chosen as the surface of the solid body, which is of course impermeable and non-moving, the relation for the sound production is further simplified to Eq. 16. As can be seen the forces of the fluid on the body are the acoustic sources.

$$\frac{1}{c_0^2}\frac{\partial^2 p'}{\partial t^2} - \frac{\partial^2 p'}{\partial x_i \partial x_j} = -\frac{\partial}{\partial x_i}\left[\sigma_{ij}n_j\delta(f)\right] \tag{16}$$

Earlier reports, like Singer et al. (18), show that taking an off-body surface does not directly imply that the acoustic results will be better, even though an improved model is the case. Flow fluctuations on the body may dissipate and disperse numerically by the CFD computation before reaching the off-body surface. This will be verified with the cylinder test case by performing a simulation with an on-body integration surface and an off-body integration surface.

Eq. 17 can now be calculated using free field Green's functions in the same way as Curle's solution. The result is the pressure fluctuation generated by the unsteady forces.

$$p'_L(x,t) = \frac{1}{4\pi c_0}\iint_S \frac{(x_i - y_i)n_i\partial\sigma_{ij}(y,t_e)}{R^2\partial t_e} \tag{17}$$

where the subscript L denotes the pressure perturbation produced by the loading term.

3.3 Application of noise calculation in design and analysis cases

The cylinder and airfoil-slatted configuration analyses presented in this Section were performed by Tijmen Ton and Dennis van Putten during their internship program at Instituto Tecnológico de Aeronáutica.

Cylinder validation case

The flow over a cylinder with a diameter d = 1.9 cm was calculated. The flow is characterized by a freestream velocity of U_∞ = 69.19 m/s at standard sea-level conditions (19), which results in a Reynolds number of about Re_d = 90,000. All simulations of the present work were performed on a PC running a Windows operational system and fitted with an AMD® Athlon™ 64 4000+ (2.42 GHz) processor and 2 GB RAM.

A discussion about the aerodynamic and aeroacoustic validation quantities is part of the content of this case. Then the results of the comparative simulations are presented. At the end of this Section, the results of the best simulation will be presented in more detail and some conclusions will be drawn regarding the follow-up simulations. The time step of the simulations was 5 x 10^{-6} and the total time was 0.2 s.

To perform a qualitative analysis of the results, some appropriate flow quantities must be chosen to use as comparative tools. These quantities must be easily accessible and comparable. Even more important is that good experimental data about them must be available. In the next sections, this is discussed for both the aerodynamic and aeroacoustic aspects of the problem. The raw Sound Pressure Level (SPL) data obtained with Fluent is a noisy signal. This data is smoothed using a locally weighted least squares quadratic polynomial technique which is robust in the sense that is resistant to outliers. The same technique is used for smoothing the Fast Fourier Transformation (FFT) of the raw C_l data. The smoothed data is used to obtain the validation quantities. The aeroacoustic data is sampled from receiver 1, the upper microphone (Figure 12).

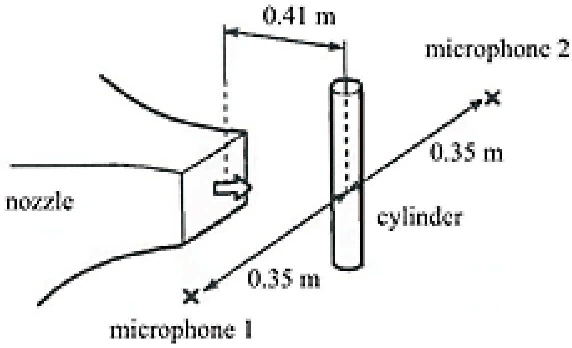

Figure 12: Experimental set-up by van der Kooi (20)

The aerodynamic flow properties that will be used to qualify the simulation results are the mean drag coefficient C_d, root-mean-square (RMS) drag coefficient $C_{d'}$, the mean lift coefficient C_l, the RMS lift coefficient $C_{l'}$, and the Strouhal number St. These quantities are defined by

$$C_d = \frac{D}{q_\infty d} \qquad C_{d'} = \frac{D'}{q_\infty d} \qquad C_l = \frac{L}{q_\infty d} \qquad C_{l'} = \frac{L'}{q_\infty d} \qquad St = \frac{f_s d}{U_\infty} \tag{18}$$

In Figure 13, the drag coefficient of a circular cylinder is given for a wide range of Reynolds numbers. As can be seen, the Reynolds region of our interest lies in a plateau of nearly constant C_d = 1.2.

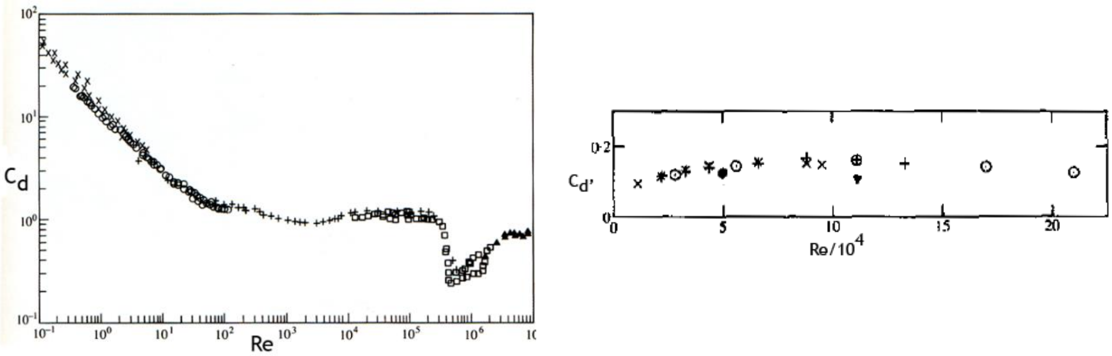

Figure 13: At left, drag coefficient vs. Reynolds number for a circular cylinder. At right, RMS drag coefficient function of Reynolds number (19)

The experimentally determined value of $C_{d'}$ can be found in Figure 12, which was presented by West (21). The reference value for $Re_d = 90{,}000$ is then $C_d' \approx 0.18$.

Regarding the flow over the cylinder, the mean lift coefficient is zero for obvious reasons. Experimental research on the time-varying lift of cylinder flow has focused on determining the RMS of the lift fluctuations. Despite a lot of efforts, however, researchers have yet not been able to agree on the correct value for $C_{l'}$ *(Re)*. In Figure 14, which is taken from Norberg (22), we consider $C_{l'} \approx 0.45 - 0.6$ for the current case under study**.**

The vortex shedding Strouhal number can be found in Figure 14 to be $St_{vs} \approx 0.19$. The figure was taken from Norberg (22).

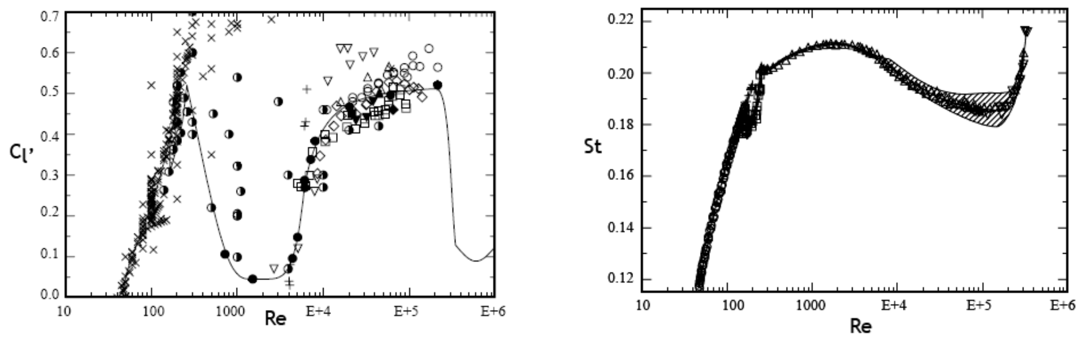

Figure 14: At left, RMS lift coefficient as a function of Reynolds number. At right, Strouhal number as a function of Reynolds number (19)

The aeroacoustic property of interest is the Sound Pressure Level (SPL) at some defined receiver locations. In the simulations, these locations were chosen to replicate the setup used by van der Kooi (20), which is depicted in Figure 12. Van der Kooi measured the SPL of a smooth cylinder at several Reynolds numbers. His results are displayed in Figure 15. The 73 m/s line corresponds to a $Re_d = 100,\ 000$. The properties of most interest are the peak SPL and the Strouhal number St_{ps} at which this occurs. The interpolated peak SPL for $Re_d = 90,\ 000$ is found to be around 107 dB at $St \approx 0.21$.

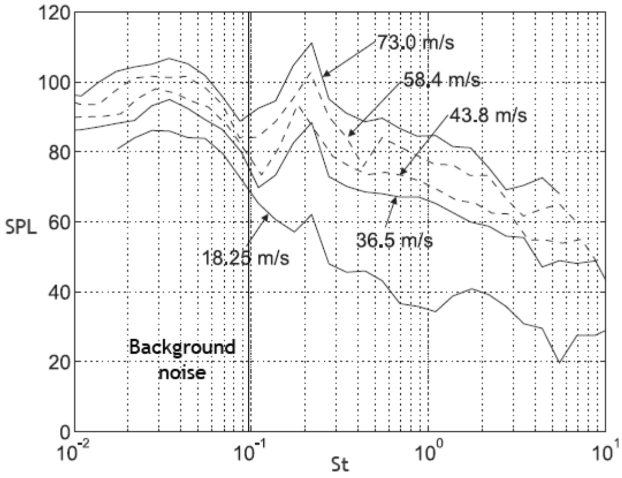

Figure 15: Sound Pressure Level as a function of Strouhal number (19)

Table 2: Summary of reference values (BM) for the benchmark cases (19)

Parameter	Value
C_d	1.2
$C_{d'}$	0.18
C_l	0
$C_{l'}$	0.45-0.60
St_{vs}	0.19
SPL (dB)	107
St_{ps}	0.21

The main conclusion from the literature study was that the influence of the SGS models on the results is quite small. To get some hands-on experience with the performance of the models it was however decided to make a comparison, nonetheless. When using the LDK model, the authors were not able to achieve convergence of the subgrid kinetic energy transport equation involved with this model. Therefore, this model was omitted from further use. All simulations were run with Interactive Time Advancing (ITA) time stepping and SIMPLEC pressure-velocity coupling. In the ITA scheme, within a given timestep, all the equations are solved in a blockwise loop until the convergence criteria for all equations are met. Thus, advancing the solution by one timestep normally requires several global iterations. With the iterative scheme, the non-linearity of the individual equations and couplings between equations are fully accounted for, eliminating the splitting error, which is caused by the segregation of the equations. This is usually overkill because the overall solution accuracy is limited by the time discretization error.

In Table 3, the results of the comparison are displayed. The differences between the results are not large. All models and Smagorinsky seem to overpredict the magnitude of the vortex shedding, because of which all values are slightly higher. Specially the fluctuation coefficients $C_{d'}$ and $C_{l'}$ are quite drastically overestimated. The agreement with the benchmark values is not fine. WALE and LDS are to be around 30% more expensive. The shedding frequency and the SPL are quite well approximated by the WALE simulation. Thus, WALE is used for all other simulations performed in this study.

Table 3: Comparison of SGS models (19)

Parameter	BM	Smagorinsky	LDS	WALE
C_d	1.20	1.486	1.433	1.525
C_d'	0.18	0.3409	0.3407	0.4555
C_l	0	0.0559	-0.0009	0.0007
C_l'	0.45-0.60	1.344	1.127	1.131
St_{vs}	0.19	0.2363	0.2258	0.1860
St_{ps}	0.21	0.2420	0.2253	0.2039
$SPL\ [dB]$	107	112.6	111.1	109.4
$CPT\ [s]$		1.07	1.37	1.35

One of the most important aspects of numerical analyses is the mesh characteristics. To evaluate the impact of mesh refinement on results three meshes were used in the calculations. The influence of wall treatment on the result is also investigated. The results of the normal grid simulation (which employs wall function) are compared to those obtained using finer meshes, which ought to resolve the full boundary layer structure. The simulations are denoted as coarse, intermediate, and fine. All simulations were performed with Non-Interactive Time Advancing (NITA) time stepping and the WALE SGS model. The NITA scheme performs a single global iteration per timestep. There are sub-iterations performed on the segregated equations within each time step, but the outer iteration (velocity-pressure iteration) is performed just once, hence the term *non-iterative*. This approach effectively drives the splitting error to the time discretization error, and it is nonzero. It must be noted that this method is only applicable for incompressible or flow with negligible compressible effects, which is the case of the present problem. The great advantage of the NITA method is the considerable decrease in computing time. Some sources give examples of a reduction in computational expense of 75% when using NITA instead of ITA. The results are displayed in Table 4 below.

Table 4: Results for different mesh sizes. BM is the reference value (19)

Parameter	BM	Coarse	Intermediate	Fine
C_d	1.20	1.202	0.6015	0.9788
C_d'	0.18	0.2902	0.1162	0.2332
C_l	0	0.0012	0.0352	0.0473
C_l'	0.45-0.60	0.9001	0.6232	0.9534
St_{vs}	0.19	0.2045	0.3027	0.2463
St_{ps}	0.21	0.2222	0.3038	0.2424
$SPL\ [dB]$	107	110.4	110.4	109.2
$CPT\ [s]$		0.55	0.51	1.78

The results of the finer meshes are somewhat disappointing. The finest mesh gives better results than the intermediate one but is in no way better than the coarsest mesh. In the intermediate case, two different vortex shedding frequencies could be distinguished. The true physical vortex shedding is not captured properly in this simulation. As observed by Piomelli (23) and Templeton (24) the near-wall vortical structures are of a very small scale, but dynamically important. SGS models are found to be incapable of capturing the correct physics associated with these small structures. This means excessively fine grid resolutions must be adopted when using this so-called *solve-to-wall* approach. Refining the grid in a wall-normal direction creates cells with a bad aspect ratio, which in LES is found to give bad results. This means that all directions must be refined, because of which the necessary resolution approaches that of a full DNS simulation. In both the fine mesh simulations Fluent adopts the *solve-to-wall* approach, although the resolution is not nearly as high as necessary to capture the correct physics. This is probably the main reason for the failure of the finer mesh simulations. The wall-modeling technique used in conjunction with the coarse grid seems to perform adequately and will therefore be adopted in the other more complex cases. It should be noted that the comparison of CPT between the coarse and finer grids is not representative, because the structure of the grids (and their qualities, which influence convergence) differs somewhat. It is however clear that in the case the meshes are structurally comparable, a lower number of cells results in a lower expense.

This section will investigate the influence of the integration surface used in conjunction with the Ffowcs Williams and Hawkings Equation (Eq. 17). The mesh and integration surfaces used for the simulations were discussed previously. The results of the simulations are displayed in Table 5 below. Because the only difference between the simulations is found in the acoustics, only these quantities are given.

Table 5: Comparison of integration surface (19)

Parameter	BM	On-cylinder	Off-cylinder
St_{ps}	0.21	0.2087	0.2087
SPL [dB]	107	106.4	106.2

It appears that the assumption that the sound generated in the off-body region is negligible is indeed valid in this case. The choice of integration surface hardly alters the outcome. This is not the case for the slatted-airfoil configuration and will be discussed later.

The results presented here are the best ones (Table 6 and Table 7). Excellent visualization of the vortex shedding behavior is formed by a filled contour plot of the velocity magnitude, as given in Figure 16. The vortex shedding character is visible from the low/high-velocity pairs which indicate an alternating sequence of clockwise rotating vortices shedding from the upper side and counterclockwise rotating vortices that are shedded by the lower side.

Table 6: Aerodynamic coefficients for the circular cylinder (19)

Parameter	BM	NITA
C_d	1.20	1.202
C_d'	0.18	0.2902
C_l	0	0.0012
C_l'	0.45-0.60	0.9001
St_{vs}	0.19	0.2045

The SPL spectrum produced by this simulation is displayed in Figure 17. The included experimental data was obtained from an interpolation of the 73.0 m/s and 58.4 m/s datasets of van der Kooi to correct deviating Reynolds number. The agreement with the experimental data is very good. The peak SPL and its corresponding Strouhal number are predicted well. The global deviation is however around 12 dB, which is considerable.

Table 7: Aeroacoustics results for the circular cylinder (19)

Parameter	BM	NITA
St_{ps}	0.21	0.2222
$SPL\ [dB]$	107	110.4

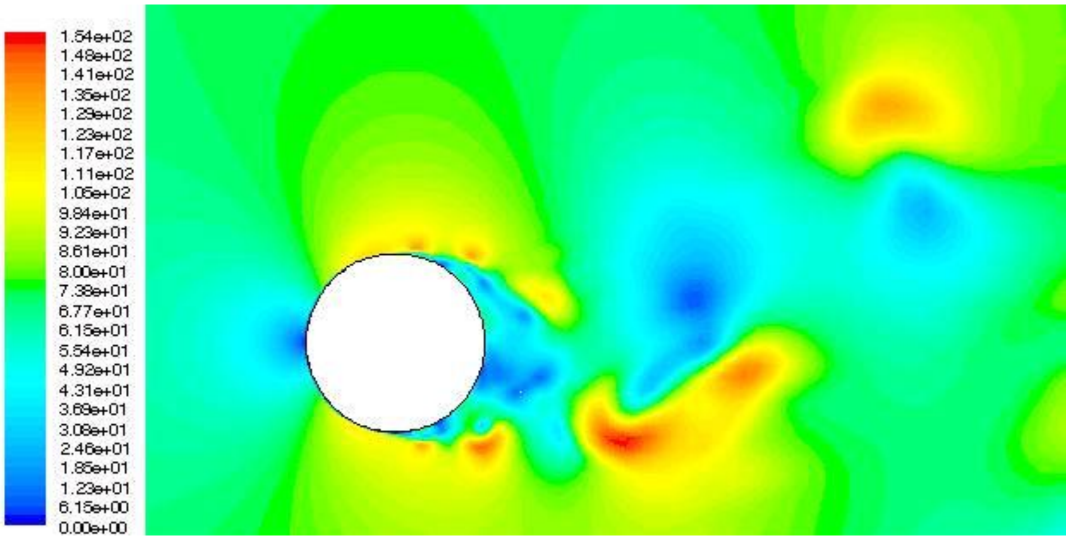

Figure 16: Contours of velocity magnitude @ time = 4.66 x 10^{-1} s. Simulation using NITA and WALE (19)

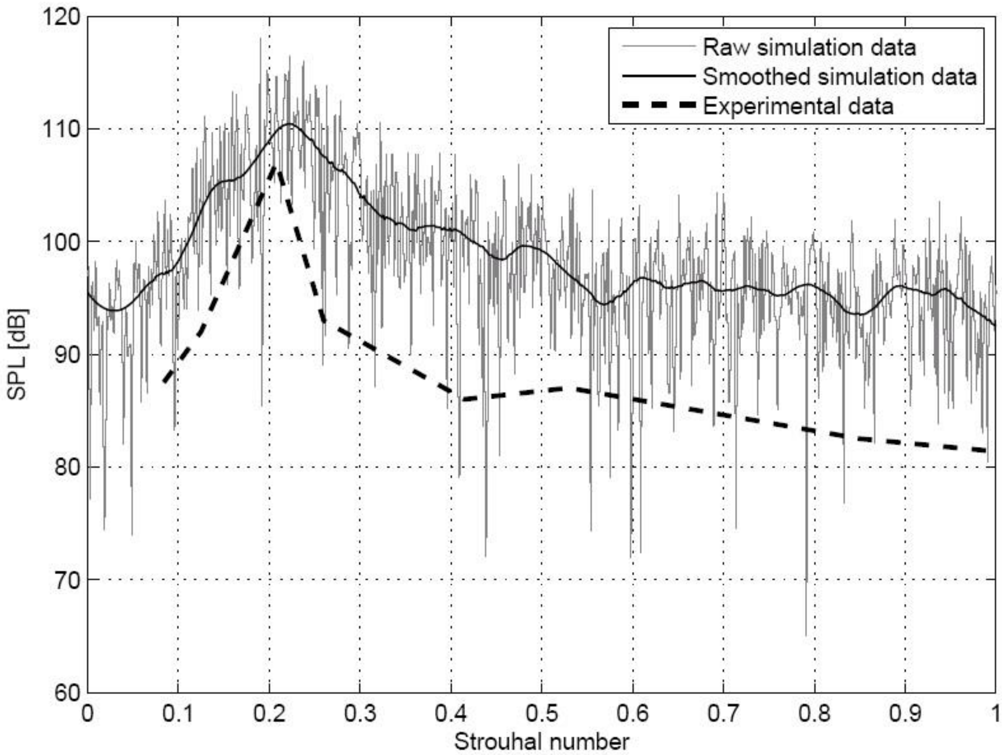

Figure 17: Sound pressure level at receiver 1 (19)

Airfoil with deflected slat

Most airframe noise is broadband in nature, with some low-frequency tones with low-frequency tones associated with cavities and discontinuities. Solid-body interaction with fluid may be related to the dipole noise source (25). In the quadrant where the slat noise is most present, the jet noise dominates. However, considering the low-noise signature of new generations of high by-pass turbofan engines, the slat noise may become the major contributor in this quadrant.

The flow over a deflected slat configuration is considerably complex and is characterized by a vortex in the slat cove region (Figure 18). One approach to reduce the noise caused by the deflected slat is to evaluate it with different horizontal and vertical separations to the main component of the airfoil and then utilize a surface response method to obtain the best configuration. However, techniques to reduce the noise level must consider the requirements of ice protection and the maximum lift coefficient provided by the slat.

The noise-generating mechanisms of slats are (25):

- Unsteady flow separation at the cusp of the slat
- Unsteady mass fluctuations in the slot
- Unsteady motions of the vortex in the slat cove region

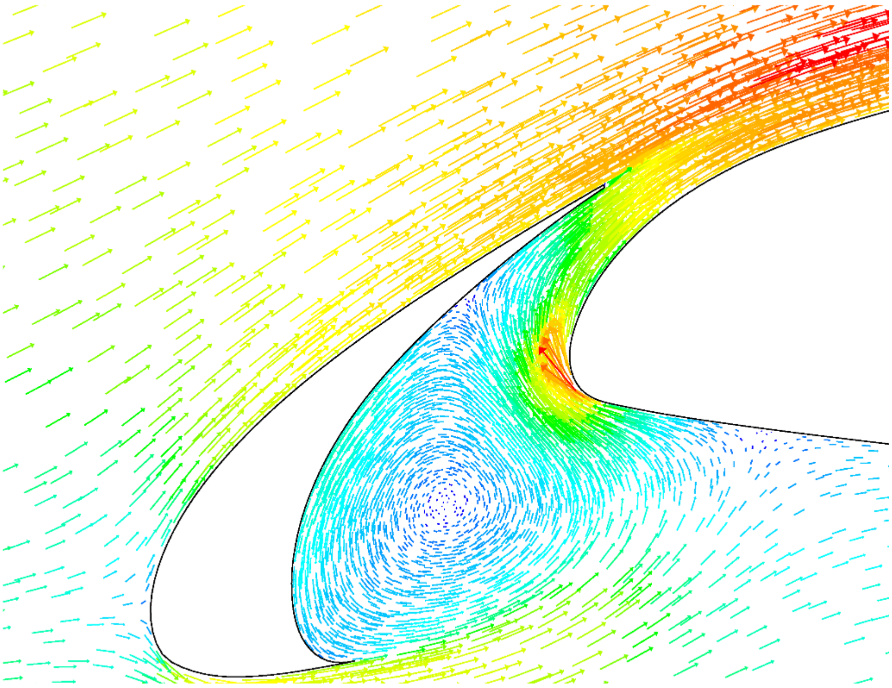

Figure 18: Navier-Stokes flow over a slat configuration showing a strong vortex behind the slat. The picture also allows for the inference of the location of the stagnation points on the slat and main airfoil ($M_\infty = 0.30, \propto = 0^o$)

An acoustic analogy is employed for the noise prediction of a slatted-airfoil configuration (19). The flow was simulated using Large Eddy Simulation (LES) approach and the acoustic propagation is successively calculated with the Ffowcs Williams and Hawkings method (26). For the LES a relatively fine mesh is required. The time step must be limited due to the acoustical calculation, and the spectrum was calculated for the whole audible range (20-20,000 Hz).

The geometry and computational domain of the high-lift airfoil are shown in Figure 19 and Figure 20. As can be seen in Figure 20, the slat and the slot region are bounded by the dashed line, representing a surface used for the computation of sound radiation. A report of Andreou (27) is used for validation of a numeric run that employed the Fluent code (16). The aeroacoustic measurements are done on the tunnel floor by an array of microphones. The vertical distance between the microphone array and the wing was 0.6 m. The use of two different arrays resulted in measurement with a frequency range between 2 kHz and 20 kHz. The validation of the simulation was performed in this bandwidth. The acoustical emission outside this bandwidth will be discussed as well. Especially the contribution in the audible range will be looked at.

Three measurements were performed at α = 6º, 10º, and 16º. Ref. (27) does not only discuss the aeroacoustics of the configuration but also provides important aerodynamic data. The acquired data was corrected due to the perturbation caused by wind-tunnel walls, wake vortex sheet hitting the wind tunnel, and blockage of the model that was tested.

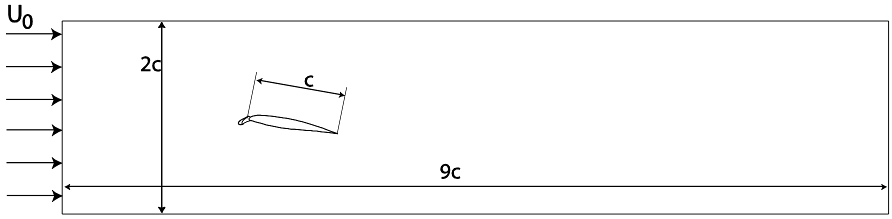

Figure 19: Computational domain for the airfoil slatted configuration (19)

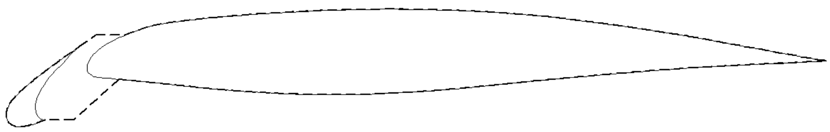

Figure 20: Airfoil configuration being investigated (19)

The report by Andreou focuses on the determination of the sources of sound. The setup with the microphone array can pinpoint the sources of sound. Figure 21 shows the experimental data for different frequencies at an angle of attack of 6º. The leading and trailing edge of the airfoil is indicated by the thick black lines. The slat is the main contributor to the noise generation of the overall configuration.

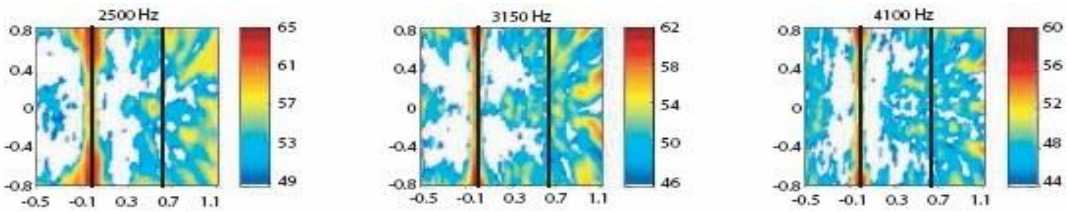

Figure 21: Sound pressure pattern for α = 6º (27)

The source location can also be determined with Fluent (16). This is done by plotting the source dipole strength on the surface of the slat and airfoil. Integrating this term over the surface will give the contribution of all the sources on the surface to a specified observation point. The source dipole strength is given in Figure 22 for α = 6º. The slat, the slot, and the leading-edge region of the main wing are the main sources of sound. The dipole strength on the upper surface of the main wing is not measured in the experiments and therefore is not shown in Figure 23. The source dipole strength for the case of 16º angle of attack is very strong at the upper surface. This indicates that there is a lot of noise radiation upwards, which was unfortunately not tested in the wind tunnel. Also, the sound pressure level at the tunnel floor was measured in the experiment. Our corresponding acoustic simulation was performed with eight receivers at the lower tunnel floor, with the receivers 0.1 m apart. SPL was calculated at these receiver points. It was found that there is not a significant difference between the receivers. Therefore, the sound pressure level of the receiver below the slat is used for the comparison. In Figure 23 the experimental SPL data is given for different angles of attack.

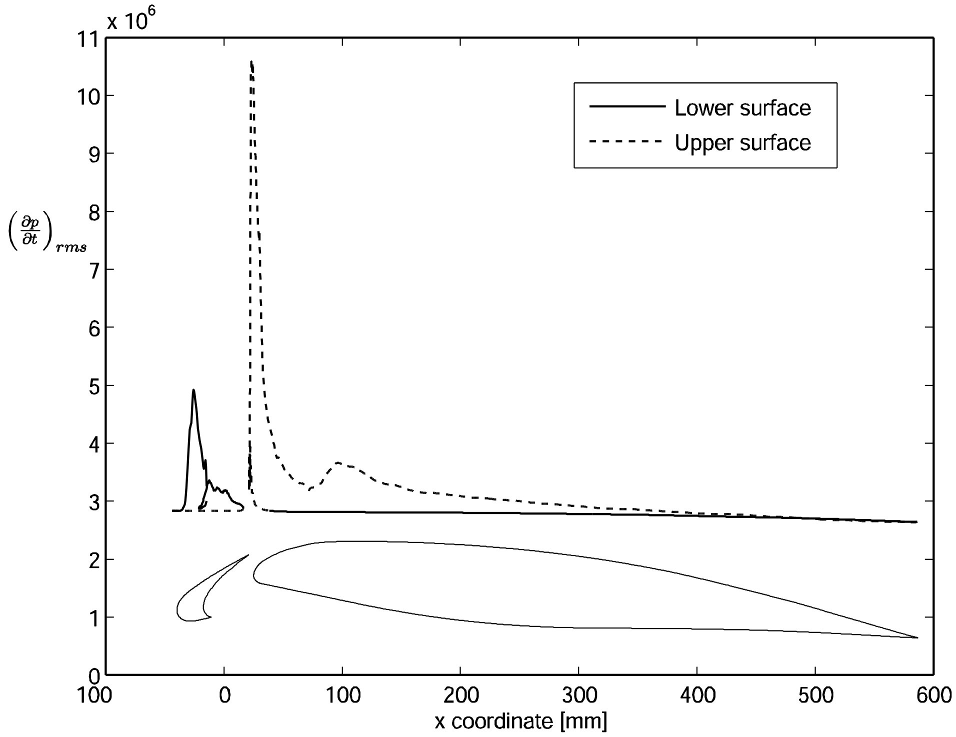

Figure 22: Source dipole strength along airfoil surface (α=6º) (19)

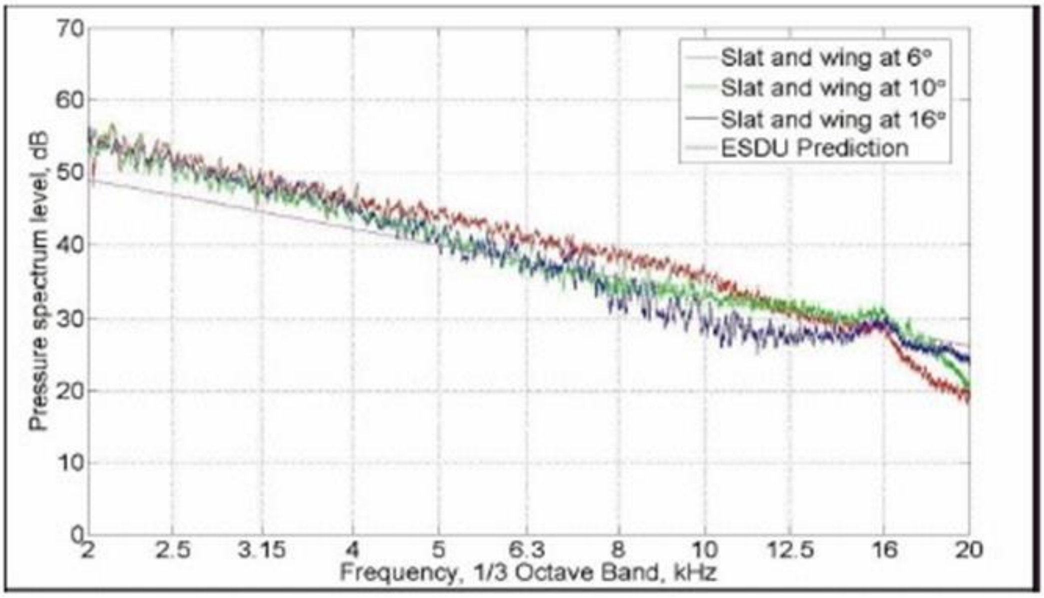

Figure 23: Experimental SPL for α = 6º, 10º, and 16º (27) (19)

The SPL over the frequency that was obtained with the numerical simulation is given in Figure 24. By using a weighted least squares method, the data is smoothed. In Figure 24, the dashed line is a regression of the experimental data, given in Figure 23. Depending on the frequency, the simulation overestimates the SPL from 5 up to 10 dB, so this result can be considered still satisfactory. The trend and specific peak frequencies must be captured properly, and the overall tendency was captured well up to a frequency of about 10 kHz. The decrease in accuracy in the high-frequency region may be accounted for by the mesh size. Literature on this topic states that often the smallest wavelength is resolved with denser meshes, specifically a refinement by a factor of about two is required, demanding a large mesh. To keep the computational expense at a reasonable level, the refinement was only applied to the slot region, because this region is the major source of the noise. The results of this simulation are shown in Figure 24.

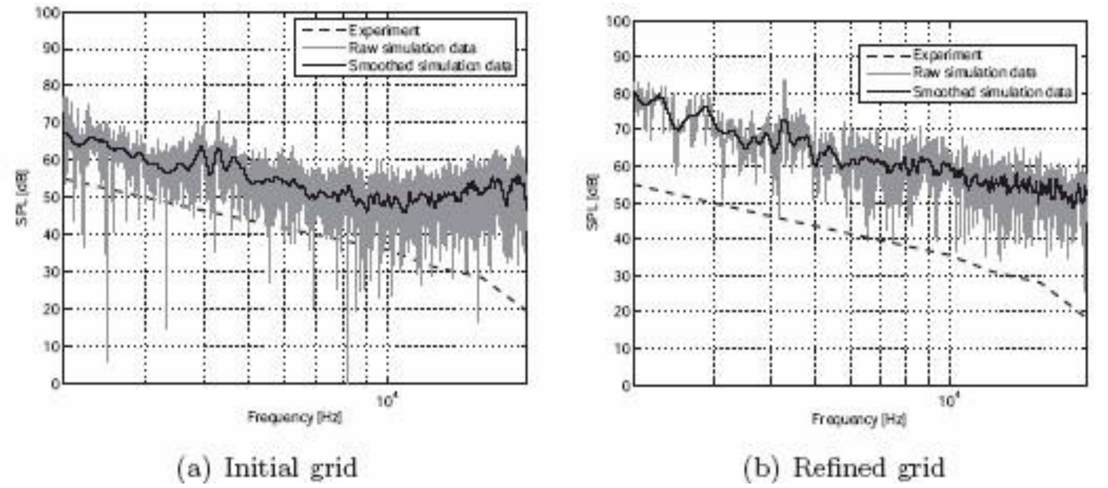

Figure 24: Experimental and computed SPL data for α = 6º (19)

According to Figure 24, the results obtained with the finer grid are not better than those with the coarser mesh. In the low-frequency region, the simulation lacks accuracy. Despite this, the trend was better captured with the finer grid, but this is just an effect of the increased SPL deviation at low frequencies. We can therefore conclude that refining only the slot region is not enough to increase the accuracy of the sound emission prediction. The refining must be extended towards the source surfaces and especially to the lower surface of the slat. It is believed that refinement in these regions will increase the accuracy, and additional simulations are needed to support this claim.

The integration surface is introduced to capture more of the physics of the problem and to obtain a better simulation of the sound production. In the benchmark case, it is proven that for the cylinder the results did not differ much. For the simulation of the slatted-airfoil configuration, two integration surfaces were used to calculate the sound emission. The results of this calculation are shown in Figure 25. For these simulations, the refined grid was used to avoid dissipative effects in the slot region. The use of two separate integration surfaces which are at a close distance is physically not realistic. In the region between the surface, reflection plays a dominant role, but it is not accounted for by the method of Ffowcs Williams and Hawkings. By enclosing this whole reflective region, this problem is avoided, and reflection is considered. The on-body surface is indeed found to perform somewhat worse when looking at the trend line, as can be seen in Figure 25.

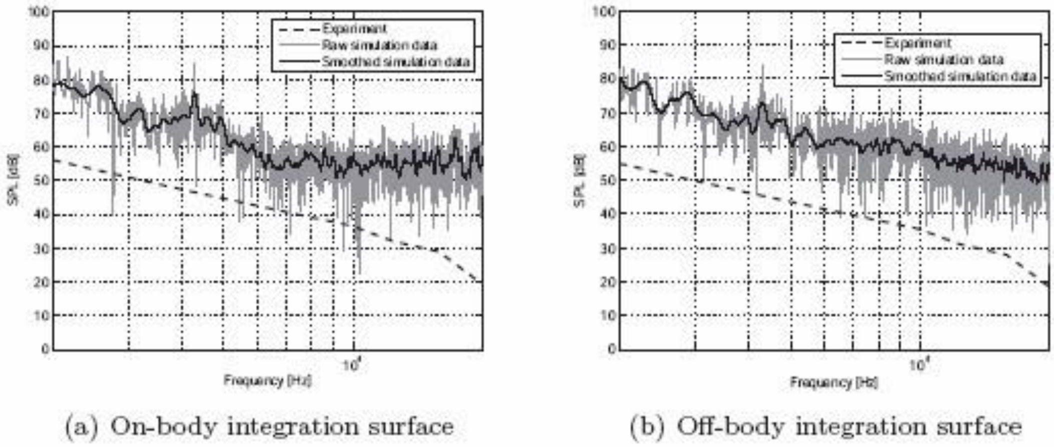

Figure 25: Sound generation from different integration surfaces (19)

In the experiment carried out by Andreou, only the frequencies between 2 kHz and 20 kHz were measured. However, the trend of the numerically obtained SPL shows that low frequencies are most dominant in the spectrum. From an engineering point of view, the bandwidth of interest extends to the low frequencies up to 20 Hz. The simulation was run long enough to also capture even lower frequencies; these results are shown in Figure 26. The region left out of the measurements of Andreou is indeed very interesting. Especially the region between 200 Hz and 1 kHz has a relatively high SPL. This region diminishes when the angle of attack is increased. This phenomenon can be ascribed to the boundary layer instability and the vortex shedding initiated from the instability at the lower slat surface. It only occurs at low angles of attack as will be clarified in the aerodynamic section.

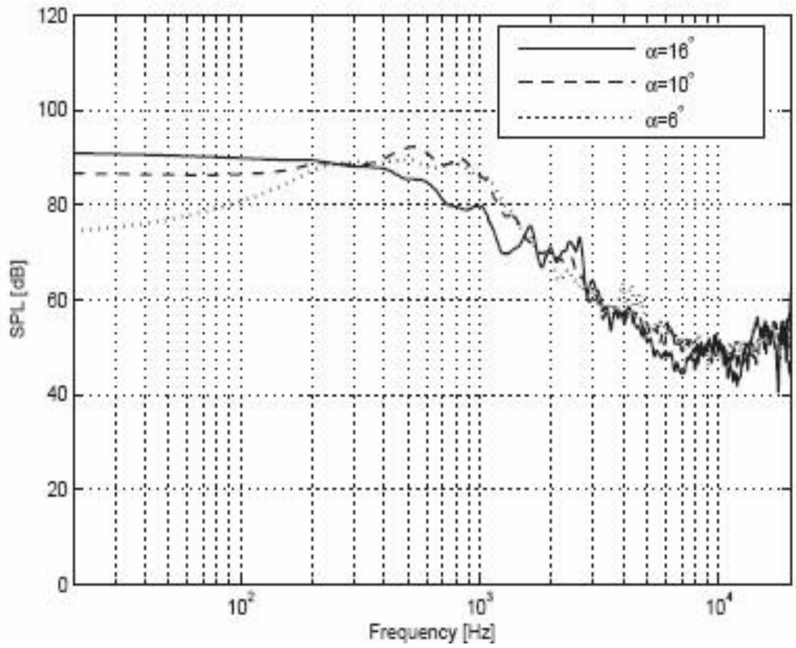

Figure 26: SPL for all angles of attacks in the audible range (19)

The same phenomenon causes the high source dipole strength on the lower slat surface, as shown in Figure 22. The instability in the boundary layer causes pressure fluctuations on the surface, which translates to sound emission. As the angle of attack is raised the boundary layer instability will occur at the upper surface of the slat.

The source dipole sound is caused by the instability of vortex formation in the boundary layer. These instabilities can be visualized by plotting the pressure distribution in the flowfield at a certain instant in time. This distribution is given in Figure 27 as the relative pressure deviation from the freestream pressure. The instability occurs at the upper surface of the main element. These fluctuations were also visible in the source dipole strength plot in Figure 22. There is also a large recirculation area visible in the slot. This region is affected by shear stress which originates from the slat trailing-edge flows.

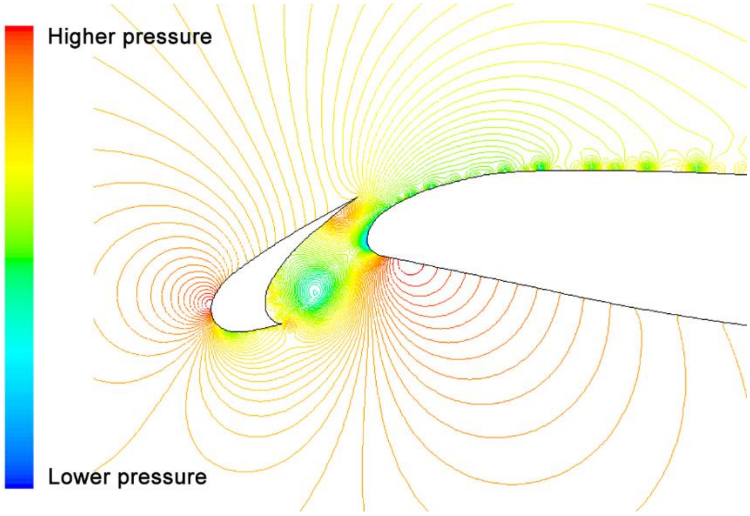

Figure 27: Iso-pressure isobar lines for α = 6º (19)

The boundary layer separation on the slat can be related to the pressure distribution on the surface. If the pressure gradient is negative the flow is accelerated, and the boundary layer will be stretched. This damps the instability and prevents the separation of the boundary layer. On the other hand, if the pressure gradient is positive, separation can occur and therefore the pressure coefficient gives a good estimation for boundary layer separation. For one instant in time the pressure coefficient along the surface is given in Figure 28. The pressure fluctuation on the lower surface of the slat is also clearly visible. Again, these results comply very well with the results found before. For graphical purposes, the slat geometry given in the Figure is stretched and does not comply with the real geometrical dimensions.

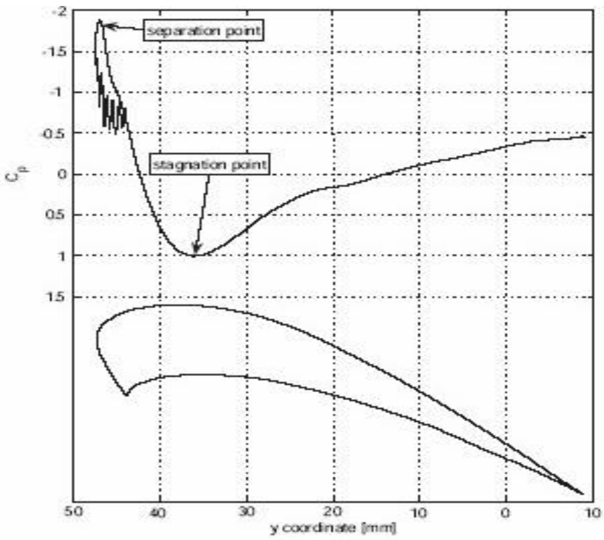

Figure 28: C_p Distribution on slat surface (α = 6º) (19)

The same can be done for the main element. Here the instability occurs at the upper surface. The pressure fluctuations are present over the whole upper surface (Figure 29). The wavelength of the fluctuations increases when traveling towards the trailing edge. This indicates that small eddies are generated near the leading edge and are convected with the flow while increasing in size. As stated before, the scale of the eddies is roughly proportional to the wavelength of the sound radiation. This means that the emission near the leading edge is relatively high-frequent and near the trailing edge low frequent. The scales of the eddies can be visualized using iso-pressure contours. This is done in Figure 30. On the lower surface a negative, or adverse, the gradient is maintained over almost the whole surface, except for the region from half the chord length up to the trailing edge. Here the pressure shows some harmonic oscillations around a nearly constant value. These fluctuations are however very small. They are caused by small eddies that are shedded from the point where the geometry changes suddenly and convected along the surface.

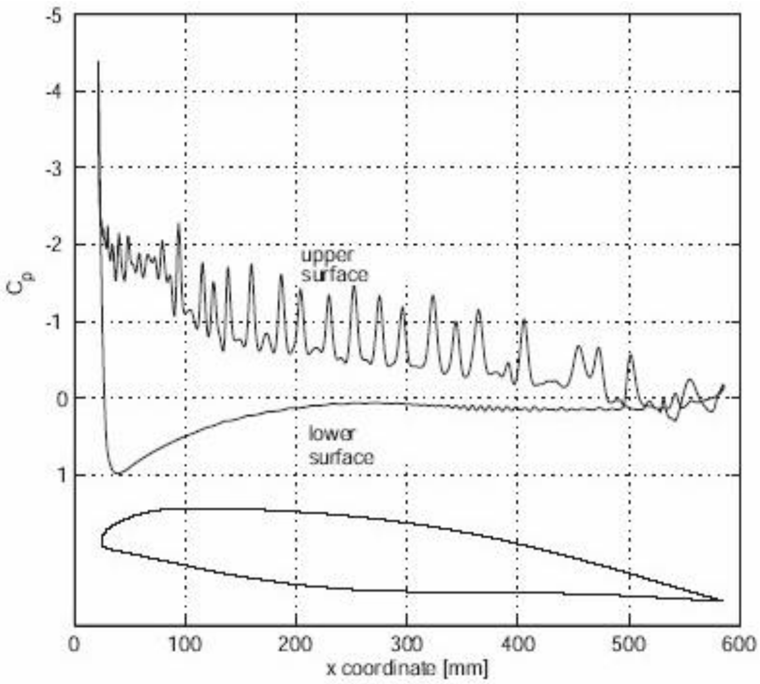

Figure 29: C_p distribution on the main element at α = 6º (19)

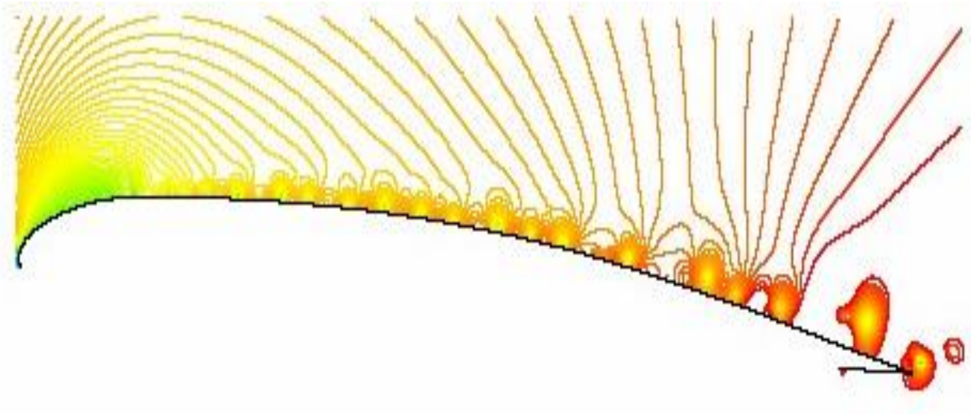

Figure 30: Iso-pressure contours on the main element at α = 6º (19)

Landing gear of a long-haul airplane configuration

White noise consists of a simultaneous combination of sounds of all frequencies. The adjective white is used to describe this type of noise in analogy to the functioning of white light, given that this is obtained through the combination of all chromatic frequencies. Proudman **(28)**, using the analogy of light waves with acoustics, derived a formula for the acoustic power generated by isotropic turbulence without mean flow. More recently, Lilley **(29)** again derived the formula but this time accounting for the delay time difference which was neglected in Proudman's original derivation. Both derivatives gave an acoustic power yield acoustic power due to the unit volume of isotropic turbulence (in W/m^3). Equation summarizes the relationship between acoustic power and flow variables:

$$P_A = \alpha \rho_0 \left(\frac{u^3}{l}\right) \frac{u^5}{a_0^5} \tag{19}$$

where u and l are the turbulence velocity and length scales, respectively, and $\boldsymbol{a_0}$ is the speed of sound. The parameter α in Equation 19 is a constant. In terms of k and ε, Equation 19 can be rewritten as

$$P_A = \alpha_\epsilon \rho_0 \epsilon M_t \tag{20}$$

with

$$M_t = \frac{\sqrt{2k}}{a_0} \tag{21}$$

Ansys Fluent **(30)** uses the above model to compute the acoustic power level in dB

$$L_P = 10\, log\left(\frac{P_A}{P_{Ref0}}\right) \tag{22}$$

A CFD simulation for an airplane similar in configuration to the A340 was carried out with Ansys Fluent **(30)**. Some characteristics of this CFD run

- Freestream Mach number of 0.14 and 3° angle of attack.
- Fluent's density-based implicit algorithm was chosen to run the simulation.
- A realizable *k-ε* turbulence model with standard wall treatment was employed. Corrections for curvature and compressibility were considered.
- The airplane analyzed was modeled with main and nose landing gear extended, including some doors at the open position.
- Airplane geometry and initial surface mesh were generated with the open-source code Sumo **(31)**.
- The final computational mesh is comprised of 7,923,665 tetrahedra.
- Mesh adaptations were performed to smooth absolute gradient values and keep the y^+ parameter within reasonable values.

Contours of surface acoustic power [dB] can be seen in Figure 31 for the main landing gear and the entire aircraft. the corner of the landing gear compartment generates considerable noise. Rounding off this edge would certainly contribute to a significant reduction in the noise level. The downstream pair of wheels is a considerable source of noise, as it receives the flow that was decelerated and separated from the front ones. Figure 32 Shows streamlines colored by velocity magnitude released in front of the main landing gear. The flow is highly disturbed by the front wheels and other cylindrical parts of the landing gear assembly.

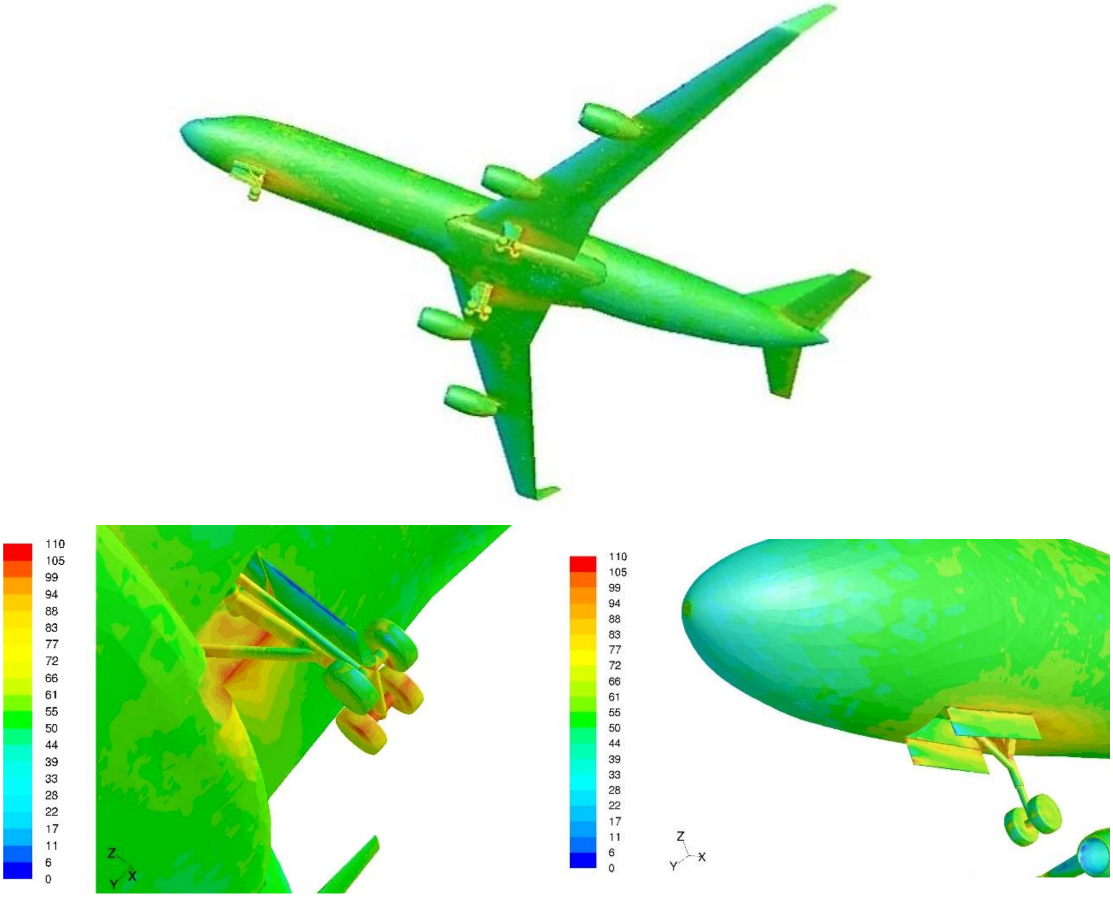

Figure 31: Contours of surface acoustic power level [dB]

The bogie incidence relative to the fuselage centerline (Figure 9 and Figure 32), as already present in many aircraft configurations, contributes to the noise reduction because a part of the wake originating on the front wheels does not impinge on the wheels located downstream. This arrangement also contributes to less mechanical vibration in the landing gear assembly. Cao et al. (32) studied the effect of the bogie pitch angle on the structural design during touchdown. Their results indicate that the overload of main landing gear, drag force, and maximum stress decrease as the initial bogie angle increases. However, the total force of the snubber increases when the initial truck angle increases. Increasing the initial bogie pitch angle at touchdown increases structural robustness (32).

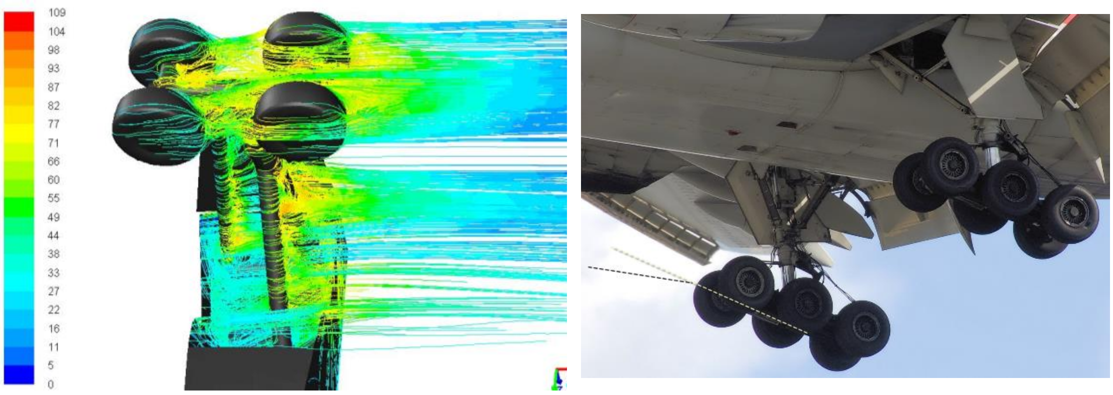

Figure 32: ***Left*** **- Streamlines close to the main landing gear of the four-engine airplane. Colors are related to acoustic power level [dB] ($M_{\infty} = 0.14, \propto = 3^{o}$).** ***Right*** **- Misalignment of wheels pairs (Photo: Adrian Pingstone, public domain)**

Ice detector

The front fuselage of airplanes must accommodate flight instruments, primary flight control, and the nose landing gear. Externally, it hosts several probes that are vital for the safety of the flight such as angle of attack sensor, total temperature probe, Pitot tubes, and ice detectors.

As ice accretes on the vibrating probe (Figure 33), the nominal natural frequency is reduced due to the ice mass. Reduction of the probe frequency below a predetermined threshold causes changes in a reference signal and the system is then activated, thus causing the protected surfaces to be deiced.

Most ice that builds up on aircraft surface owes its constitution to droplets with a size between 15 and 50 µ. An aircraft certificated to fly into known icing conditions can sustain flight in stratus-type clouds with droplet Median Volume Diameters (MVD) up to 40 µ; and flight in cumulus clouds with droplet MVDs up to 50 µ. Larger droplets present greater inertia, and their trajectories may depart significantly from the streamlines around the aircraft. As a result, larger droplets adhere to larger parts of the aircraft surface and are more likely to strike behind ice-protected surfaces. Supercooled Large Droplets (SLD) can be up to 4000 µ in diameter and, despite icing certification limitations, accidents, and incidents in SLD conditions have been documented, especially following sustained flight in freezing drizzle or freezing rain.

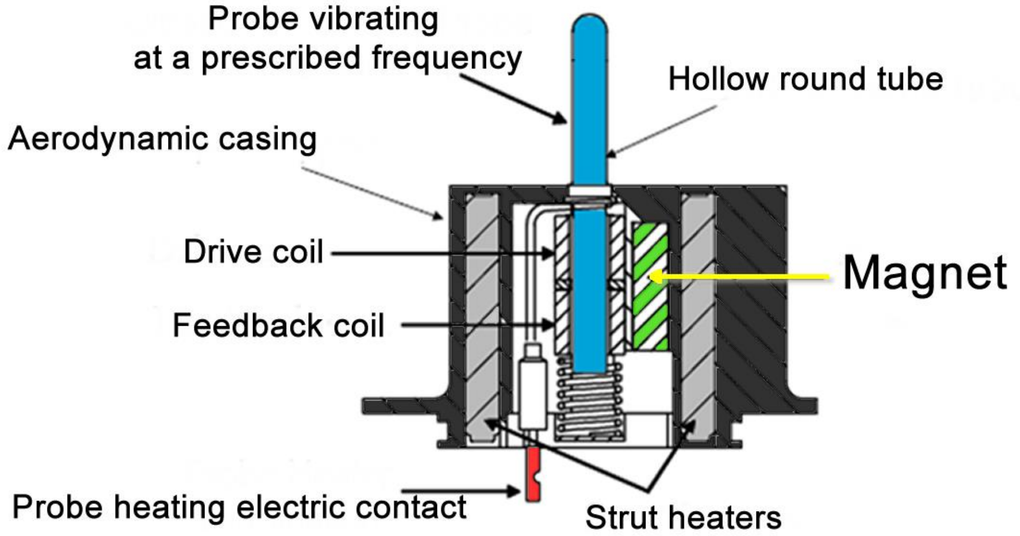

Figure 33: Magnetostrictive ice detector

Navier-Stokes simulations were carried out with the Ansys Fluent code (16) for a 55-seat airliner configuration, which was designated ITA55ADV. Fluent's realizable *k-ε* turbulence model and standard wall functions were employed in this simulation The computational model is not symmetric, with one ice probe placed only on the port side of the front fuselage in the position labeled P2 (Figure 34). This approach intends to measure the impact of the probe on the SWL, comparing the distribution on this side with the flow calculated on the starboard side, which is free from probes. Figure 34 also displays the triangular surface mesh employed in the calculation. The spatial mesh was adapted to lower velocity and pressure gradients and to keep the y+ values within reasonable values.

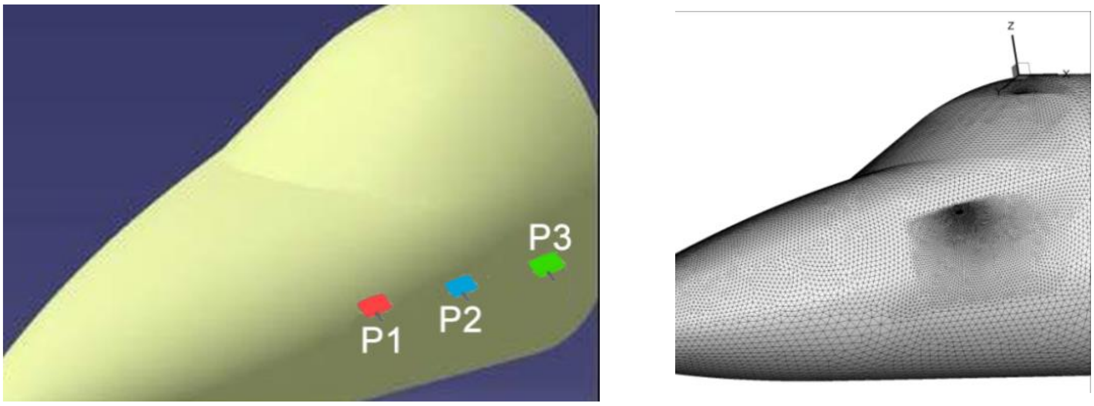

Figure 34: ***Left*** **- Locations chosen for placement of the ice detector.** ***Right*** **– Initial surface mesh in the ice-detector region generated for the P2 ice-detector configuration**

A CFD calculation was performed at freestream conditions with $M_\infty = 0.40$ and $\alpha = 3^o$. The results show that, besides the logic separation behind the cylindrical part of the probe, the flow also separates at the trailing edge of the P2 configuration according to the Navier-Stokes simulation performed with Fluent (Figure 35). The rounded trailing edge of the basis of the probe is not suited to keep the flow attached (Figure 36), namely at higher Mach numbers. Naturally, the flow behind the probe's cylindrical part is also separated for all conditions in the airplane's flight envelope. The maximum Mach number over the ice detector obtained from the CFD run was found to be as high as 0.89. Comparatively, the fuselage and wings recorded 0.58 as the highest Mach number on these surfaces.

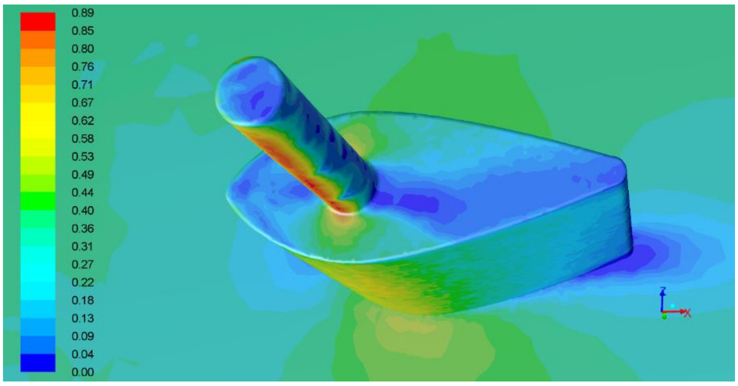

Figure 35: Mach number contours on the ice detector and its neighborhood ($M_\infty = 0.40$, $\alpha = 3^o$)

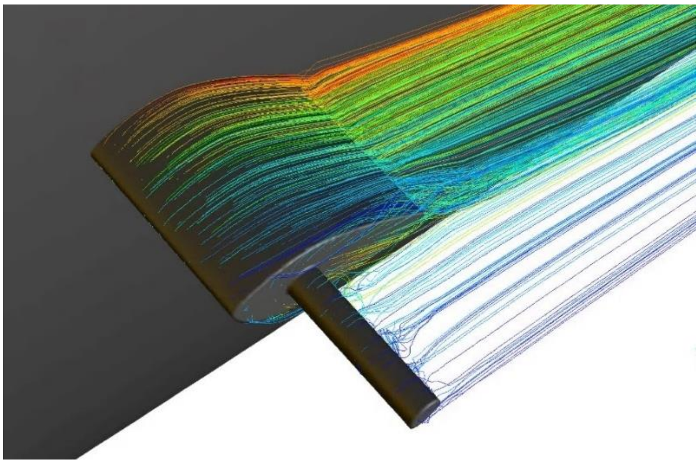

Figure 36: Streamlines ($M_\infty = 0.40$, $\alpha = 3^o$)

Figure 37 shows regions where the surface power level was calculated to be higher than 100 dB. It is noticeable the great impact of the ice probe is producing considerable noise. The shape of the fuselage surface over cockpit the accelerates the flow there and causes a thickening of the boundary layer and consequently an increase in the broadband noise. However, the region affected by the ice detector is much larger. This CFD run leads to two important conclusions:

1. It is important to consider aerodynamics and noise in the design of ice probes to avoid flow separation and high accelerated flow over the probe.
2. There are many probes at the front fuselage of airliners, so the combined noise generated by them is considerable and affects mainly the cockpit crew.

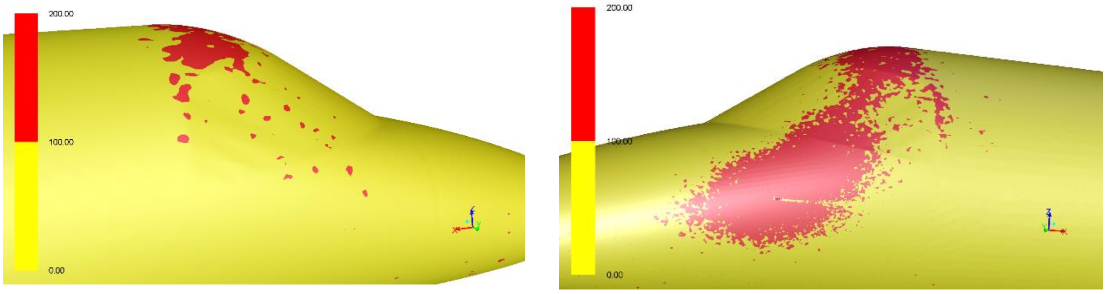

Figure 37: Surface power level above 100 dB reveals that the ice probe is a considerable source of noise

3.4 Some remarks about helicopter noise

In terms of helicopter noise sources, the main sources are the rotor, anti-torque, engines, gearbox, depending on flight condition, transmission gear, and are illustrated in Figure 38. The typical noise sources in helicopters can be summarized as

- Turbulent boundary layer noise.
- Engine noise.
- Heating and ventilation noise.
- Main/tail rotor noise.
- Fan noise.

In a short review of the noise sources generated by the helicopter and connected to the present study, it is worth mentioning the thickness noise which is caused by the blade periodically displacing air during each revolution and is dependent only on the shape and motion of the blade. Generally, the thickness noise propagates in the plane of the rotor as well as the high-speed impulsive noise. In addition, the loading noise is another type of noise source which influences the inside-cabin noise. The noise generated due to the loading on the blade is directed below the rotor and is caused by the acceleration of the force distribution on the air around the rotor blade passing through it. Another important contribution is that of the blade vortex interaction directed down and rearward. It occurs when a rotor blade passes within proximity of the shed tip vortices from a previous blade. The rotor noise sources are depicted in Figure 39.

Figure 38: Helicopter noise sources

Rotating blades emit two distinctly different types of acoustic signatures (33): tone or harmonic noise which is caused by periodic sources with a period linked to a rotation cycle; and broadband noise which is a random, nonperiodic signal caused by the flow-blade interaction.

Helicopter main rotors typically present a rotating frequency between 3 and 7 Hz, depending on the aircraft configuration and performance. The main vibrations caused by the rotors in the structure vary between 3 and 22 Hz, while tail rotors and other accessories rotate at higher frequencies. The most annoying noise for humans is that originated at the tail rotor due to its higher frequency which coincides with the band to which the human ear is most sensitive (34). A method to separate the main rotor noise from that originating from the tail rotor of a helicopter in flight was applied by Farassat and Morris (35). A two-dimensional Fourier analysis method was used, whereas the two-dimensional spectral analysis method is initially applied to artificial signals. This initial analysis provided an idea of the characteristics of the two-dimensional autocorrelations and spectra. Data from a helicopter flight test were then analyzed using data from a 2D-microphone array. Two test aircraft were employed, a Boeing MD902 Explorer NOTAR and a Sikorsky S-76, the latter fitted with a four-bladed tail rotor.

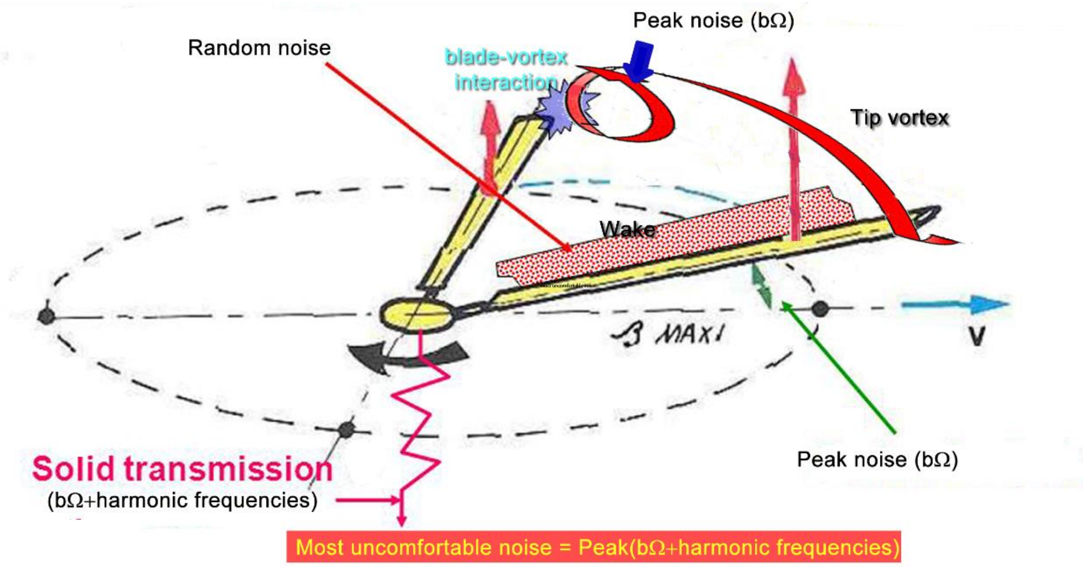

Figure 39: Rotor noise sources [Adapted from Ref. (11)]

The contributions to the internal noise of major helicopter components are summarized in Figure 40. The pressure level is practically linearly decreasing when the frequency is increasing on a logarithmic scale,

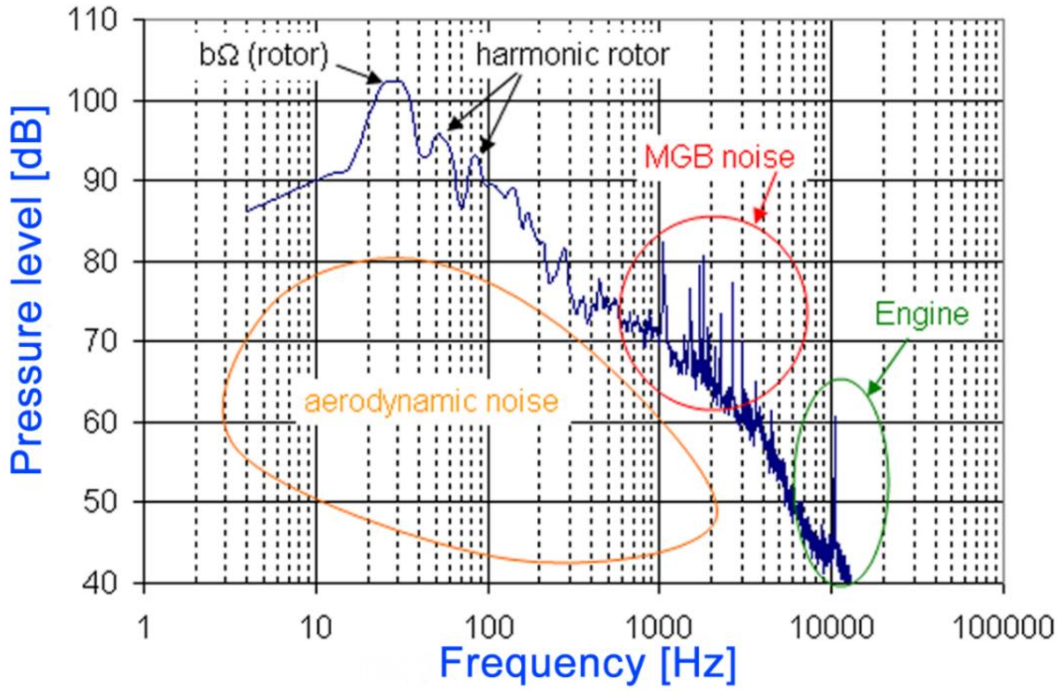

Figure 40: Internal noise mapping (11)

As seen in Figure 39 gearbox is also a major source of noise in helicopter cabins. Several studies address transmission designs by targeting noise reduction (36). The production of gear noise is basically due to the meshing forces acting on the gear teeth. The shape variation of the teeth during their operational cycle will produce sound waves or, in other words, noise (Figure 41). If the forces acting on teeth are reduced, the generated noise will follow this trend. The two main approaches for helicopter transmission are the modification of the tooth shape and contact ratio.

The contact ratio has a strong influence on stiffness. Depending on which part of the toot the contact takes place, the bending stiffness may vary substantially (Figure 42).

Helical gears, as compared to spur gears, typically produce lower noise levels. The helicoidal angle has a strong influence on the overlap ratio (Figure 43):

$$\epsilon_\beta = \frac{btan(\beta)}{p} \tag{23}$$

By raising the parameter ϵ_β, the meshing stiffness decreases, and therefore the noise generated by the gears follows suit.

Li et al. proposed a methodology of fault diagnosis combining vibration and sound signals from gears (37). According to them, the two kinds of signals complement each other, which is beneficial for fault diagnosis. However, there is a limitation of the signal source and sensor in assessing the gear state under different working conditions.

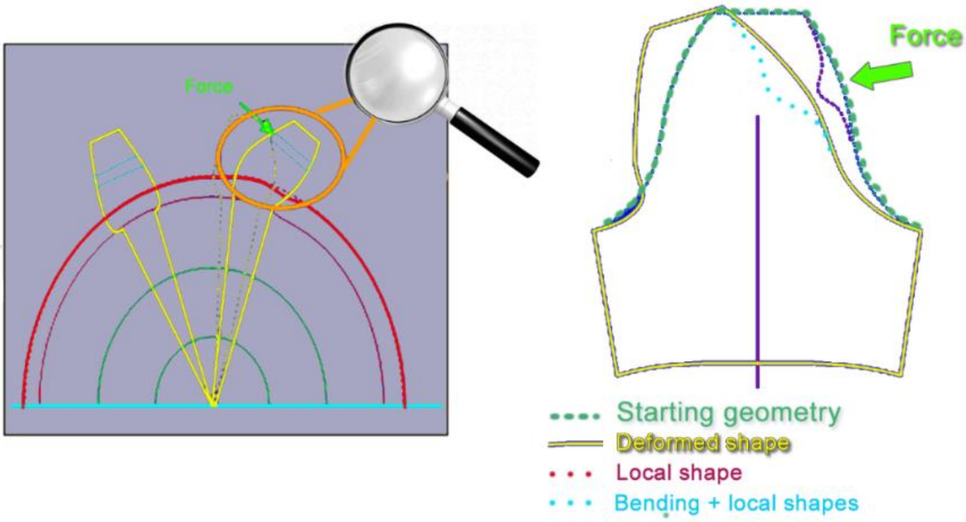

Figure 41: Gear deformation due to loading (11)

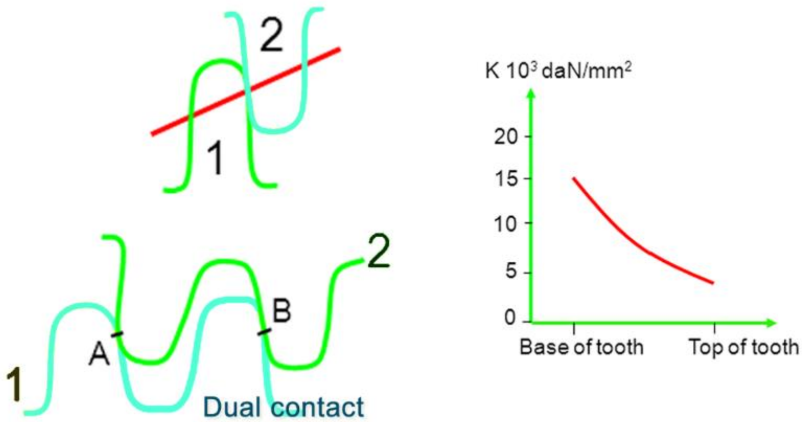

Figure 42: Variation of the bending stiffness according to the contact point (11)

While helical gears provide some degree of noise reduction, their use also generates a thrust load which must be dealt with in the design of the overall system, especially the support bearings, gear blank design, and housing structure (36). Double helical gears cancel the thrust loads from each helix within the gear blank, providing this way relief from the net thrust issue (36).

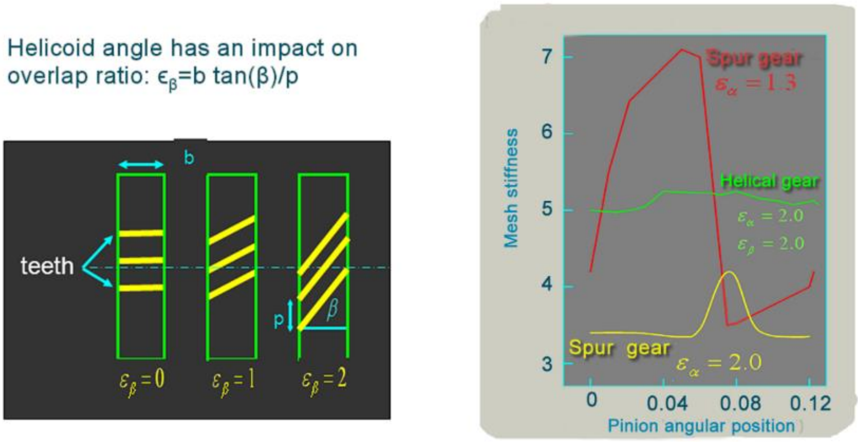

Figure 43: Helical gear (11)

3.5 Turbofan engines

Overview

Interaction of tone and broadband noise mechanisms are found in a multi-blade row propulsor application (Figure 44). Broadband noise is produced by the interaction of airflow with a solid surface, as is the case of a wake from a rotor interacting with a stator. Broadband noise is defined as noise that has a flat spectral density distribution.

Regions of separated flow produce a considerable noise, and the flow separation must be contained as far as possible. These regions can be even found on airplanes in steady-level flight. An example of this is the regions downstream of anti-collision lights, ice detectors, and knobs.

Aeroacoustics measurements are vital for providing validation data for the development of computational aeroacoustics codes (38). The main sources of noise in turbofan engines are as follow:

i. Rotor self-noise which is significant even with clean inflow and no duct boundary layer includes Gutin tones, thickness noise, tones and broadband sound generated by the interaction of the rotor with upstream flow distortion, and tones and broadband sound generated by the interaction of the rotor wakes with downstream bodies and trailing-edge broadband noise.

ii. The interaction of the rotor with the inlet boundary layer is affected by rotor tip clearance.

iii. An unsteady nonuniformity in the tip-duct gap rotating at a fraction of the fan speed, at least when tip clearance and loading are both large.

iv. Stator-generated noise is significantly affected by propagation through the upstream rotor fan which consists of interaction tones and broadband noise with the shed rotor turbulent wakes and stator trailing-edge noise.

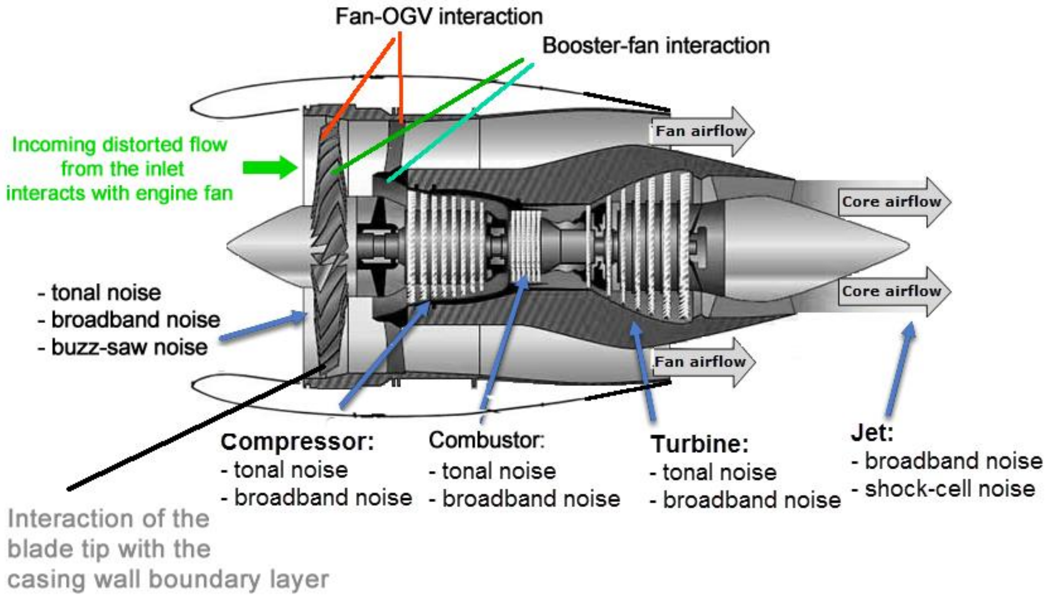

Figure 44: Turbofan engine noise sources (OGV means outlet guide vane)

Example of noise prediction

A computational tool for noise prediction generated by conventional turbofan engines was developed by Muraro in his master's program (39). The tool was based on several methods described in a batch of NASA TM-X reports. Each of those reports addressed some specific component of the engine such as the inlet, fan (40), core (41), turbine, and nozzle (42). The tool was written in MATLAB® language. The following baseline data were considered as an exemplification of noise prediction and a comparison with the results of Refs. (43) (44) is provided. Table 8 shows the ambient and position of the airplane fitted with the engine considered in the present noise estimation example (43).

Table 8: General parameters for noise estimation methods comparison (39)

Parameter	Value	Unit	Description
ΔT_{ISA}	0	ºC	Temperature variation in comparison to ISA
H	0	m	Altitude
P_0	101,325	Pa	Ambient static pressure
ρ_0	1.225	kg/m³	Ambient density
V_0	87	m/s	Ambient velocity or flight velocity
M_0	0.26	-	Ambient Mach number or flight Mach number
θ	50	degree	Directivity angle
ϕ_f	0	degree	Azimuth angle
r	538	m	Distance between the source and the observer

Fan noise

The following parameters (Table 9) are considered for the estimation of the fan noise.

Table 9: Engine parameters for fan noise comparison (39)

Parameter	Value	Unit	Meaning
$\dot{m}_{fan}$	385	kg/s	Fan mass flow rate
PR_{fan}	1.53	-	Fan pressure ratio
η_{fan}	0.9	-	Fan efficiency
D_{fan}	1.6	m	Fan diameter
rpm_{fan}	5,233	rpm	Fan revolutions per minute
$(M_{TR})_D$	1.17	-	M_{TR} value in the fan design point
n_{rotor}	22	-	Number of fan rotor blades
n_{stator}	50	-	Number of fan stator blades
RSS	200	%	Fan rotor/stator spacing

Additionally, there must be informed if the engine has inlet guide vanes and if there are inlet flow distortions. The program results are shown in Figure 45, together with the results from the applet and the ESDU methodology for comparison. The ESDU results are plotted two times, one with the original ESDU method, and another with the Heidmann method (40), the same used in the NASA report. A Java applet for the prediction of noise generated by turbofan engines was some time ago available on the Website of the TU Berlin and it served as a comparison basis. Amado's program results are very similar to the ones obtained by the ESDU results with the NASA method. The difference at higher frequencies can be credited to atmospheric damping, which is not considered in the ESDU method.

However, the applet results are very lower than the programs. This is probably because the applet uses the ESDU own methodology. The difference at higher frequencies is again due to the atmospheric damping.

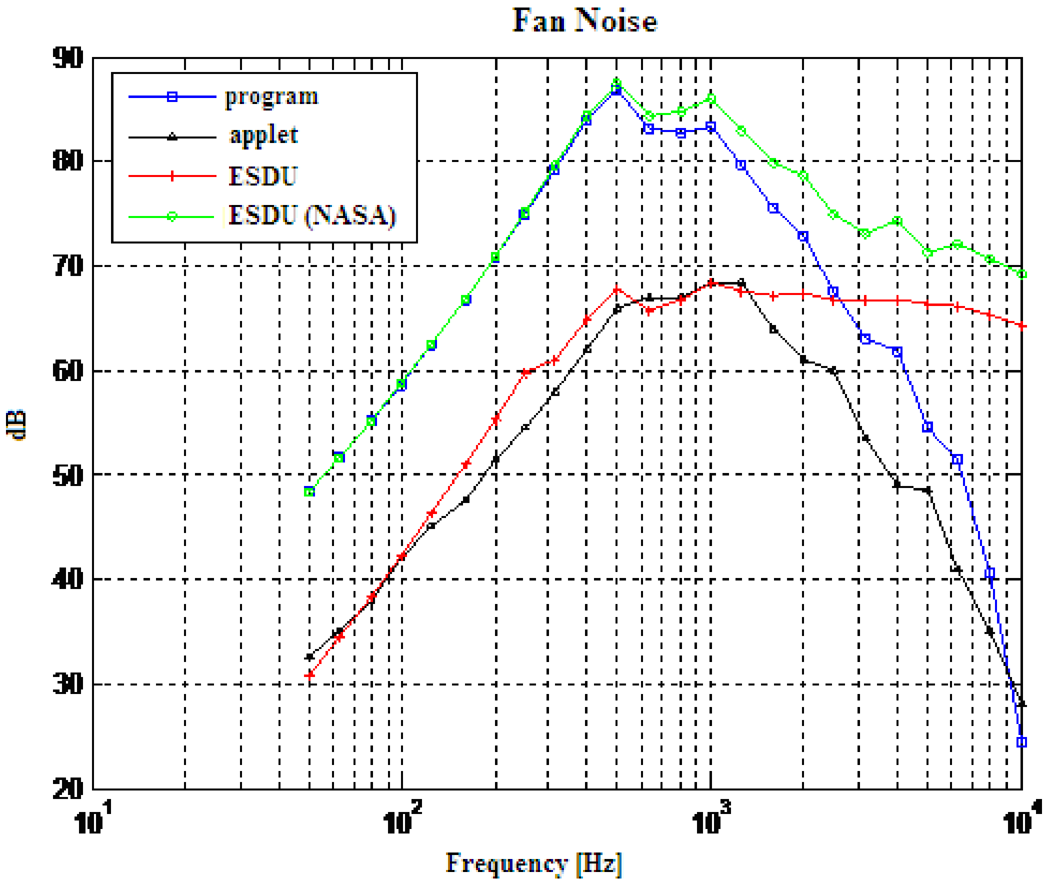

Figure 45: Comparison between the fan noise generated by the program, by the applet, and by the ESDU (39)

Combustion chamber noise

There are 4 parameters needed for the noise prediction generated by the combustion chamber:

Table 10: Engine parameters for combustion chamber noise comparison (39)

Parameter	Value	Unit	Meaning
$\dot{m}_{chamber}$	157	kg/s	Chamber mass flow rate
$T_{entrance}$	844	ºC	Air temperature at the chamber entrance
T_{exit}	1,676	ºC	Air temperature at chamber exit
$P_{entrance}$	3,000,000	Pa	Air pressure at the chamber entrance

The results are shown in Figure 46, together with the results from the applet and the ESDU.

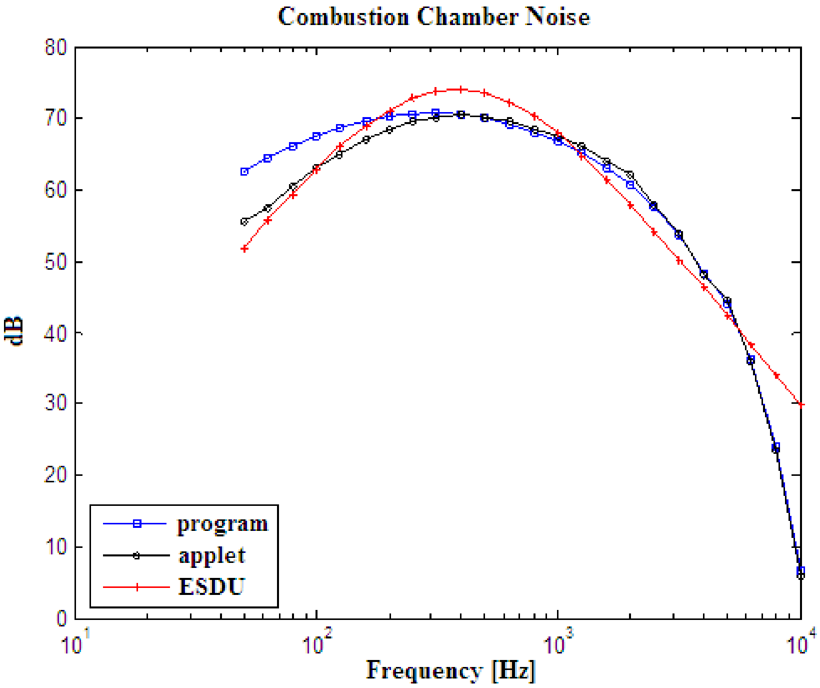

Figure 46: Comparison between the combustion chamber noise results obtained by the program, the applet, and the ESDU (39)

The program results are very close to the applet results, and only show some difference in lower frequencies. The ESDU results are also very similar to the program's, however, since the ESDU method considers a $10.\log_{10}\left(\frac{\rho_0 c_0 W_{ref}}{4\pi.p_{ref}^2}\right)$ factor, that is equal to -10.8 dB at the simulation conditions, the results are lower, and the ESDU plot in Figure 46 has this factor value-added.

Turbine noise

For the turbine noise estimation, the following parameters are required:

Table 11: Engine parameters for turbine noise comparison (39)

Parameter	Value	Unit	Meaning
$\dot{m}_{turbine}$	157	kg/s	Turbine mass flow rate
$rpm_{turbine}$	5,233	rpm	Turbine revolutions per minute
$M_{TR\ turbine}$	0.5	-	Mach number at turbine tip
$n_{rotorturbine}$	50	-	Number of turbine rotor blades
$RSS_{turbine}$	50	%	Turbine rotor/stator spacing

The program results are shown in Figure 47 below, together with the applet results for comparison. As it can be seen, both graphics are very close, showing that the program has a good correspondence.

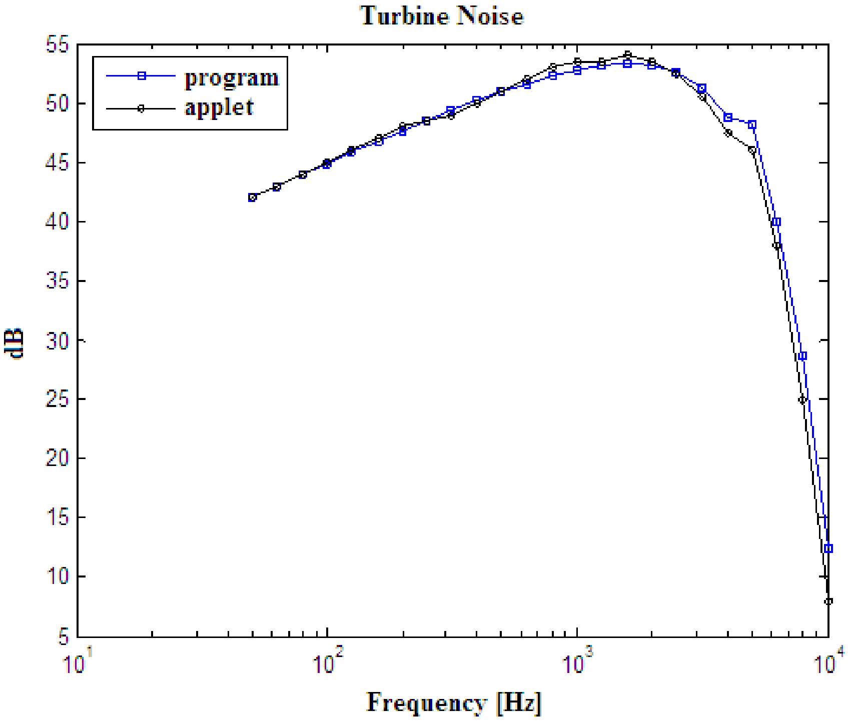

Figure 47: Comparison between the turbine noise results obtained by the program and the applet (39)

Jet noise

Jet noise is caused by a mixture of hot air with the surrounding air. Temperature and velocity gradients can significantly influence the nature of the turbulence, and hence the noise generated. Lighthill (14) proposed the following equation for the power irradiated by the gas exhaustion:

$$P = k\frac{\rho_{jet}}{\rho_{air}}A\frac{V^8}{V_{sound}^5} \tag{24}$$

In Eq. 24, ρ_{jet} e ρ_{air} are the jet and ambient density, respectively; V and V_{sound} are the flow speed and sound speed, respectively; A is the nozzle area, and k is a proportionality constant.

For the estimation of the last part of the engine noise, several velocities, densities, areas, and temperatures are needed (Table 12).

Table 12: Engine parameters for jet noise comparison (39)

Parameter	Value	Unit	Meaning
A_{jet}	0.85	m²	Jet area
h_{gap}	0.15	m	Gap distance
A_{bypass}	2.399	m²	Bypass area
V_{jet}	447	m/s	Jet velocity
V_{bypass}	298	m/s	Bypass velocity
T_{jet}	786	ºC	Jet temperature
T_{bypass}	88	ºC	Bypass temperature
ρ_{jet}	0.22	kg/m³	Jet density
ρ_{bypass}	0.976	kg/m³	Bypass density

Additionally, it is necessary to inform if the nozzle is circular or plug. The results for the applet and the program with a circular nozzle are shown in Figure 48, while Figure 49 shows the results with the plug nozzle. In the two situations, the program has very good results compared to the applet, although with the plug nozzle a small difference can be seen in lower frequencies.

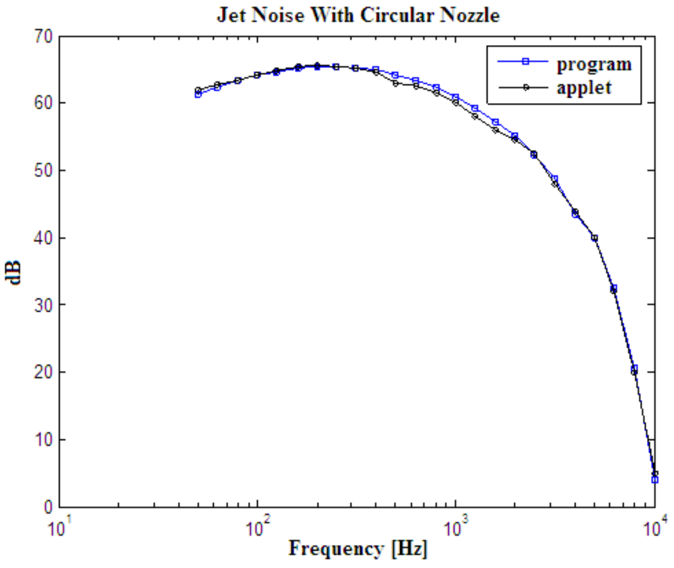

Figure 48: Comparison between the jet noise results with circular nozzles obtained by the program and the applet (39)

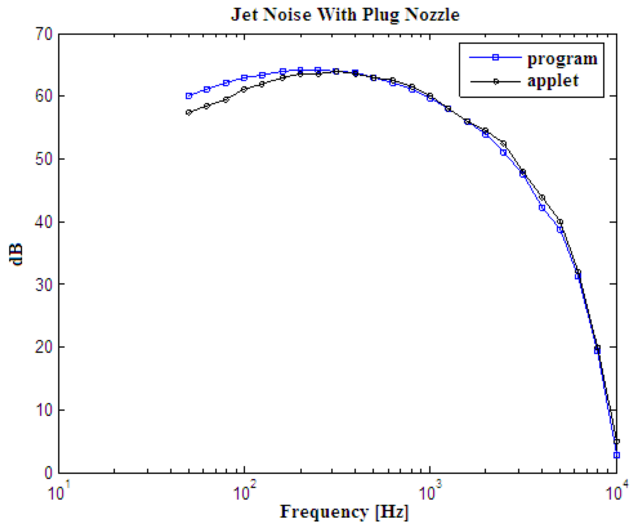

Figure 49: Comparison between the jet noise results with plug nozzles obtained by the program and the applet (39)

By lowering the jet exhaust velocity, the jet noise will be reduced, typically. Some more recent engines like the GE-90 employ this approach by using the engine cycle to extract energy from the engine core and reduce the mixed velocity of the core and fan ducts (38). It is highly desirable to reduce the jet noise without changing the engine cycle, indeed a very challenging problem. In 1996, a jet noise reduction concept using "chevron nozzles" was tested at NASA that reduces the jet noise by mixing the core and bypass flows in a way that reduces low frequency mixing noise from highly turbulent flows (40). This approach is employed in the engines of the B787 airliner.

3.6 Transport airplane optimization with noise constraints

An optimization with noise constraints was carried out for the design of a 78-seat airliner. Some characteristics of this simulation:

- Only twinjet configurations were considered.
- Some FAR rules are set as constraints: missed approach climb gradient, climb gradient in 2nd segment, rate of climb at service ceiling, and others.
- Design variables are set for wing planform and engine definition.
- The turbofan engine model (45) presents five design variables.
- Turbofan noise model according to Ref. (39); airframe noise by Ref. (46).
- The maximum lift coefficient is estimated by the critical section methods.
- Direct Operating Cost (DOC) and Maximum Takeoff Weight (MTOW) are the two objectives.
- Artificial neural networks were employed for the estimation of aerodynamic coefficients (47).
- Range of 2,200 nm with 78 passengers.
- Stabilizers were designed according to controllability and stability criteria (48).
- The genetic algorithm NSGA-II was used as an optimizer.

Figure 50 shows the results of the optimization run. There, 804 airplane configurations were analyzed, of which 279 could properly be sized and did not violate any constraints. Another graph containing the wing aspect ratio and area of the individuals analyzed in the optimization run is shown in Figure 51. Only three airplane configurations composed the Pareto front, which resulted in a line almost parallel to the DOC axis, i. e., the MTOW of the Pareto members differ by a small amount.

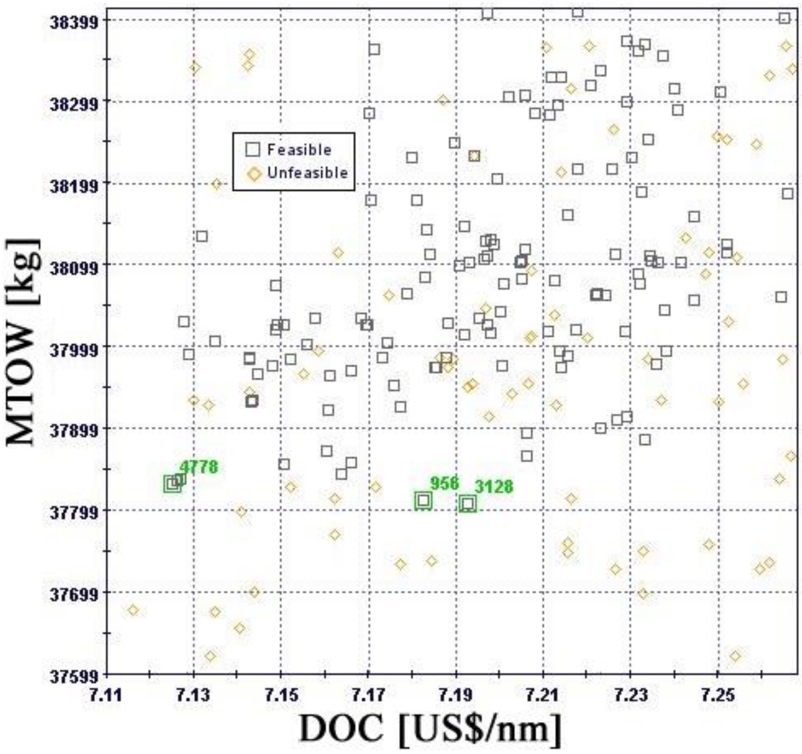

Figure 50: Pareto and dominated individuals of the optimization run for the design of a 78-seat airliner

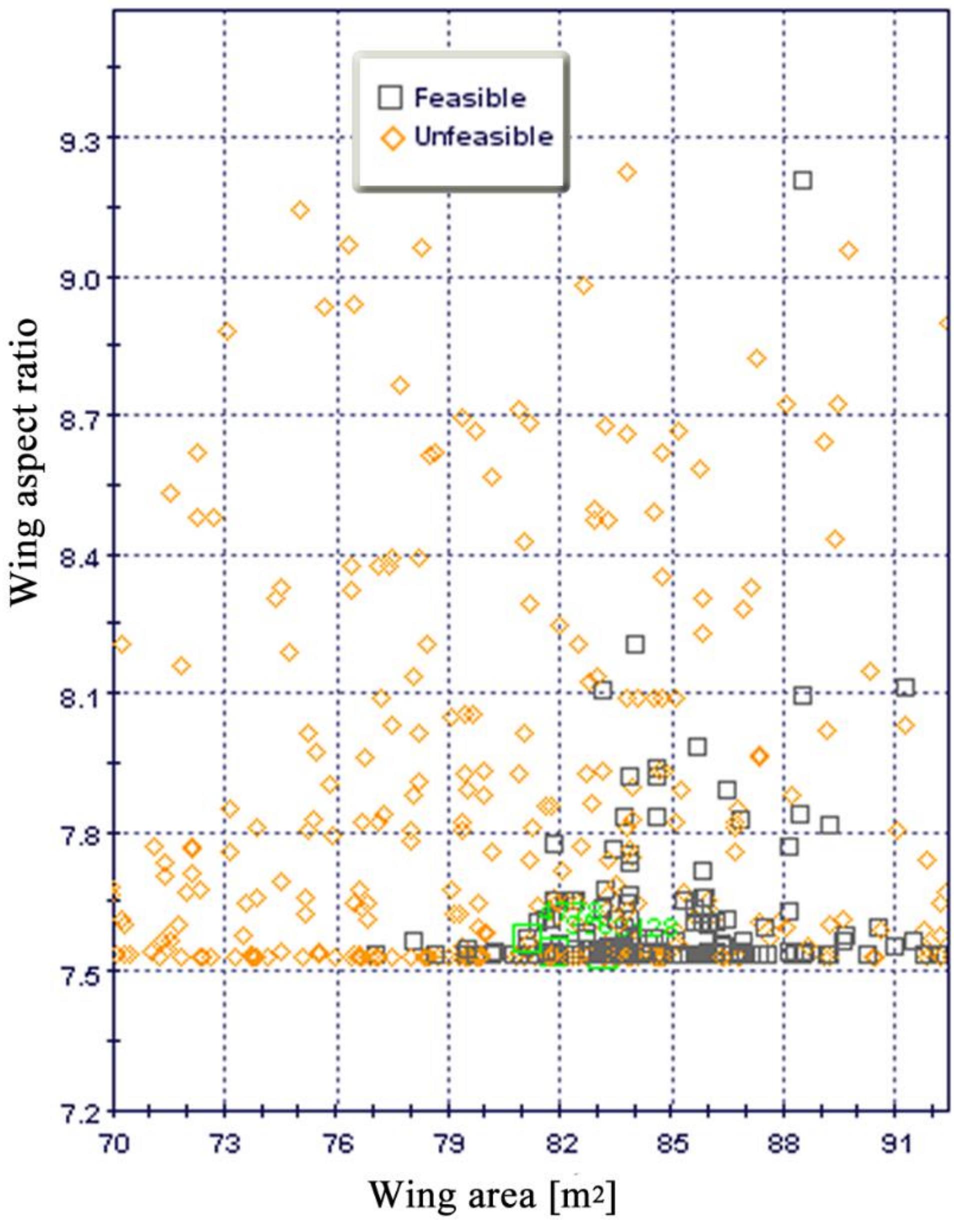

Figure 51: Wing aspect ratio and area of individuals analyzed in the optimization run

Table 13 presents a comparison of characteristics among two E175 versions (AR and LR) to those from three configurations that resulted from the design optimization task. The range for the mission with 78 pax mission was performed at 35,000 ft for the Embraer airplanes and 40,000 and 41,000 ft for the optimized configurations. The thrust provided by the CF34-8E engines of the E175 versions does not enable them to cruise at higher altitudes than 35,000 ft taking off with MTOW, according to the aircraft model employed in the present computations.

The flyover noise (posed as a constraint) was considerably reduced when compared to those from the E175 versions, but the sideline noise (no constraint established) increased approximately by 1 dB.

Table 13: Specifications of the optimally designed 78-seat airliner compared to those of two E175E1 versions. All airplanes present a service ceiling of 41000 ft (49) (50) (51)

	E175 LR	**E175 AR**	**ID 956**	**ID 4778**	**ID 3128**
Range (MTOW, LRC, 78 Pax, ISA, 100 nm alternate, 45 min loiter) [nm]	2,000[+, 1]	2,200[+, 2]	2,200[†]	2,200[†]	2,200[†]
Maximum operating Mach number	0.82	0.82	0.84	0.84	0.84
Takeoff field length (MTOW, sea level, ISA) [m]	1,724	2,244	2,000	2,000	2,000
Landing field length (MLW, sea level, ISA) [m]	1,259	1,261	1,259	1,259	1,259
BOW [kg]	21,870	21,890	**21,708**	21,830	21,785
MTOW [kg]	38,790	40,370	37,812	37,832	**37,808**
Max. usable fuel [kg]	9,428	9,428	9,187	9,007	9,421
Wing quarter-chord sweepback angle	23.5	23.5	26.63	27.48	27.25
Wing reference area [m^2]	72.72	72.72	82.07	**81.37**	78.53
Wing aspect ratio	8.6	8.6	7.50	7.54	7.50
Fuselage width [m]	3.01	3.01	2.84	2.84	2.84
Engine by-pass ratio	5.00	5.00	5.69	5.27	5.54
Engine overall pressure ratio	28.50	28.50	30.57	31.85	29.37
Fan pressure ratio	1.9	1.9	1.60	1.64	1.65
Static takeoff thrust (Sea level, ISA) [lb]	14,200	14,200	14,902	15,017	14,706
Time to climb to initial or final cruise altitude [min]	18[1]	18[2]	26.3[3]	25.7[4]	24.8[3]
Flyover noise (EPNL)	84.4[*]	85.9[*]	78.8	79.0	**78.6**
Sideline noise (EPNL)	91.9[*]	91.9[*]	**93.0**	93.1	**93.0**
DOC [US$/nm]	-	-	7.183[β]	7.126[β]	7.194[β]
[1,2]FL350 [3]FL400 [4]FL410 / [+] TOW of 38,790 kg / [†] MTOW, 200 nm alternate + 45 min loiter * Reference (50) / β fuel at US$ 2.387/gallon					

4. Estimation and prediction with convolutional neural networks

4.1 Overview

There are various types of neural networks, which are used for diverse applications and data types. For example, recurrent neural networks are frequently utilized for natural language processing and speech recognition whereas multilayer perceptron networks are frequently utilized for parameter identification (47).

Multilayer-perceptron and other ANNs operating on raw images do not scale well as the image size increases, lacking accuracy (52). For example, consider a color image with 64×64 pixels with a red, green, and blue channel. This results in a total of 64×64×3 inputs to that network, which apparently can be handled. However, if 256×256-pixel images are in place, the total number of inputs and weights would jump to 196,608. For an ANN with multiple hidden layers with a varying number of nodes per layer, these parameters can demand unacceptable training times and unsatisfactory accuracy (52).

Convolutional neural networks (ConvNets or CNNs) are more often utilized for classification and computer vision tasks (53). CNN represents the local features by convolution kernels to solve the problem of high-dimension data.

Manual feature extraction methods to identify items in images demands considerable computational power. By using CNNs a more scalable approach to image classification and object recognition tasks is possible. The CNN methodology is based on utilization of concepts and ideas from linear algebra, specifically matrix multiplication (convolution operation), to identify patterns. Besides finding patterns in images to recognize objects, faces, and scenes, CNNs can also be quite effective for classifying signal data such as audio records, HUMS measuraments, and other time series. One important application of CNN is on autonomous vehicles, which require intensive processing for object recognition.

CNNs embody multilayer perceptrons neural networks ins their structure (47). Multilayer perceptrons usually are fully connected networks, that is, neurons placed in one layer are connected to all other neurons in both the preceding and the following layer. CNNs have three main types of layers (54):

- Convolutional layer
- Pooling layer
- The fully connected layer

The convolutional layer is the first layer of a convolutional network. Convolutional layers can be followed by additional convolutional layers, but a fully connected layer must be the last one. With each layer, the CNN increases in its complexity, identifying greater portions of the image. Earlier layers focus on simple features, such as colors and edges. As the image data progresses through the layers of the CNN, it starts to recognize larger elements or shapes of the object until it finally identifies the intended object.

Convolutional layer characteristics

The convolutional layer is the main part of a CNN. It requires a few components, which are input data, a filter, and a feature map. However, the convolutional layers are where high-demanding computational processing takes place.

Convolution is a mathematical operation on two functions (*f* and g) that produces a third function (*f***g*) that expresses how the shape of one is modified by the other. In practice, the convolution theorem is used to design filters in the frequency domain. The convolution theorem states that the convolution in the time domain equals the multiplication in the frequency domain.

To illustrate the application of a convolutional operation, consider an image sharpening. Taking four times the current pixel and subtracting the neighbors from it results in a sharpened image (Figure 52).

Another example considers a color image where the input consists of a matrix of 3D pixels. This means that the input will have three dimensions, height, width, and depth, which correspond to RGB layers in an image.

The feature capture of a CNN consists of a two-dimensional array where weights are stored. This represents only a portion of the image. The filter size (width and height) can be specified that also determines the size of the receptive field. In Figure 53, a 3x3 matrix was employed. The filter is then applied to an area of the image, and a convolutional operation is then carried out between the input pixels and the filter. This operation, a dot product, is then stored in an output array. This process is repeated until the entire image is processed. The final output from the series of dot products from the input and the filter is known as a feature map or kernel matrix (54).

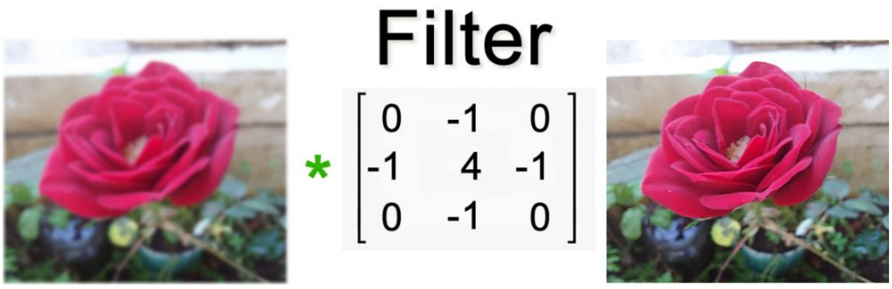

Figure 52: Example of image sharpening

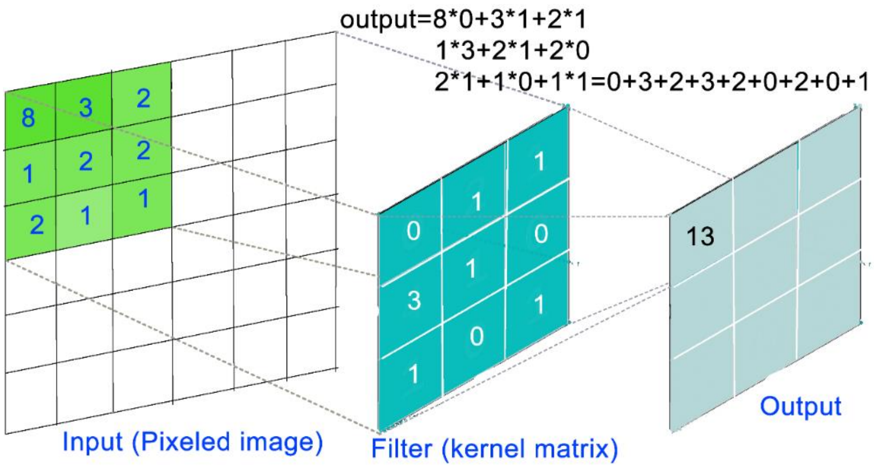

Figure 53: Feature mapping of the color image example [Adapted from (54)]

As can be seen in the image in Figure 53, each output value in the feature map does not have to connect to each pixel value in the input image but it only needs to connect to the receptive field, the area of filter application. Since the output array does not need to map directly to each input value, convolutional (and pooling) layers are commonly referred to as *partially connected* layers.

The weights in the feature detector remain fixed as it moves along the image, which is also known as parameter sharing. Parameters, like the weight values, are modified during the training of the network, which can be performed by backpropagation and optimization algorithms such as gradient descent ones.

Three parameters affect the size of the output, and they must be set before training of a neural network starts (54) (55):

- The *number and size of filters* affect the profundity of the output, so the number of feature maps is directly related to this parameter.
- *Zero-padding* is usually used when the filters do not fit the input image. This sets all elements that fall outside of the input matrix to zero, producing a larger or equally sized output. It must be specified whether to use padding.
- *Stride* is the distance or pixels that the kernel moves over the input matrix. While stride values of two or greater is rare, a larger stride yields a smaller output.
- *Output depth:* This parameter controls the number of neurons in a convolutional layer, which is connected to the same region in the input layer (55).

After each convolution operation, a CNN applies a Rectified Linear Unit (*ReLU*) transformation to the feature or constituent map, conferring non-linear characteristics to the model. The *ReLU* activation operation performs a nonlinear threshold operation, where any input value less than zero is set to zero. This operation is equivalent to

$$f(x) = \begin{cases} x, x > 0 \\ 0, x \leq 0 \end{cases} \tag{25}$$

ReLU allows for faster and more effective training by mapping negative values to zero and keeping positive values active and only the activated features are carried forward into the next layer (56).

As described in the preceding paragraphs, another convolution layer can follow the initial convolution layer. When this happens, the structure of the CNN can become hierarchical as the later layers can see the pixels within the receptive fields of prior layers. As an example, it is required to determine whether an image contains a car or not (Figure 54). The usual approach is to consider the car as a sum of parts. It is comprised of an engine, transmission, wheels, doors, instrumentation et cetera. Each part of the car makes up a lower-level pattern in the neural net, and the combination of its parts represents a higher-level pattern.

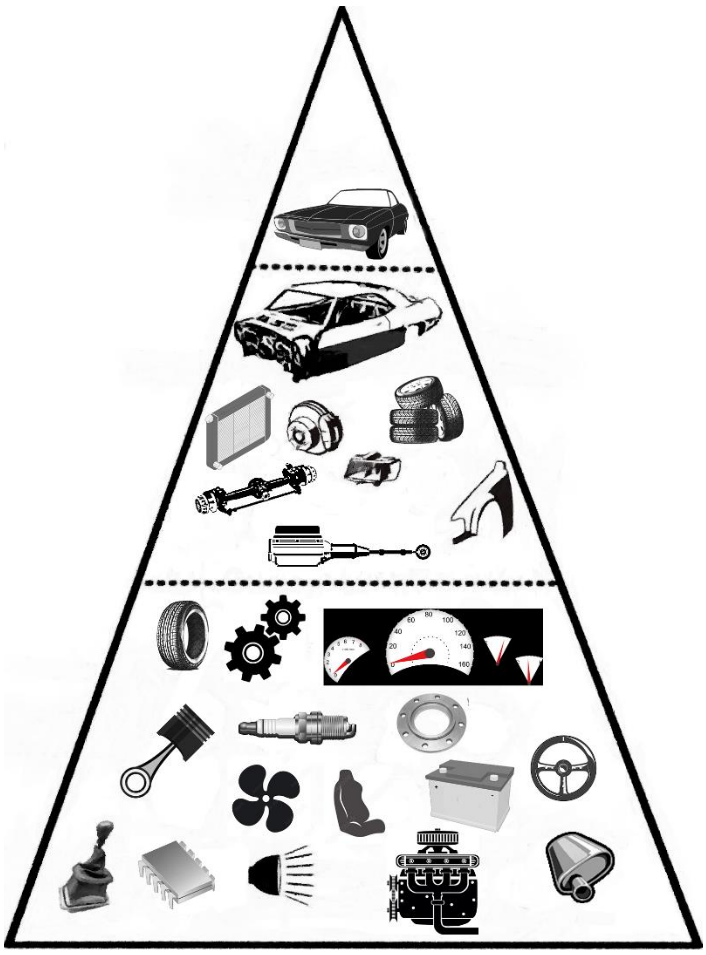

Figure 54: Hierarchy within the CNN [Adapted from (54)]

Ultimately, the convolutional layer converts the image into numerical values, allowing the neural network to interpret and extract relevant patterns.

Pooling Layer

Pooling layers reduce the dimensionality of the problem, lowering the number of parameters present in the input data. Like the convolutional layer, the pooling operation applies a filter across the whole input, but here the filter does not have any weights. Instead, the kernel applies an aggregation function to the values within the receptive field, populating the output array. While a lot of information is lost in the pooling layer, it also has several benefits for CNN. They help to reduce complexity, improve efficiency, and limit the risk of overfitting. There are two common types of pooling in popular use: max and average.

Fully connected layer

Pixel data of the input image are not directly connected to the output layer in partially connected layers. However, in the fully connected layer, each node in the output layer connects directly to a node in the previous layer.

This layer performs the task of classification based on the features extracted through the previous layers and their different filters. While convolutional and pooling layers tend to use *ReLu* functions, FC layers usually leverage a *softmax* activation function to classify inputs appropriately, producing a probability from 0 to 1.

Convolutional neural networks applications

Convolutional neural networks power image recognition and computer vision tasks. Computer vision is a field of artificial intelligence (AI) that enables computers and systems to derive meaningful information from digital images, videos, and other visual inputs, and based on those inputs, it can act. This ability to provide recommendations distinguishes it from image recognition tasks. Some common applications of this computer vision today can be seen in:

- *Marketing*: photo tagging in social media.
- *Maintenance*: gear fault diagnosis. Monitoring and diagnosis are important means to detect and eliminate mechanical faults in real-time or to proceed with preventive maintenance (37).
- *Healthcare*: thanks to machine learning in radiology diseases can be now easily diagnosticated.
- *E-commerce*: Visual search has been incorporated into some e-commerce platforms with the introduction of methodic purchases and data-driven personalized advertising.
- *Automotive*: While the age of driverless cars has not quite emerged, the underlying technology has started to make its way into automobiles, improving driver and passenger safety through features like lane line detection.

4.2 Examples of CNN application for the prediction and forecasting of time-series

CNN-RNN combination

Time series forecasting is an important area of machine learning and in recent years has been the main topic of research in a wide range of sectors such as engineering, energy, finance, and health among others.

This example presents a combination of a CNN with a recurrent neural network (RNN) to predict a function dependent on time-based known values for previous months. The application was developed by H. Sanchez (57).

The CNN is tailored for feature extractions while an RNN has proved its ability to predict values in sequence-to-sequence series. At each time step, the CNN extracts the main features of the sequence while the RNN learns to predict the next value on the next time step (57).

The size of the input of the sequence is lagged by n-months thus the RNN expects an input size of n-months cases to yield the prediction of the next month; one step ahead.

This example used a sine-type distribution with decreasing amplitude over time. The training and the net parameters need further tuning. Fine-tuning is performed by using Bayesian optimization. The observed data was split into training and testing. 90% of the data is used for training and 10% for testing. It is useful to reserve a small portion of the data for validation purposes thus the convergence progress can be closely checked. In this example, the validation data has been ignored.

To improve the convergence process, it is recommended to standardize the data or normalize the data. In this example the data is standardized. The data can be normalized by several normalization algorithms by using *normalize* the function of MATLAB® but the normalization parameters need to be recorded to further de-normalize or convert the data to its generic values.

Monitoring the convergence training process is always useful (Figure 55). By plotting various metrics during training, the user can learn how the training is progressing. For example, it is possible to determine if and how quickly the network accuracy is improving, and whether the network is starting to overfit the training data.

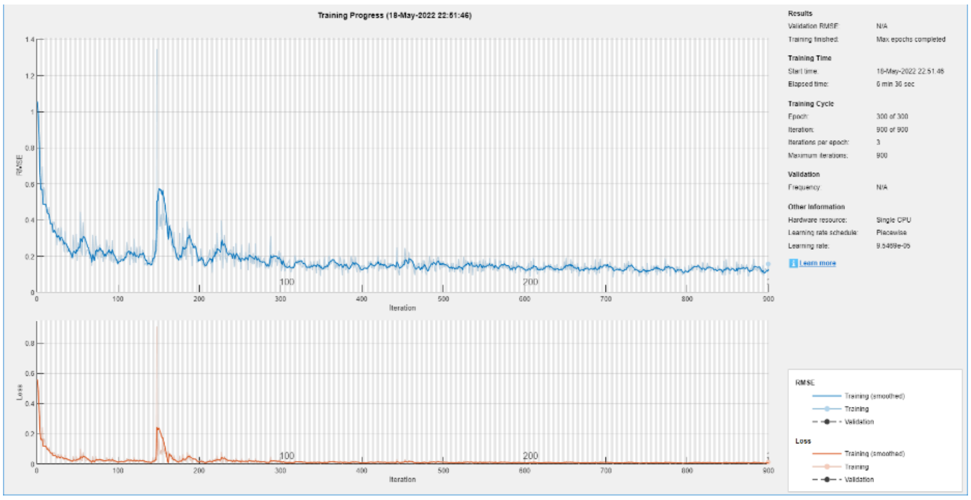

Figure 55: Convergence log of the hybrid ANN for the prediction of time-series

The time series and forecasted with the trained network values are compared in Figure 56 and Figure 57. The simple correlation (Eq. 26) between the testing and the predicted value is also shown in Figure 56.

$$sMAPE = \frac{1}{2}\frac{mean(Y_{predicted} - Y_{test})}{abs(Y_{predicted}) - abs(Y_{test})} \tag{26}$$

Figure 58 shows the correlation between predicted and observed data and contains. For an ideal prediction capability, the regression curve of the predicted sample should merge with the target line crossing the origin.

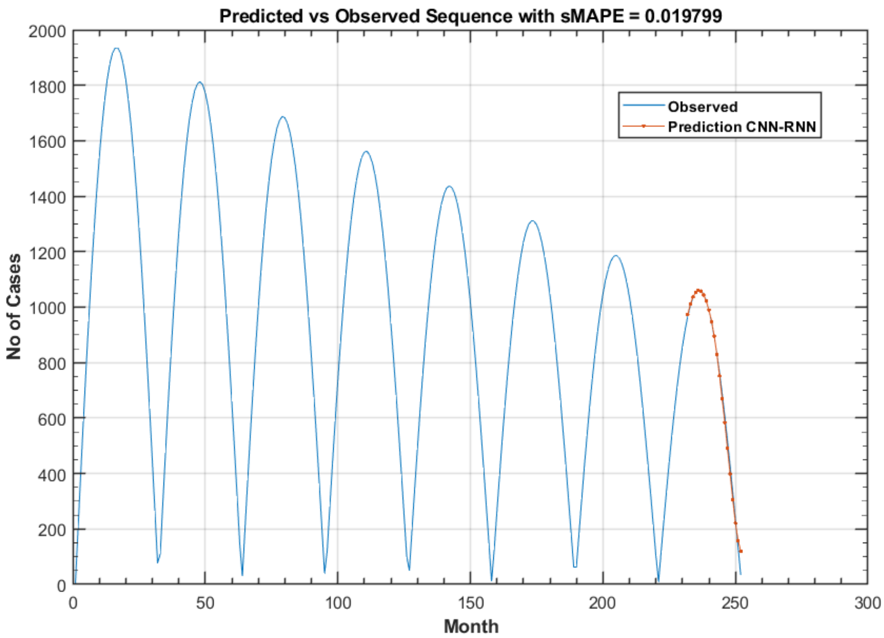

Figure 56: Distribution selected for analysis and its part that was selected for forecasting

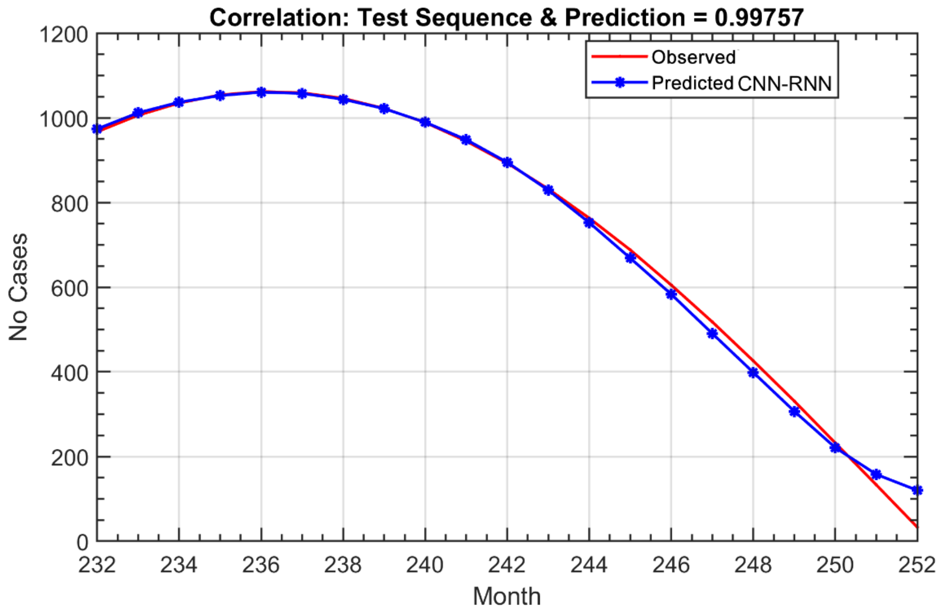

Figure 57: Predicted vs observed sequence for sinusoid-type time series

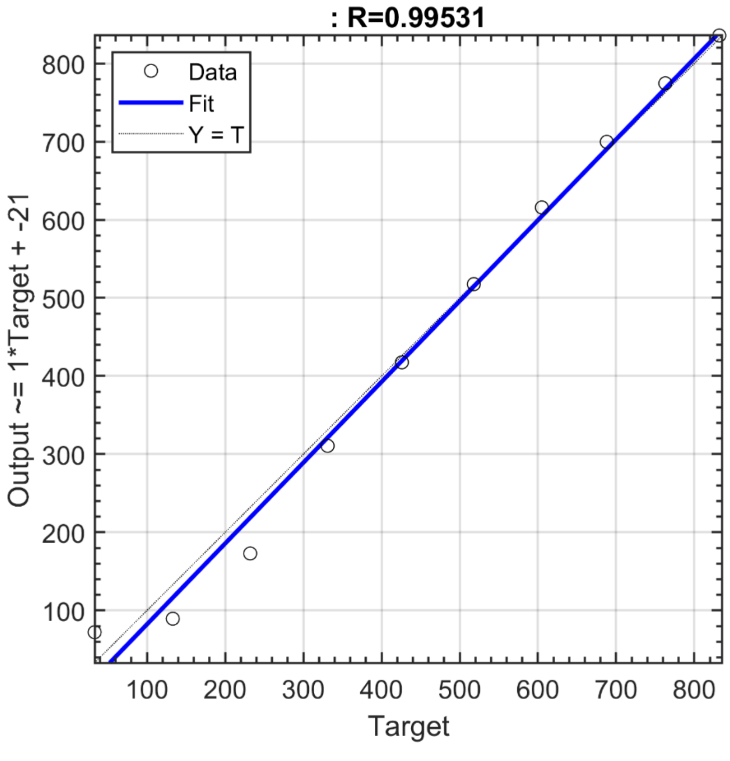

Figure 58: Correlation between predicted and observed data

Historic data concerning the West Texas Intermediate (WTI) price for crude oil is freely available by U.S. Energy Information Administration (58). The WTI Price evolution from January 1986 until April 2022 is shown in Figure 59. Utilizing the same methodology utilized in the previous example, which consists of five convolutional layers and a single fully connected one, the prediction capacity for the last batch of data is shown in Figure 59 and Figure 60. In this case, the hybrid CNN is working as a surrogate model for the crude oil price over time.

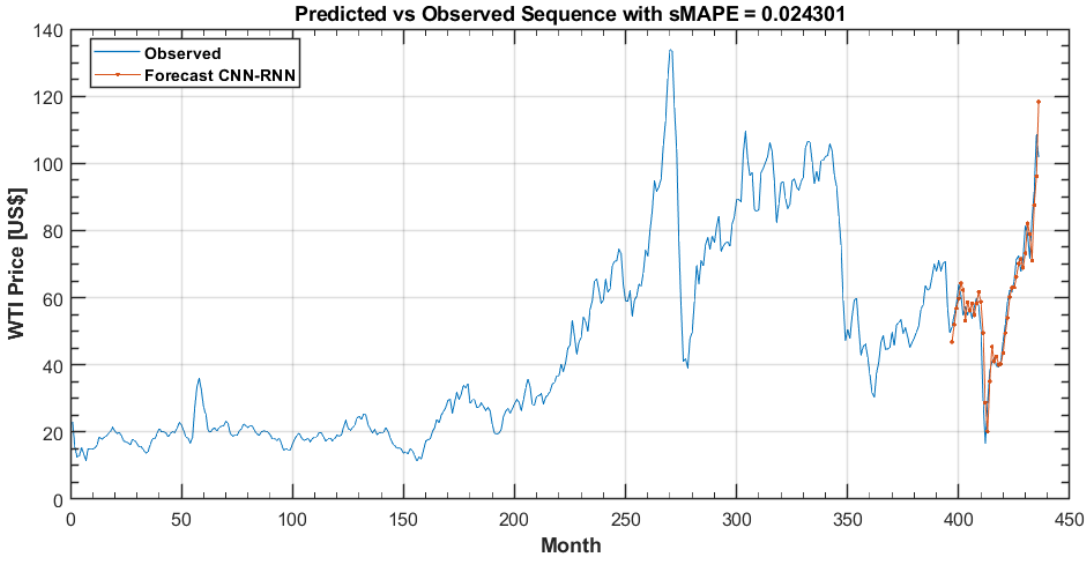

Figure 59: oil data series and prediction capability of the CNN-RNN combination

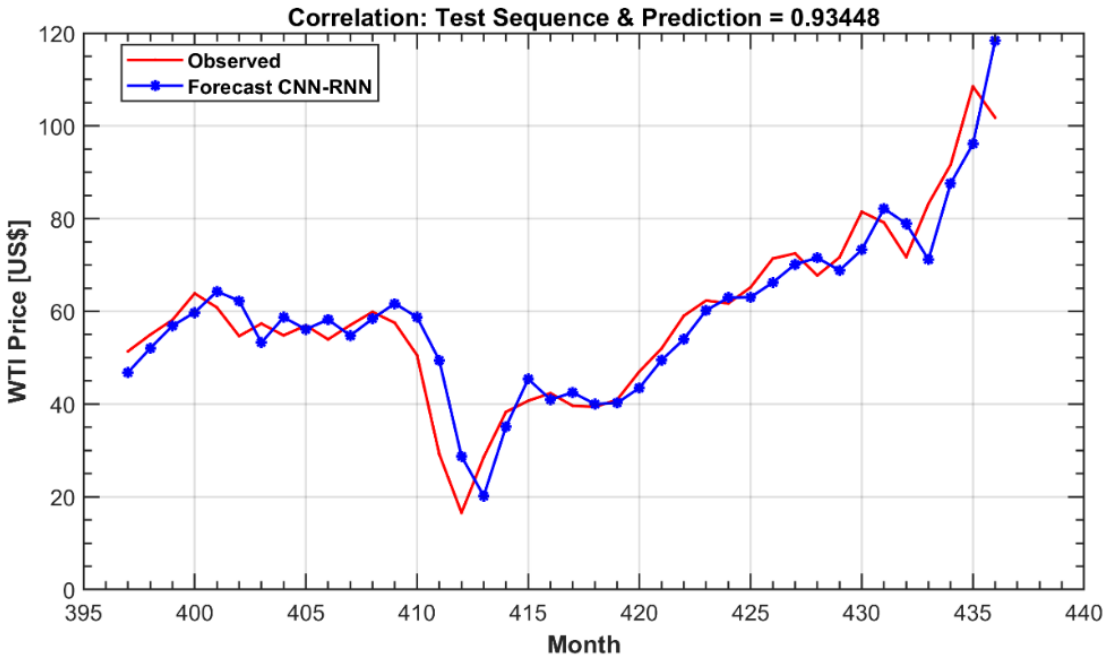

Figure 60: Close-up of the observed and predicted WTI price by the CNN-RNN combination

Non-stationary time series

Despite the good results with the two data sets shown before, these sets contain nonstationary data. Thus, the hybrid RNN does not work very well to proceed with forecasting. However, for other data sets such as stock data, it is recommended to transform the data stationary and then apply the method described before.

The Auto-Regressive Integrated Moving-Average (ARIMA) model was developed by Box-Jenkins (59). This model has been successfully applied in several situations, with emphasis on the forecast of econometric time series.

The ARIMA model establishes the prediction of the future value of a variable with the use of a temporal correlation structure (autocorrelation). This model consists of estimating a variable from a linear function, through several historical observations, considering its random errors.

The difference between exponential smoothing models and ARIMA is that the former is based on describing the trend and seasonality in the series, while the latter is based on autocorrelations present in the data.

The structure of time series data presents a big challenge for researchers and users, considering that traditional regression approaches do not yield valid results. Uncorrelated residuals are a key assumption of many regression methods. Models that fail to account for autocorrelation will have correct parameter estimates, but incorrect standard errors.

The identification steps involve fitting the autoregressive component (variable “p”), the moving average component of the ARIMA model (variable “q”), as well as any required differing to make the time series stationary or to remove seasonal effects (variable “d”). Together, these user-specified parameters are called the order of ARIMA.

The formal specification of the model will be ARIMA (p,D,q), where

- p — Nonseasonal autoregressive polynomial degree nonnegative integer
- D — Degree of nonseasonal integration nonnegative integer
- q — Nonseasonal moving average polynomial degree nonnegative integer

The first step in model identification is to ensure the process is stationary. Stationarity can be checked with a Dickey-Fuller Test. In statistics, the Dickey-Fuller test tests the null hypothesis that a unit root is present in an autoregressive time series model. The alternative hypothesis is different depending on which version of the test is used but is usually stationarity or trend-stationarity (60). Any non-significant value under model assumptions suggests a non-stationarity. The process must be converted to a stationary process to proceed by differencing the time series using a lag in the variable and removing seasonality effects.

After a developed model is properly considered to be stationary and adjusted such that there is no information in the residuals, a forecasting task can then take place. Forecasting assesses the performance of the model against concrete data. The usual approach now is to split the time series into two parts, utilizing the first part to fit the model and the second half to check performance. Usually, the utility of a specific model or the utility of several classes of models to fit actual data can be assessed by minimizing a value like a root mean square.

To proceed with the forecast of WTI oil price using the data from Figure 59 the regARIMA MATLAB® command was initially employed (61). This creates a stationary regression model of the oil-price time series. If the errors have an autocorrelation structure, then it is possible to specify models for them.

A seasonality parameter is required by the regARIMA command, and it exerts a great influence on the results. After the model is created, another step involves its rework by using the ARIMA errors of the previous step. This rework also encompasses the use of the distribution of the innovations to build the likelihood function. Finally, forecast responses of the regression model with ARIMA errors are performed.

Figure 31 shows a forecast with ARIMA data regularization that is compared to the last 200 registers of the WTI oil price. This period, i. e., this part of the data set was never employed in the creation of the regression models. This result represents the best match obtained by adjusting the seasonality parameter. in Figure 32, the area of interest was augmented. The overall trend of the price evolution was satisfactorily captured, but the plunge seen in Figure 32, was in some way anticipated.

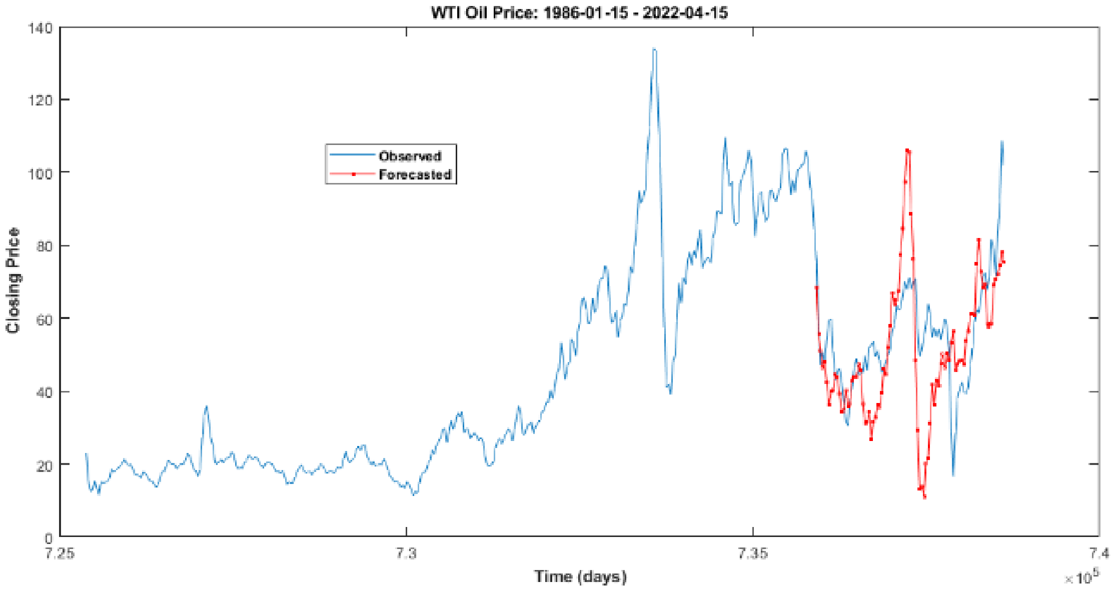

Figure 61: Oil price forecast

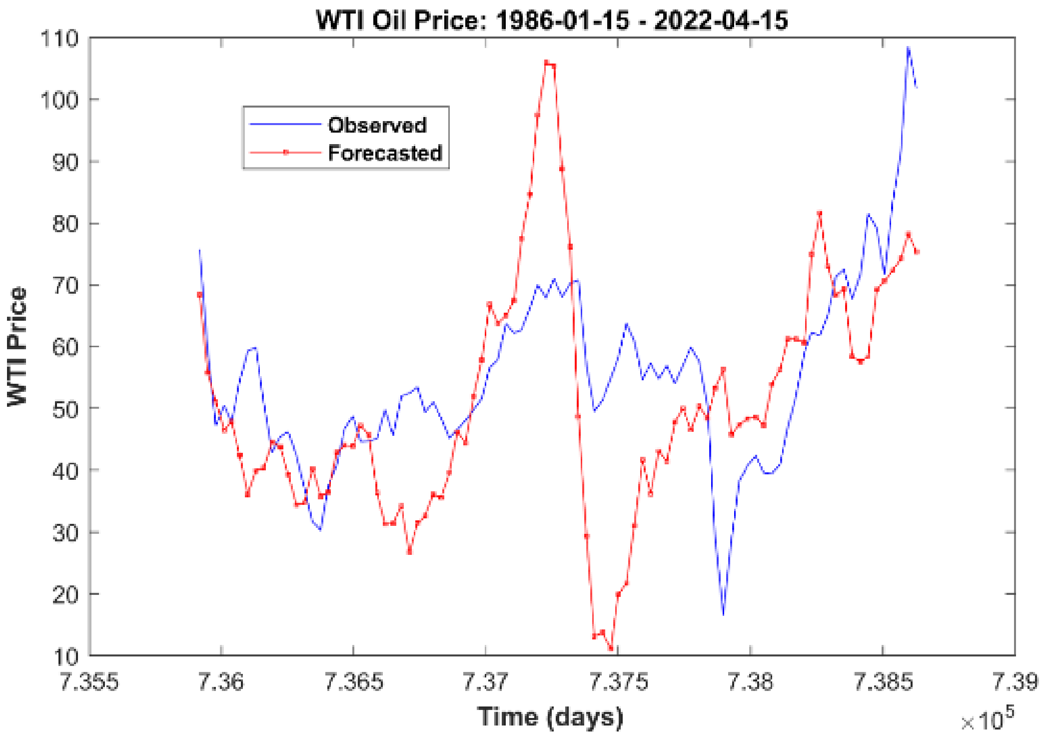

Figure 62: Oil price forecast in detail

4.3 Remained useful life of a turbofan engine

The remaining useful component life (RUL) is given in units of time (e.g., hours or cycles); end-of-life can be subjectively determined as a function of operational thresholds that can be measured. These thresholds depend on user specifications to determine safe operational limits.

Prognostics is currently at the core of systems health management. Reliably estimating remaining life holds the promise of considerable cost savings (for example by preventing unscheduled maintenance and by increasing equipment usage) and operational safety improvements. Remaining life estimates provide decision-makers with information that allows them to improve operational characteristics (like usage) which in turn may prolong the life of the component. It additionally allows companies to account for upcoming maintenance and set in motion a logistics process that supports a seamless transition from defective equipment to a fully operative one. Aircraft engines and structures, helicopter gearboxes, power plants, etc. are some of the typical examples of these types of equipment.

There is a lack of run-to-failure data sets for prognostics based on data. In most cases, real-world data contain fault signatures but no or little data capture fault evolution until failure (62). However, progress has been recorded. Khan and Yairi (63) studied the utilization of deep learning tools, such as, convolutional neural networks (CNNs), and recurrent neural networks (RNNs) in prognosis and health management.

Saxena et. al (62) describe how damage propagation can be modeled within the modules of aircraft gas turbine engines. They built response surfaces for all sensors by using a thermodynamical model for the engine as a function of variations of flow and efficiency of its components. An exponential rate of change for flow and efficiency loss was imposed for each data set, starting at a randomly chosen initial deterioration set point. The rate of change of the flow and efficiency denotes an otherwise unspecified fault with an increasingly worsening effect. The rates of alteration of the faults were constrained to an upper threshold but were otherwise chosen randomly. Damage propagation was allowed to continue until a failure criterion was reached. A health index was defined as the minimum of several superimposed operational margins at any given time instant. The failure criterion is reached when the health index equals zero. The output of the model obtains the cycles of the measurements, typically available from aircraft jet engines.

The prominent advantage of a deep learning approach is that there is no practical necessity for manual feature extraction or selection to use in a customized model to predict RUL. In addition, no prior knowledge is required of equipment health prognostics or signal processing to adequately develop a deep learning-based RUL prediction model.

The remained part of this section shows how to predict the RUL of turbofan engines by using deep convolutional neural networks, based on an example made available by Mathworks, Inc (64) (65). This example utilizes the Turbofan Engine Degradation Simulation Data Set (C-MAPSS) (66). The data set was compressed into a single file that can be freely downloaded from the NASA Website. It contains run-to-failure time-series data regarding four different sets (FD001, FD002, FD003, and FD004), corresponding to tests carried out under different combinations of operational conditions and fault modes. The present application uses only the FD002 data set, which is further divided into training and test groups. The training group contains simulated time-series data for 260 engines.

Each engine contains 21 sensors whose values are recorded at a given instance in a continuous process. Therefore, the sequence of recorded data varies in length and corresponds to a full run-to-failure instance. The test group contains 259 partial series and corresponding values of the remaining useful life at the end of each sequence.

The available data from NASA files present 26 columns of numbers, separated by spaces. Each row is a data record taken during a single operational cycle, and each column represents a different variable:

- Column 1 — Unit number
- Column 2 — Elapsed time
- Columns 3–5 — Operational conditions
- Columns 6–26 — Measurements of 21 sensors

Figure 63 shows some information extracted from the FD002 data set, which contains a failure related to a degradation of the high-pressure compressor. Initially, a verification procedure concerning the variability of some data is carried out and if there are small changes over time this data is discarded (64). Here, it is properly processed and sorted the data in a sequence format, with the first dimension being representative of the number of selected features and the second dimension representing the length of the time sequence. A convolutional layer composes a set with a normalization layer followed by an activation one, this combination being tailored for feature extraction. The fully connected layers and regression layer are used at the last stage of the network to estimate the RUL value and provide the output figure.

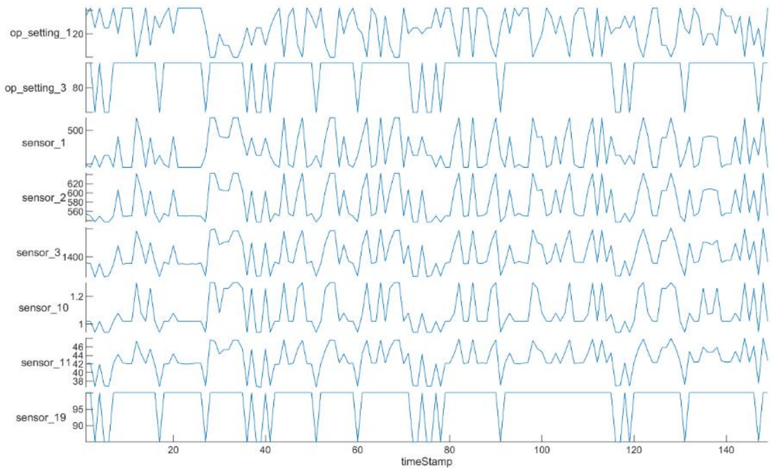

Figure 63: Some data of NASA's Turbofan Engine Degradation Simulation Data Set

The chosen CNN architecture applies a 1-D convolution along the time sequence direction only. Therefore, the order of features has no impact on the training, and only trends for each feature at a time are considered (64).

The CNN consists of five consecutive sets of a convolution 1-d, batch normalization, and a *ReLU* layer, with increasing filter size and number of filters as the first two input arguments to the convolution layer followed by two fully connected layers with 100 neurons each and a dropout layer with a dropout probability of 0.5. Since the network predicts the RUL of the turbofan engine, there is just a single output in the fully connected layer as the last layer of the network. Figure 64 provides a good overview of the network architecture.

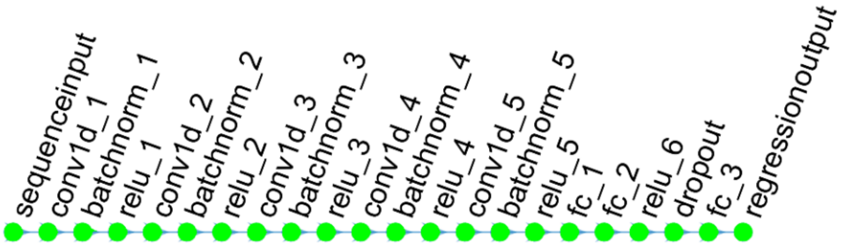

Figure 64: CNN architecture

The calculation of the root mean squared error (RMSE) across all time cycles of the test sequences provides rightful information to analyze how well the network performs on the test data.

The capability of the network predictor to perform throughout the given sequence of data in the test engines can be inferred from the comparison shown in Figure 65. The degradation process is represented by a combination of straight lines. The predicted RUL against the true RUL of a best case prediction reveals a 12-cycle difference concerning the prediction by the CNN and the test data at the fianl stage of this analysis. In general, the agremeent with test data is very good according to Figure 65. However, the CNN prediction of RUL is lower along the some part of period analyzed. In addition, each time this example is run, different results are obtained (Figure 66).

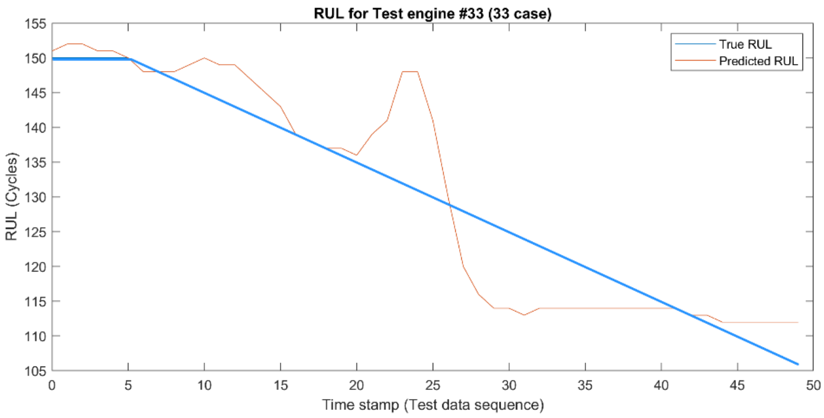

Figure 65: Best prediction case

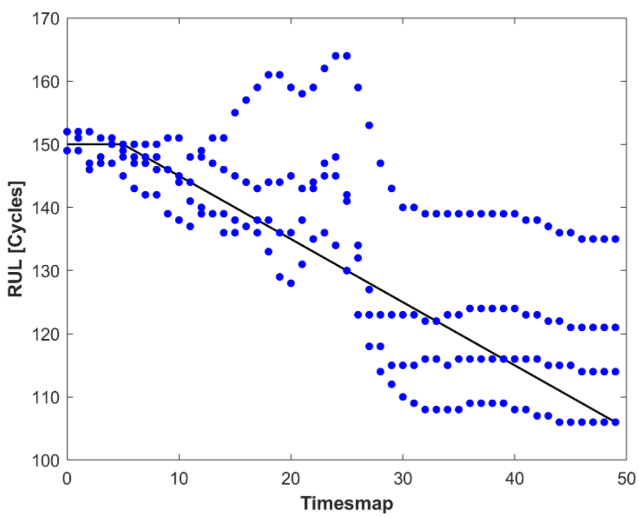

Figure 66: variability of RUL predictions for engine no. 33

5. Conclusions

The Chapter addressed some relevant noise and vibration issues related to transport aircraft and rotorcraft. An example of an application for noise estimation of turbofan engine components showed excellent agreement with two other methods. This approach jointly with another for estimation of airframe noise was employed in an MDO framework for the optimal design of a 78-seat airliner. The flyover noise was posed as a constraint and was effectively reduced for the individuals in the Pareto front when compared to a reference airplane.

From the CFD runs described in the present work, suggestions to lower the noise power level generated by main landing gear arrangements and sensors placed in front fuselages of transport aircraft are provided.

The forecast of the crude oil price by the regularization of non-stationary time series was carried out and the results can be considered acceptable.

A methodology to predict remained useful life of turbofan engines was described and applied to real data made available by NASA. The methodology utilizes convolutional neural networks and there is no need to manually extract features from data.

Acknowledgments

Part of the computations used in the present work was carried out with hardware and software purchased with the support of the Brazilian federal agency Financiadora de Estudos e Projetos (FINEP) through the project CAPTAER II.

The authors would like also to acknowledge the support from the Program HUMS OFFSET-Brazil, HX-BR, carried out in the EUROCOPTER facilities in Marignane, France, involving the Brazilian Universities Instituto Tecnológico de Aeronáutica and UNIFEI, EUROCOPTER-France, and HELIBRAS.

References

1. **Inquiété, Guillaume.** *Offset Brazil: Dynamics and Vibrations - Equipment Qualification.* Marignane : Eurocopter, 2012.
2. **Jorge, A. B.** *Fault detection system of a helicopter rotor from the vibration level (Systeme de Detection de Defauts d'un Rotor d'Helicoptere a Partir du Niveau Vibratoire.* Toulouse : ENSICA, 1992.
3. **Cruz, Ronaldo Vieira.** *Fundamentos da Engenharia de Helicópteros e Aeronaves de Asas Rotativas.* São José dos Campos : ITA, 2022. Apostilha de PRJ-91.
4. **Certain, Bernard, et al.** *Offset Brazil: Vibrations and Ressonance.* [Powerpoint Presentation] Marignane : Eurocopter Test Flight Department, 2012.
5. **Eurocopter.** *THM AS 350B3 Squirrel: Mechanics Instruction Manual.* [PDF] Marignane : Eurocopter, 2010.
6. **Lacaille, J., et al.** Turbofan Engine Monitoring with Health State Identification and Remaining Useful Life Anticipation. *International Journal of Condition Monitoring.* 2, 2015, Vol. 5.
7. **Morel, H.** *Brazil Offset: Dynamics/Health & Monitoring System.* [Powepoint Presentation] Marignane : Eurocopter, 2012.
8. **Rotor & Wing Aviation Services.** Rotor Blade Balancing – Rotor Track & Balance (RTB) & Helicopter Vibration. *Helicopter Rotor Blade Balancing – Tools, Techniques & Education.* [Online] Rotor & Wing Aviation Services, 2022. https://www.rwas.com.au/rotor-track-and-balance-rtb/.
9. **Basner, Mathias, et al.** Aviation Noise Impacts: State of the Science. *Noise&Health.* 2017, Vol. 41.
10. **Mauel, Stefan.** Frankfurt Airport Pioneers Active Noise Abatement. *International Airport Review.* [Online] Russel Publishing Limited, 2015. https://www.internationalairportreview.com/article/20017/frankfurt-airport-pioneers-active-noise-abatement/.
11. **Roulois, G.** *Offset Brazil: Internal Noise.* Marignane : Eurocopter, 2012.

12. **Magalhães, P. E. and Mattos, Bento Silva.** Environmental Aspects of Airplane Design. *Conceptual Design of Green Transport Airplane.* Sharjah : Bentham Science Publishers, 2018, p. 436.
13. **Wikipedia, The Free Encyclopedia.** Sound Power. *Wikipedia.* [Online] Wikipedia, The Free Encyclopedia, 2022. https://en.wikipedia.org/wiki/Sound_power.
14. **Lighthill, Michael James.** On Sound Generated Aerodynamically I. General Theory. *Proceedings of the Royal Society of London Series A.* 1952, Vol. 211.
15. **Rienstra, S. and Hirschberg, A.** An Introduction to Acoustics. [Online] 2021. https://www.win.tue.nl/~sjoerdr/papers/boek.pdf.
16. **Fluent, Inc.** *Fluent 6.2 User Manual.* New Hampshire : Fluent, Inc., 2005.
17. **Pan, Y. S.** Perturbation Solution of the Navier-Stokes Equations and its Relation to the Lighthill-Curie . *Journal of the Acoustical Society of America.* 1975, Vol. 58.
18. *In Computational Aeroacoustic Analysis of Slat Trailing-Edge Flow.* **Lockard, D., Brentner, K. and Singer, B.** Bellevue : %th AIAA/CEAS Aeroacoustics Conference, 1999. AIAA-99-1802.
19. *Aeronoise of a Slatted-Airfoil Configuration.* **Ton, T. A., et al.** Reno : 46th AIAA Aerospace Sciences Meeting and Exhibit, 2008. AIAA 2008-0014.
20. **van der Kooi, J. T.** *An Experimental Study of Aolean Tones and Trailing-edge Noise.* Twente : Master Thesis, University of Twente, 2006.
21. **West, G. S.** Measurements of Fluctuation Pressures and Forces on a Cylinder in the Reynolds Number Range 104 to 2.5 x 105. *Jounal of Fluids and Structures.* 1993, Vol. 7.
22. **Norberg, C.** Fluctuating Lift on Circular Cylinder: Review and New Measurements. *Journal of Fluids and Structures.* 2003, Vol. 17.
23. *Large-Eddy Simulation: Present state and future perspectives.* **Piomelli, U.** Reno : 36th AIAA Aerospace Sciences Meeting and Exhibit, 1998. AIAA 098-0534.
24. **Templeton, Jeremy, Wang, Meng and Moin, Parviz.** Towards LES Wall Models Using Optimization Techniques. *Researchgate.* [Online] 2002. https://www.researchgate.net/publication/251501476_Towards_LES_wall_models_using_optimization_techniques.
25. **Antoine, Nicolas.** *Aircraft Noise Overview.* Stanford, CA : Aircraft Design & Aerodynamic Group, Stanford University, 2000.
26. **William, Ffowcs and Hawkings, J.** Sound Generation by Turbulence and Surface in Arbitrary Motion. *Phil. Trans. Roy Soc. London.* 1969, Vol. 264.
27. *In Aeroacoustic Study of Airfoil Leading Edge High-Lift Devices.* **Andreou, C., Graham, W. and Shin, H.** Cambridge, MA : 27h AIAA/CEAS Aeroacoustics Conference, 2006. AIAA 2006-2515.
28. **Proudman, I.** The Generation of Noise by Isotropic Turbulence. *Proc. Royal Society.* 114, 1952.
29. **Lilley, G. M.** *The radiated noise from isotropic turbulence revisited.* Hampton, VA : NASA, 1993. CR-93-75.
30. **Ansys, Inc.** Ansys Fluent R15 Tutorial Guide. *Absys Fluent.* [Online] 2013. https://vdocument.in/ansys-fluent-tutorial-guide-r-15.html.
31. **Larosterna.** Sumo: Open Source Mesher. *larosterna Products.* [Online] larosterna, 2017. https://www.larosterna.com/products/open-source.
32. **Cao, Xin, Yuhong, Jia and Jiajie, Tian.** Research on Landing Impact Characteristic of Multi-wheel Bogie Landing Gear's Truck. *International Journal of Aerospace System Engineering.* 2015, Vol. 2.
33. **Glegg, Stewart and Davenport, William.** Open Rotor Noise - Tone and Broadband noise. *Tone Noise.* [Online] ScienceDirect, 2022. https://www.sciencedirect.com/topics/engineering/tone-noise.
34. **Deaconu, Marius, et al.** Helicopter Inside Cabin Acoustic Evaluation: A Case Study - IAR Puma 330. *International Journal of Environment Research and Public Health.* September 2021, pp. 1-14.
35. *Two-dimensinal Fourier Transform Analysis of Helicopter Flyover Noise*. **Farassat, Odylin and Morris, J. Philip.** 55th Annual Forum of the American Helicopter Society : American Helicopter Society, 1999.
36. **Oswald, Fred B., et al.** *Influence of Gear Design on Gearbox Radiated Noise.* Washington, D.C. : NASA Lewis Research Center, 1994. TM-106511.
37. **Yu, Liya, et al.** Gear Fault Diagnosis through Vibration and Acoustic Signal Combination Based on Convolutional Neural Network. *Information.* 2020, Vol. 11.
38. **Huff, Dennnis.** *Noise Reduction Technologies for Turbofan Engines.* Cleveland : NASA/TM—2007-214495, 2007.
39. *Noise Estimation of Installed Turbofan Engines.* **Muraro, Daniel A.** São José dos Campos : 2009 Brazilian Symposium on Aerospace Eng. & Applications, 2009. 3rd CTA-DLR Workshop on Data Analysis & Flight Control.

40. **Heideman, M. F.** *Interim Prediction Method for Fan and Compressor Source Noise.* Cleveland : NASA Lewis Research Center, 1979. p. 68p. TM-X-71763.
41. **Huff, R. G., Clark, B. J. and Dorsch, R. G.** *Interim Prediction Method for Low Frequency Core Engine Noise.* NASA. s.l. : NASA Lewis Research center, 1974. p. 25p. TM-X-71627.
42. **Stone, J. R.** *Interim Prediction Method for Jet Noise.* NASA. s.l. : NASA Lewis Research Center, 1974. TM-X-71618.
43. **Schmid, Michael.** *Entwicklung eines Programmmoduls zur Prognose des Lärms von Strahltriebwerken im Flugzeugvorentwurf.* Berlin : Technische Universität Berlin, Studienarbeit, 2001.
44. **ESDU.** *Computer-based estimation procedure for single-stream jet noise.* s.l. : ESDU 98019, 1998.
45. *The Best Suited Airliner for an Existing Airline Network.* **Siqueira, L., Mattos, B. S. and Loureiro, V.** Palm Springs : 50th AIAA/ASME/ASCE/AHS/ASC Structures, Structural Dynamics, and Materials Conference, 2009. AIAA Paper 2009-2206.
46. *Conceptual optimal design of environmentally friendly airliners: a review of available methodologies and their integration into a consistent framework for everyday use.* **Magalhães, P. E. and Mattos, Bento Silva.** Dallas : 16th AIAA/ISSMO Multidisciplinary Analysis and Optimization Conference, 2015. AIAA 2015-3358.
47. **Secco, Ney and Mattos, Bento Silva.** Artificial neural networks to predict aerodynamic coefficients of transport airplanes. *Aircraft Engineering and Aerospace Technology.* March 2017, pp. 211-230.
48. **Mattos, Bento Silva and Secco, Ney Rafael.** An Airplane Calculator Featuring a High-Fidelity Methodology for Tailplane Sizing. *Journal of Aerospace Technology and Management.* 2013, Vol. 5, pp. 371-386.
49. **EMBRAER Commercial Aviation.** Embraer 175 Performance. [Online] 2018. https://www.embraercommercialaviation.com/wp-content/uploads/2017/02/Embraer_spec_175_web.pdf.
50. **EASA.** *Type-Certificate Data Sheet for Noise for ERJ 170.* s.l. : EASA, 2016. p. 14 of 27. EASA.IM.A.001.
51. **GE Aviation.** CF34-10E - GE Aviation. [Online] October 2018. https://www.geaviation.com/bga/engines/cf34-engine.
52. **Rosebrock, Adrian.** Convolutional Neural Networks (CNNs) and Layer Types. *pyimagesearch.* [Online] Pyimagesearch, 2021. https://pyimagesearch.com/2021/05/14/convolutional-neural-networks-cnns-and-layer-types/.
53. **Krizhevsky, Alex, Sutskever, Ilya and Hinton, Geoffrey.** ImageNet Classification with Deep Convolutional Neural Networks. *Communications of the ACM.* 2017, Vol. 60, 6, pp. 84-90.
54. **IBM.** Convolutional Neural Networks. *IBM Cloud Education.* [Online] IBM, October 2020. https://www.ibm.com/cloud/learn/convolutional-neural-networks.
55. **Asthana, Meghna.** Layers of a Convolutional Neural Network. *Analytics Vidhya.* [Online] Analytics Vidhya, March 2020. https://medium.com/analytics-vidhya/layers-of-a-convolutional-neural-network-168daddd2dd1.
56. **Mathworks, Inc.** Convolutional Network. *Mathworks.* [Online] Mathworks, Inc., 2022. https://www.mathworks.com/discovery/convolutional-neural-network-matlab.html.
57. **Sanchez, H.** Time Series Forecasting Using Hybrid Convolutional Neural Network - Recurrent Neural Network. *Matlab File Exchange.* [Online] Mathworks, Inc., 2002. https://www.mathworks.com/matlabcentral/fileexchange/91360-time-series-forecasting-using-hybrid-cnn-rnn?s_tid=srchtitle. 91360.
58. **U.S. Energy Information Administration.** Petroleum & Other Liquids. *U.S. Energy Information Administration.* [Online] May 2022. https://www.eia.gov/petroleum/reports.php#/T1288. Excel Worksheet.
59. **Box, George and Jenkins, Gwilym.** *Time Series Analysis: Forecasting and Control.* San Francisco : Holden-Day, 1970.
60. **Wikipedia, The Free Encyclopedia.** Dickey–Fuller Test. [Online] Wikipedia, The Free Encyclopedia, 2022. https://en.wikipedia.org/wiki/Dickey%E2%80%93Fuller_test.
61. **Mathworks, Inc.** regARIMA class. *Matlab User Guide.* [Online] Mathworks, Inc., 2022. https://www.mathworks.com/help/econ/regarima-class.html.
62. *Damage propagation modeling for aircraft engine run-to-failure simulation.* **Saxena, Abhinav, et al.** s.l. : International Conference on Prognostics and Health Management, PHM , 2008.
63. **Khan, S. and Yairi, T. S.** A Review on The Application of Deep Learning in System Health Management. *Mechanical Systems and Signal Processing.* 2018, Vol. 107.

64. **Mathworks, Inc.** Remaining Useful Life Estimation Using Convolutional Neural Network. *Mathworks.* [Online] Mathworks, 2022. https://www.mathworks.com/help/predmaint/ug/remaining-useful-life-estimation-using-convolutional-neural-network.html.

65. **Li, Xiang, Ding, Qian and Sun, Jian-Qiao.** Remaining Useful Life Estimation in Prognostics Using Deep Convolution Neural Networks. *Reliability Engineering & System Safety.* 2018, Vol. 172.

66. **NASA Ames.** Turbofan engine degradation simulation data set . *Dashlink.* [Online] NASA, 2022. https://ti.arc.nasa.gov/tech/dash/groups/pcoe/prognostic-data-repository/#turbofan.